LUND UNIVERSITY

Short Attosecond Pulse Trains at High Repetition Rates for Novel Pump-Probe and Coincidence Studies

Mikaelsson, Sara

2021

Document Version:
Publisher's PDF, also known as Version of record

Link to publication

Citation for published version (APA):
Mikaelsson, S. (2021). *Short Attosecond Pulse Trains at High Repetition Rates for Novel Pump-Probe and Coincidence Studies*. Department of Physics, Lund University.

Total number of authors:
1

Short Attosecond Pulse Trains at High Repetition Rates for Novel Pump-Probe and Coincidence Studies

SARA MIKAELSSON

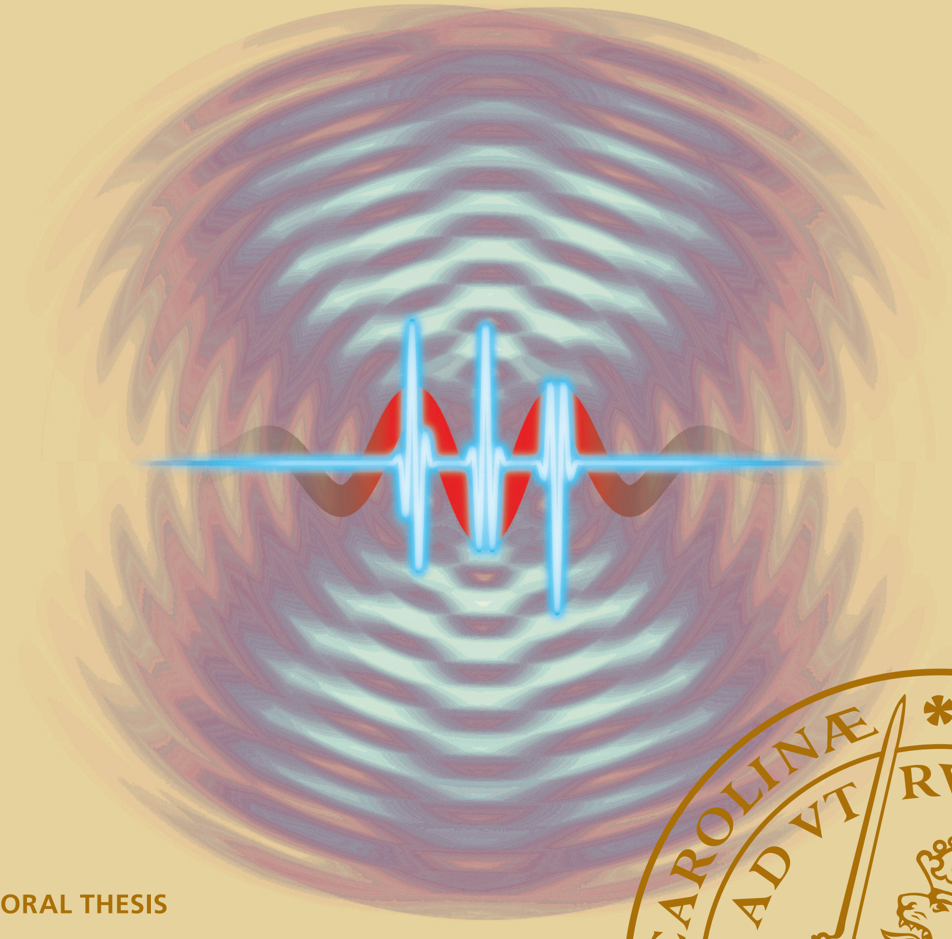

DOCTORAL THESIS

Faculty of Engineering, LTH
Department of Physics
Division of Atomic Physics
Lund University

Short Attosecond Pulse Trains at High Repetition Rates for Novel Pump-Probe and Coincidence Studies

Short Attosecond Pulse Trains at High Repetition Rates for Novel Pump-Probe and Coincidence Studies

by Sara Mikaelsson

LUND
UNIVERSITY

Thesis for the degree of PhD in Physics
Thesis advisors: Dr. Cord L. Arnold, Prof. Anne L'Huillier, Dr. Miguel Miranda
Faculty opponent: László Veisz

To be presented, with the permission of the Faculty of Engineering, LTH of Lund University, for public criticism in Rydberg lecture hall at the Department of Physics on Friday, the 29th of January 2021 at 09:00.

Organization **LUND UNIVERSITY** Atomic Physics Box 118 SE–221 00 LUND Sweden	Document name **DOCTORAL DISSERTATION**
	Date of disputation 2021-01-29
	Sponsoring organization
Author(s) Sara Mikaelsson	

Title and subtitle

Short Attosecond Pulse Trains at High Repetition Rates for Novel Pump-Probe and Coincidence Studies

Abstract

This work aims at studying photoionization dynamics from atoms and surfaces at atomic time scales. The work was based on development and applications of a high repetition rate High-order Harmonic Generation (HHG) light source that utilizes Optical Parametric Amplification (OPA) laser technology. The laser system delivers few-cycle pulses in the near infrared (IR) at a repetition rate of 200 kHz. Through the use of advanced pulse characterization techniques, the pulse quality was kept high in order to ensure efficient HHG at relatively low pulse energies.

In the HHG process, a short extreme ultraviolet (XUV) light pulse of attosecond duration is produced with every half cycle of the driving field. When performing HHG with driving pulses in the few-cycle regime, a short attosecond pulse train consisting of only a handful pulses is generated. The spectral properties and temporal structure of the HHG radiation was explained in terms of interference between attosecond pulses. The number of pulses can be controlled with the Carrier-to-Envelope Phase (CEP).

The short pulse trains were used together with a weak IR field for two-color photoionization, measured with a 3D momentum imaging spectrometer. The angle-resolved photoionization spectra are found to be asymmetric, and behave distinctly different depending primarily on the number of pulses that are used for ionization. In the case when two pulses are used, the electron peaks are shifted, but when the number is increased to three, additional peaks appear. This was explained using an attosecond time-slit interference model.

The coincidence capabilities of the photoelectron spectrometer were utilized to measure single-photon double-ionization of helium for the first time with an HHG source. This challenging measurement combines the coincidence and imaging properties of the spectrometer with the efficient generation of high harmonics, and is only possible due to the high repetition rate of the source. The full Triple Differential Cross Section (TDCS) was obtained for a range of energies.

Additionally, the IR light source was used for surface science applications, which benefit strongly from a high repetition rate. Light-wave driven currents in semiconductor materials were measured at a higher repetition rate and with longer pulses than reported previously. Plasmon dynamics in gold nanosponges and induced at the edges of thin layers of the Transition Metal Dichalcogenide (TMD) WSe2 were studied.

Key words

Attosecond, High-Order Harmonic Generation, Photoionization

Classification system and/or index terms (if any)

Supplementary bibliographical information		Language English
ISSN and key title 0281-2762		ISBN 978-91-7895-713-2 (print) 978-91-7895-714-9 (pdf)
Recipient's notes	Number of pages 258	Price
	Security classification	

I, the undersigned, being the copyright owner of the abstract of the above-mentioned dissertation, hereby grant to all reference sources the permission to publish and disseminate the abstract of the above-mentioned dissertation.

Signature

Date 2020-12-14

DOKUMENTDATABLAD enl SIS 61 41 21

Short Attosecond Pulse Trains at High Repetition Rates for Novel Pump-Probe and Coincidence Studies

by Sara Mikaelsson

LUND
UNIVERSITY

A doctoral thesis at a university in Sweden takes either the form of a single, cohesive research study (monograph) or a summary of research papers (compilation thesis), which the doctoral student has written alone or together with one or several other author(s).

In the latter case the thesis consists of two parts. An introductory text puts the research work into context and summarizes the main points of the papers. Then, the research publications themselves are reproduced, together with a description of the individual contributions of the authors. The research papers may either have been already published or are manuscripts at various stages (in press, submitted, or in draft).

Cover illustration front: Illustration of electron wave packet interference from short pulse trains.

Cover illustration back: 3D plot of photoelectron momentum distribution from single ionization with high-order harmonics.

Funding information: The thesis work was financially supported by the Swedish Research Council, the European Research Council (Grant PALP), and the Knut and Alice Wallenberg Foundation.

Faculty of Engineering, LTH, Atomic Physics

ISBN: 978-91-7895-713-2 (print)
ISBN: 978-91-7895-714-9 (pdf)
ISSN: 0281-2762

Printed in Sweden by Media-Tryck, Lund University, Lund 2021

Abstract

This work aims at studying photoionization dynamics from atoms and surfaces at atomic time scales. The work was based on development and applications of a high repetition rate High-order Harmonic Generation (HHG) light source that utilizes Optical Parametric Amplification (OPA) laser technology. The laser system delivers few-cycle pulses in the near infrared (IR) at a repetition rate of 200 kHz. Through the use of advanced pulse characterization techniques, the pulse quality was kept high in order to ensure efficient HHG at relatively low pulse energies.

In the HHG process, a short extreme ultraviolet (XUV) light pulse of attosecond duration is produced with every half cycle of the driving field. When performing HHG with driving pulses in the few-cycle regime, a short attosecond pulse train consisting of only a handful pulses is generated. The spectral properties and temporal structure of the HHG radiation was explained in terms of interference between attosecond pulses. The number of pulses can be controlled with the Carrier-to-Envelope Phase (CEP).

The short pulse trains were used together with a weak IR field for two-color photoionization, measured with a 3D momentum imaging spectrometer. The angle-resolved photoionization spectra are found to be asymmetric, and behave distinctly different depending primarily on the number of pulses that are used for ionization. In the case when two pulses are used, the electron peaks are shifted, but when the number is increased to three, additional peaks appear. This was explained using an attosecond time-slit interference model.

The coincidence capabilities of the photoelectron spectrometer were utilized to measure single-photon double-ionization of helium for the first time with an HHG source. This challenging measurement combines the coincidence and imaging properties of the spectrometer with the efficient generation of high harmonics, and is only possible due to the high repetition rate of the source. The full Triple Differential Cross Section (TDCS) was obtained for a range of energies.

Additionally, the IR light source was used for surface science applications, which benefit strongly from a high repetition rate. Light-wave driven currents in semiconductor materials were measured at a higher repetition rate and with longer pulses than reported previously. Plasmon dynamics in gold nanosponges and induced at the edges of thin layers of the Transition Metal Dichalcogenide (TMD) WSe2 were studied.

Popular Science Summary

When people who know nothing about physics have asked me what my PhD work is about, I have often said that ”I shoot lasers at stuff to see what happens!” It is meant to be a little funny and disarming—although also true. I have noticed a funny thing, though: it is rare that anyone questions what the *point* of that is supposed to be. Non-scientists and scientists alike are fascinated by the world that surrounds us, and the desire to understand and explore it—from its smallest parts to the stars that are light-years away—is as universal as the drive to make music, tell stories, or come together to share a meal.

In the millennia since we humans begun our collective history and started passing knowledge on through generations, the limits of what is possible to investigate and explore have expanded, through collective effort put into the creation of knowledge and enormous technological advancement. During my thesis work, where I in some small way have attempted to contribute to this scientific project, I have looked at things that are at the lower limit of what is possible to study today—things that are very very small, and especially, very very *fast*.

Super Small and Ultrafast

A general principle that agrees with our everyday human intuition is that small things are fast, and big things are slow. Compare the frantic pacing of a small rodent to the lazy, languid movements of a whale. Mountains rise and erode over millennia while sandbanks disappear in days; galaxies form and collapse over billions of years, but electrons move on a time scale of *attoseconds*. One attosecond is 10^{-18} seconds—that is seventeen decimal zeroes before the one, like so:

$$0.000000000000000001\mathrm{s}$$

Is it even possible to measure things that move that fast?

Actually, since the beginning of this millennium, scientists have been able to produce light pulses that have a duration on the scale of attoseconds. These light pulses have very short wavelengths, short enough that they cannot be seen by the human eye—indeed they are closer to X-rays than to visible light—and interact very strongly with most matter. That breakthrough has provided a foundation for the, appropriately named, field of *attosecond science*. By using such light pulses in a manner similar to the flash of a camera, it is possible to study the dynamics of electrons on their natural timescale.

Attosecond pulses are produced by state-of-the-art high-intensity laser systems, and in fact, the development of laser technology has been closely tied to the field since its beginnings.

Better, stronger, and more stable lasers means better control over the attosecond pulses, and in turn better conditions for experiments and measurements. In this thesis, much of the work has been on developing such a laser system capable of generating attosecond pulses.

Strength vs Speed

While it's certainly nice to dream about a laser system that has as much power as you want and that can fire at whatever speed you like, that's not realistically achievable. Instead, when designing a laser, there is always a trade-off between the energy contained in one laser pulse, and how often you can produce those pulses. The most powerful, large-scale laser systems in the world are only able to fire maybe once or twice a day! Instead of pushing towards something bigger and stronger, however, the goal of the laser I've worked on has been to increase the amount of pulses per seconds, i.e. the *repetition rate* of the laser.

In the field of attosecond science, the techniques used are often so called *pump-probe* experiments. The idea is, to use the short light pulses as the flash of a camera, and then take snapshots at different times during a process. One light pulse starts the process—the pump, and a second one makes a read-out—a probe. Of course, that only gives a single snapshot. In the case of atoms and electrons, though, luckily the exact same state can be prepared again and again, and therefore it is possible to start it over and over again in order to make many readouts, and in the end get a full recording of the whole process. For these kind of applications, it is therefore better to have a higher repetition rate, but with less energy per pulse. Still, many experiments—including the generation of attosecond pulses themselves—require high light intensities. That means the relatively small energy of high repetition rate pulses must be contained tightly; in space, but also in time.

During my thesis work, I have worked on understanding how this confinement of the available energy in time—i.e. the use of very short laser pulses for the generation of the even shorter attosecond pulses—affects the measurement techniques commonly used in attosecond science.

But is There a Point Though?

So if I have now made a convincing case that it is possible to measure things that happens this absurdly quickly, maybe it is tempting to ask the question I preemptively dodged right at the beginning: Is there a point to all of this? The answer is a resounding yes! The initial motions of electrons that take place over attoseconds are crucial in longer processes, like the forming and breaking of chemical bonds—including those in our DNA, and other bio-molecules which all life is built from. To understand, and maybe one day even be able to control those things, certainly seems like an exciting prospect. By studying other, more elemental processes, it is also possible to investigate more fundamental questions. When we explore things that are as small and fast as electrons, we enter the realm of physics that is governed by *quantum mechanics*, where particles behave like waves, can be in several places at once, and may be correlated and entangled in ways that contradict the ways we humans experience the world around us.

The field of attosecond science mostly studies *photoionization*, where the interaction of light with matter results in the emission of electrons. One of the most interesting applications of a system that works at high repetition rates is the possibility of doing *coincidence* experiments. That means measuring the properties of several particles that come from the same event; for example an emitted electron and the remaining ion after photoionization. In principle, the electrons and ions can go ever which way after the ionization event, and if a detector is just placed somewhere close to the laser focus where the interaction takes place, it would only catch a small fraction of the emitted particles. Luckily, charged particles interact with electromagnetic fields, and by designing the right combination of electric and magnetic fields, the charged particles will be pushed apart—ions in one direction and electrons in the other, towards different detectors. The faster electrons also have to be steered by a magnetic field, guiding them in a circular motion to the detector. If both the position and arrival time at the detector are recorded properly, one can completely reconstruct both the speed of the electron and ion and which direction they went in, right as they were ionized. Spectrometers like this are called *reaction microscopes*, since like with a regular microscope we can get a complete picture of something extremely small—in this case a reaction between light and matter.

During my thesis work, I have applied the high repetition rate attosecond pulses in combination with a reaction microscope to measure photoionization, using coincidence methods. I've applied those methods not only to the coincidence between electrons and ions, but also between pairs of electrons that have been emitted together. Such pairs of electrons will be highly correlated, and by following how they evolve in time, it might be possible to really dig into some cool fundamental quantum mechanical properties of matter. Together with the development of a good understanding of how to perform time resolved pump-probe measurements, this thesis has laid a solid foundation for further exploration of quantum dynamics at the attosecond timescale.

Populärvetenskaplig Sammanfattning

För att förklara vad jag har gjort under min doktorandtid för de som inte kan så mycket fysik, brukar jag oftast säga att ”Jag skjuter lasrar på saker för att se vad som händer!” Tanken är att det ska få folk att skratta lite, men här är en annan rolig sak som jag upptäckt—det är väldigt sällan någon ifrågasätter vad det ska vara bra för. Forskare som lekmän; alla är vi fascinerade av den värld vi lever i, och viljan att utforska och försöka förstå vår omgivning—från dess minsta beståndsdelar till stjärnorna som vi ser ljusår bort—är lika allmängiltig som önskan att spela musik, berätta historier, eller dela en god måltid.

Under de tusentals år som passerat sedan vår gemensamma mänskliga historia startade och vi började föra med oss vår kunskap genom generationer, har gränserna för vad som är möjligt att utforska fortsatt flyttas genom gemensamma ansträngningar som producerat kunskap och enorma teknologiska framsteg. Under min tid som doktorand, där jag har försökt bidra till ett litet hörn av detta vetenskapliga projekt, har jag fokuserat på det som går att finna vid den lägre gränsen för vad som är möjligt att studera idag—saker som är väldigt väldigt små, och framförallt, väldigt väldigt *snabba*.

Super smått och ultrasnabbt

En generell princip som överensstämmer väl med vår vardagliga mänskliga intuition är att små saker är snabba, och stora saker är långsamma. Jämför de hektiska springandet hos en liten mus med de makliga rörelserna hos en val. Berg uppstår och eroderar över millenium medan sandbankar kan försvinna på en dag; galaxer bildas och kollapsar över billioner år, och elektroner rör sig på en tidskala av *attosekunder*. En attosekund är 10^{-18} sekunder—det är sjutton nollor efter decimaltecknet men innan ettan, likt så här:

$$0.000000000000000001s$$

Är det ens möjligt att mäta något som går så fort?

Sedan runt millenniumskiftet så har forskare faktiskt kunnat producera ljuspulser som har en varaktighet på attosekundstidsskalan. Dessa ljuspulser har en väldigt kort våglängd, kort nog att de inte kan ses med blotta ögat—de ligger faktiskt närmare röntgenstrålning än synligt ljus—och de interagerar väldigt starkt med materia. Det genombrottet har lagt grunden för det ändamålsenligt nämnda fältet *attosekundsfysik*. Genom att använda dessa ljuspulser likt en kamerablixt så är det möjligt att studera elektroner på dess naturliga tidsskala.

Attosekundspulser produceras av toppmoderna hög-intensiva lasersystem, och utvecklingen av laserteknik har därför varit tätt sammanlänkad med fältets utveckling sedan dess början. Bättre, starkare, och mer stabila lasrar medför bättre kontroll över attosekundspulserna och bättre förutsättningar för experiment och mätningar. En stor del av den här avhandlingen har varit riktad mot att utveckla ett sådant lasersystem som kan generera attosekundspulser.

Styrka eller hastighet

Det är trevligt att drömma om en laser som har obegränsat med kraft och samtidigt kan avfyras så ofta du vill. I verkligheten är det inte möjligt, och när en laser ska byggas så måste en alltid göra en avvägning mellan energi per laserpuls, och hur ofta pulserna kan produceras. De kraftfullaste lasersystemen som finns idag kan bara avfyras en eller två gånger om dagen! Men istället för att försöka bygga något större och starkare, så har målet med lasern jag jobbat med varit att öka *repetitionshastigheten* hos pulserna.

Inom attosekundsfältet används dock oftast mättekniker såsom *pump-prob* experiment. Idéen bakom sådana experiment är, så som jag nämnde tidigare, att använda de korta ljuspulserna som en kamerablixt, och sedan ta bilder vid olika tillfällen under samma process. En ljuspuls startar processen—pumpen, och en läser av vad som hänt—proben. Det i sig ger dock naturligtvis bara en ögonblicksbild. För atomer och elektroner är det lyckligtvis möjligt att försätta ett system i exakt samma tillstånd om och om igen, och samma process kan alltså startas upprepade gånger för många avläsningar, som kan kombineras till en fullständig mätning. För sådana applikationer är det därför bättre att ha mindre energi per puls, om dessa pulser kan produceras oftare. För att fortfarande kunna nå de höga intensiteten som krävs för många experiment—vilket inkluderar generationen av själva attosekundspulserna—så måste den relativt låga energin koncentreras både på en liten yta, men också under en kort tid.

Under mitt doktorandarbete så har jag jobbat på att öka förståelsen för hur denna begränsning av pulserna till en kort tid—dvs. användandet av väldigt korta laserpulser för att generera de ännu kortare attosekundspulserna—påverkar de mättekniker som vanligtvis används inom attosekundsfysik-fältet.

Men är det faktiskt bra för något?

Om jag nu varit övertygande nog om att det är möjligt att mäta saker som sker så absurt fort, så kanske det är lockade att ställa frågan som jag värjde mig för i början av denna text: Finns det någon poäng med allt detta? Svaret är naturligtvis: Ja! De initiala rörelserna hos elektroner är avgörande i även längre processer så som upplösandet och bildandet av kemiska band—vilket inkluderar de i vårt DNA, och andra biomolekyler som allt liv är baserat på. Att förstå, och kanske en dag kunna kontrollera, sådana processer är definitivt ett intressant projekt. Genom att studera andra mer grundläggande processer kan vi också besvara mer grundläggande frågor. När vi utforskar något så litet och snabbt som en elektron, så har vi nått den del av fysikens värld där *kvantmekaniken* råder, där partiklar beter sig som vågor, kan vara på flera platser samtidigt, och vara korrelerade och sammanflätade på sätt som är motsägelsefullt i jämförelse med sättet vi människor upplever världen.

Attosekundsfysikfältet studerar framförallt *fotojonisation*, där interaktionen mellan ljus och materia resulterar i en utsöndring av elektroner. En av de mest intressanta applikationerna av ett system som har en hög repetitionshastighet är möjligheten att göra koincidensmätningar. Det innebär att mäta flera partiklar som kommer från samma händelse; till exempel en elektron och den kvarvarande jonen efter fotojonisering. Sådana partiklar kan generellt fara varsomhelst efter de frisläppts, och om en detektor bara placeras nära laserfokuset där interaktionen sker, kommer bara en bråkdel av all möjliga partiklar att kunna fångas. Lyckligtvis så influeras laddade partiklar av elektromagnetiska fält, och genom att designa rätt kombination av elektriska och magnetiska fält så kommer partiklarna först att separeras i olika riktningar—joner åt ett håll och elektroner åt ett annat. De snabbare elektronerna måste också styras av ett magnetiskt fält som för dem i en cirkelrörelse mot detektorn. Ifall både positionen och ankomsttiden vid detektorn kan avläsas på rätt sätt så är det möjligt att helt återskapa både den ursprungliga farten hos elektronen och jonen samt vilka håll de far åt efter joniseringen. Denna typ av spektrometer kallas *reaktionsmikroskop*, eftersom liksom med ett vanligt mikroskop så kan en få en komplett bild av något extremt litet—i detta fall en reaktion mellan ljus och materia.

Under mitt doktorandarbete har jag applicerat attosekundspulser med hög repetitionshastighet i kombination med ett reaktionsmikroskop för att mäta fotojonisation, med hjälp av koincidensmetoder. Jag har applicerat det inte bara på koincidens mellan elektroner och joner, utan också mellan flera elektroner som joniserats samtidigt. Sådana elektronpar kommer vara till hög del korrelerade, och genom att följa deras utveckling i tiden kan en utforska spännande kvantegenskaper hos materia. Tillsammans med en god förståelse för hur tidsupplösta pump-prob experiment kan utföras med samma system, har den här avhandlingen lagt en god grund för fortsatt utforskande och dynamiska kvantmekaniska processer på attosekundsnivå.

List of Publications

This thesis is based on the following publications, referred to by their Roman numerals:

I **Compact 200kHz HHG source driven by a few-cycle OPCPA**

A. Harth, C. Guo , Y.-C. Cheng, A. Losquin, M. Miranda, **S. Mikaelsson**, C. M. Heyl, O. Prochnow, J. Ahrens, U. Morgner, A. L'Huillier and C. L. Arnold
J. Opt., **20**, 014007 (2018)

II **Characterizing ultrashort laser pulses with second harmonic dispersion scans**

I. Sytcevic, C. Guo, **S. Mikaelsson**, J. Vogelsang, A.-L. Viotti, B. Alonso, R. Romero, P. T. Guerreiro, I. J. Sola, A. L'Huillier, H. Crespo, M. Miranda, and C. L. Arnold
Submitted for Publication

III **Phase control of attosecond pulses in a train**

C. Guo, A. Harth, S. Carlström, Y.-C. Cheng, **S. Mikaelsson**, E. Mårsell, C. Heyl, M. Miranda, M. Gisselbrecht, M. B. Gaarde, K. J. Schafer, A. Mikkelsen, J. Mauritsson, C. L. Arnold and A. L'Huillier
J. Phys. B: At. Mol. Opt. Phys., **51**, 034006 (2018)

IV **A high-repetition rate attosecond light source for time-resolved coincidence spectroscopy**
S. Mikaelsson, J. Vogelsang, C. Guo, I. Sytcevic, A.-L. Viotti, F. Langer, Y.-C. Cheng, S. Nandi, W. Jin, A. Olofsson, R. Weissenbilder, J. Mauritsson, A. L'Huillier, M. Gisselbrecht, and C. L. Arnold
Nanophotonics, **10**, 117-128 (2021)

V **Accuracy and precision of the RABBIT technique**

M. Isinger , D. Busto, **S. Mikaelsson**, S. Zhong, C. Guo, P. Salières, C. L. Arnold, A. L'Huillier and M. Gisselbrecht
Phil. Tran. R. Soc. A, **377**, 20170474 (2019)

VI **Controlling photoionization using attosecond time-slit interferences**

Y.-C. Cheng, **S. Mikaelsson**, S. Nandi, L. Rämisch, C. Guo, S. Carlström, A. Harth, J. Vogelsang, M. Miranda, C. L. Arnold, A. L'Huillier and M. Gisselbrecht
Proc. Natl. Acad. Sci., **117**, 10727-10732 (2020)

VII **Few-cycle lightwave-driven currents in a semiconductor at high repetition rate**
F. Langer, Y.-P. Liu, Z. Ren, V. Flodgren, C. Guo, J. Vogelsang, **S. Mikaelsson**, I. Sytcevich, J. Ahrens, A. L'Huillier, C. L. Arnold and A. Mikkelsen
Optica, **7**, 4 (2020)

VIII **Nonlinear plasmon-exciton coupling enhances sum-frequency generation from a hybrid metal/semiconductor nanostructure**
J.-H. Zhong, J. Vogelsang, J.-M. Yi, D. Wang, L. Wittenbecher, **S. Mikaelsson**, A. Korte, A. Chimeh, C. L. Arnold, P. Schaaf, E. Runge, A. L'Huillier, A. Mikkelsen and C. Lienau
Nat. Com., **11**, 1464 (2020)

IX **Coherent excitation and control of plasmons on gold using two-dimensional transition metal dichalcogenides**
J. Vogelsang, L. Wittenbecher, D. Pan, J. Sun, **S. Mikaelsson**, C. L. Arnold, A. L'Huillier, H. Xu, and A. Mikkelsen
Submitted for Publication

All papers are reproduced with permission of their respective publishers.

Abbreviations

3D	Three Dimensional
AOM	Acusto Optical Modulator
APT	Attosecond Pulse Train
BBO	β-Barium Borate
CEO	Carrier-to-Envelope Offset
CEP	Carrier-to-Envelope Phase
CIEL	Coïncidences entre Ion et Electrons Localisés
COLTRIMS	Cold Target Recoil Ion Momentum Spectrometer
CPA	Chirped Pulse Amplification
DFG	Difference Frequency Generation
d-scan	Dispersion scan
EWP	Electron Wave Packet
FEL	Free Electron Laser
FOD	Forth Order Dispersion
FROG-CRAB	Frequency Resolved Optical Gating for Complete Reconstruction of Attosecond Bursts
GD	Group Delay
GDD	Group Delay Dispersion
HeNe	Helium-Neon
HEX	Hexanode
HHG	High-order Harmonic Generation
IR	Infrared
MBES	Magnetic-Bottle Electron Spectrometer
MCP	Micro Channel Plate
NOPA	Non-collinear Optical Parametric Amplification
OPA	Optical Parametric Amplification
OPCPA	Optical Parametric Chirped Pulse Amplification
PEEM	Photoemission Electron Microscope
PSD	Position Sensitive Detector
RABBIT	Reconstruction of Attosecond Beating By two-photon Transitions
REMI	Reaction Microscope
RF	Radio Frequency
RMS	Root Mean Square
SAP	Single Attosecond Pulse
SEM	Scanning Electron Microscope
SFA	Strong Field Approximation

SFG	Sum Frequency Generation
SHG	Second Harmonic Generation
SLM	Spatial Light Modulator
SNR	Signal-To-Noise
TDCS	Triple Differential Cross Section
Ti:Sa	Titanium:Sapphire
TMD	Transition Metal Dichalcogenides
TOD	Third Order Dispersion
TOF	Time Of Flight
VMI	Velocity Map Imaging
XUV	Extreme Ultraviolet

Contents

Chapter 1

Introduction

1 Ultrafast High-Intensity Lasers

Pushing the frontiers of science has always been a complex interplay between technological advancements, development of theory, and discovery of new physical phenomena. One such case is the invention of the laser in 1960 [1], which revolutionized the field of light-matter interaction. The properties of laser light—especially its spatial and temporal coherence—allowed scientists to control light in entirely new ways and apply this hitherto unexplored phenomena. Lasers can be optimized for a multitude of different characteristics—central frequency, frequency bandwidth, average power, peak power, etc. Almost immediately, in 1961, the ability to focus light to unprecedented intensities lead to the observation of the first non-linear interaction between light and matter—the generation of the second harmonic in a crystal [2].

If energy is contained not just in space, as in a beam, but also in time, in a short pulse, the resulting intensity will be significantly higher still. High intensity lasers are therefore inexorably tied to short pulse durations. In order to create a short light pulse, a broad frequency spectrum is required, and one of the most important discoveries in the development of shorter pulses and higher intensities was therefore the discovery of Titanium:Sapphire (Ti:Sa) and its broad gain bandwidth in the mid eighties [3]. When used as a lasing medium, Ti:Sa-based oscillators can generate pulses as short as a few femtoseconds. This is usually done through the process of Kerr lens mode-locking [4], in which a laser resonator is designed so that high intensities are favored through the help of the Kerr effect. This effect also leads to so called self phase modulation which may broaden the spectrum further, resulting in even shorter—ultrashort—pulses.

After their generation, ultrashort pulses may be amplified. The Chirped Pulse Amplification

(CPA) technique [5], awarded the Nobel price in 2018, was an additional breakthrough in this area. Eventually, these developments allowed for the focusing of light to remarkable intensities and the emergence of the field of strong-field physics, where the intensity of the light is high enough that its impact on electrons rivals the bonding potential of the atomic core.

Apart from providing high intensities, the availability of ultrashort pulses also enables time resolved measurements. When studying the temporal dynamics of any object, the relevant timescale is often related to its spatial size. A regular camera recording at 24 frames per second is more than fine for documenting human behavior—however, to study the smallest constituents of matter, such as atoms or molecules, much higher temporal sampling is required. The study of phenomena such as the movement of nuclei in a molecule in respect to each other, and the forming and breaking of chemical bonds, are processes that take place during picoseconds (10^{-12}s) or femtoseconds (10^{-15}s).

To measure those ultrafast dynamics, pump-probe techniques are used. In such a scheme, a pump pulse starts the process of interest, and a second probe pulse, arriving after a certain delay, allows for a read-out of the state of the system—much like taking a snapshot with a camera. By varying the delay between the two pulses, the time evolution of the process can be mapped out. This has been applied with great success in the visible and near IR regime to understand the motion of molecular nuclei in the field of femtochemistry, for which Ahmed Zewail was awarded the Nobel Prize in 1999 [6].

2 Attosecond Science

While a few femtoseconds is a formidably short time duration, there are processes which take place on timescales orders of magnitude faster. The electrons that orbit the atomic nuclei, for example, evolve on durations that need to be measured in attoseconds—10^{-18}s, and the field of attosecond science, in turn, is mostly concerned with studying the dynamic behavior of electrons and electronic states. In order to probe those timescales, however, pulses with a similar pulse duration are necessary, and this requires the shift of the central frequency of the light to higher energies. Apart from enabling shorter pulse durations, light in the extreme ultraviolet (XUV) and X-ray spectral region also interacts strongly with matter and can probe deeper into the atomic shell structure than visible or IR light. When used for imaging purposes, the shorter wavelengths also lowers the diffraction limit and therefore provides higher resolution. Short wavelength light sources are therefore highly desirable.

While laser-active materials in the visible and near IR spectral regions are plentiful, this is not true for higher frequencies. To gain access to these attractive spectral regions, enormous facilities like synchrotrons have been constructed. These large scale facilities are, however, extremely costly and can be hard to access. Similarly, Free Electron Lasers (FELs), which can generate light with high frequencies and large flux, are exciting sources for many fields of science—but only a handful of them have been built due to the cost and complexity involved.

Another option for coherent XUV light sources is the process of High Harmonic Generation (HHG), a non-linear frequency up-conversion process that generates odd order harmonics of the fundamental driving frequency [7, 8]—these harmonics can potentially reach energies in the keV range, i.e. the X-ray regime [9]. The conversion efficiency of the process is low (on the order of 10^{-5} at best). It is, however, possible through HHG to produce XUV radiation for spectroscopy in a regular sized research lab.

In addition to an interesting spectral range, HHG results in pulses with unprecedentedly short time duration—attosecond pulses [10]. Since this discovery, the field of attosecond science has been able to utilize these XUV pulses for a plethora of exciting experiments: time-resolved inner-shell spectroscopy [11], charge migration in molecules [12, 13], ionization delays in atoms [14, 15] and solids [16], and many others.

In order to generate to high-order harmonics, the field intensity of the driving laser must reach approximately 10^{14} W/cm^2. While this is certainly easier when using a laser which provides high energy pulses, it is also possible to focus less energetic laser pulses very tightly for the same result, and the process is scale-invariant [17]. The continued development of better lasers has also lead to better control of HHG, and a large number of attosecond light sources exist today, operating over a large range of pulse energies and wavelengths.

3 Limitations and Current Development

One of the greatest challenges for attosecond science is the low conversion efficiency of the HHG process, which severely limits the XUV flux that can be generated. Optics in the XUV region are also a challenge, since the radiation is so strongly absorbed by any matter—including optical components. Also, the refractive index in this regime is $n \approx 1$, making it impossible to make conventional optics. This means that XUV light is much harder to control and shape than light in the visible region.

One consequences of the limited flux is that the pump-probe scheme, which, for the best time resolution, ideally would use two delayed attosecond pulses [18], is instead usually performed with one XUV attosecond pump pulse, and one replica of the driving near-IR pulse as a probe. The low flux also makes investigations of various non-linear interactions in the XUV regime very difficult. Much effort is still being invested towards the goal of achieving an attosecond source that is capable of pump-probe experiments with two XUV pulses, by trying to improve the output pulse energy, and attosecond sources can today provide peak output powers in the GW range [19]. However, these high pulse energy sources have to compromise elsewhere. The increase in energy per pulse comes at the expense of repetition rate, which usually ends up around tens of Hz, or at best 1 kHz.

In contrast, some experiments require very little XUV energy. When doing electron imaging [20], space charge from the emission of too many electrons will ruin resolution, and therefore the amount of electrons emitted at once must be limited. This requires a low energy per pulse, but still many pulses for a high signal-to-noise (SNR) ratio. A similar problem occurs for coincidence measurements [21], where one must be able to know that several measured particles originate from the same event. A higher XUV pulse energy means more ionization events per shot, which is incompatible with this type of measurements. In order to record many events for good SNR, again, the repetition rate must be increased.

The development of attosecond XUV sources is often towards one of these two directions—higher pulse energies and higher intensities, or higher repetition rates. The main limitation, in both cases, is the available laser technology. Recent developments of fiber lasers and optical parametric amplification techniques have led to large improvements in the latter case, and at the same time, the understanding of how to do HHG with these sources was established. In the last decade, HHG sources with repetition rates of several hundreds of kHz have been constructed [22–26].

4 Scope of this Work

This thesis work has been concerned with pushing attosecond science towards higher repetition rates, and has been centered around the 200 kHz laser source at the Lund Laser Centre. This laser system is based on an octave spanning Ti:Sa oscillator, which provides pulses with a duration of <6 fs and is able to operate at a high repetition rate via the use of non-linear parametric processes for further amplification. This thesis has focused on establishing a beamline for attosecond science and in particular the study of photoionization, and has included work on the whole chain, from the laser to the photoelectron spectrometer.

At the beginning of the thesis, a lot of effort was devoted to the laser itself, its characterization and its stable and efficient operation. Due to the difficulties involved in measuring ultrashort pulses, this involved work on characterization methods, which are crucial for obtaining high quality pulses and consistent operation. The laser output was also used directly to investigate ultrafast phenomena in solid state materials.

As a next step, the laser output was used to generate high-order harmonics. The properties of the generated XUV when using few-cycle driving pulses were studied, both in the spectral and temporal domain. Due to the nature of HHG, where one attosecond pulse is generated for each half-cycle of the driving pulse, the short laser pulse duration results in XUV pulse trains that are short and consist primarily of only a few pulses. The number can be tuned by controlling the waveform of the driving pulse via the Carrier-to-Envelope Phase (CEP). Effort was also spent ensuring efficient HHG through the design of a high-pressure gas target, and an XUV-IR spectrometer was installed to be able to perform pump-probe experiments.

Finally, the short attosecond pulse trains were used for photoionization experiments using a photoelectron spectrometer capable of three dimensional (3D) momentum reconstruction and coincidence measurements. The importance of the temporal structure of the trains when doing XUV-IR pump-probe experiments was investigated. The coincidence capabilities of the spectrometer were utilized in order to measure single-photon double-ionization of helium.

5 Papers and Outline

This thesis consists of nine papers detailing the development and applications of the 200 kHz high-order harmonic light source.

Paper I and **Paper IV** provide a comprehensive overview of the light source and experimental beamline, from the generation of ultrashort near IR pulses, to the efficient generation of XUV through high-order harmonic generation, and the application of the beamline for the study of photoionization. **Paper I** presents the laser source and a detailed analysis of high-order harmonic generation, while **Paper IV** introduces an XUV-IR interferometer, additional analysis of the efficiency of XUV generation, and the capabilities of the photoelectron spectrometer permanently docked to the beamline.

Papers II and **V** present the measurement techniques used for the characterization of ultrashort and attosecond pulses, respectively. **Paper II** is a tutorial on the dispersion scan technique, the primary characterization method for the optical pulses used during the thesis work, and **Paper V** analyzes in detail the requirements and limitations of the RABBIT (Reconstruction of Attosecond Beating By two-photon Transitions) technique, which is used to characterize attosecond pulse trains and for applications, e.g. the measurement of photoionization delays. **Paper III** investigates the influence of the CEP on the attosecond pulse train, and develops a model for understanding high-order harmonic generation driven by few-cycle pulses.

The peculiarities of using a short attosecond pulse train for XUV-IR photoionization experiments are explored in **Paper VI**, where the angular photoelectron distribution and its CEP dependence are investigated. It is found that the distribution is asymmetric with respect to the polarization axis of the light, depending on the CEP of the driving laser, can exhibit behavior that resembles either streaking measurements or RABBIT measurements. This is understood as interference between the sequence of electron wave packets ionized by the short train, in close analogy to diffraction from multiple slits.

Paper VII, **VIII**, and **IX** are dedicated to other applications of the laser source in the field of solid-state physics and nanophotonics.

This thesis is organized as follows: In Chapter 2 we introduce basic concepts of ultrafast optics and the 200 kHz light source used in this work, as well as the characterization methods. In Chapter 3 we discuss the properties of high harmonic generation using few-cycle pulses and the practical generation concerns. Chapter 4 concerns photoionization and explains the differences between the RABBIT technique and the case with few-cycle pulses, and introduces how short attosecond pulse trains can be manipulated in order to perform pump-probe measurements in either the streaking or RABBIT regimes. Also, the first measurement of a one-photon double-ionization of helium with an attosecond source is discussed. Finally, Chapter 5 covers other applications of the laser system.

Chapter 2

Ultrafast Photonics

This thesis is dedicated to studying the interaction of extremely short intense light pulses with matter. In order to understand such interactions, it is essential to have a firm understanding of the fundamental principles that apply to ultrashort light pulses, and of the technology used to produce and characterize them. This chapter starts with an introduction to ultrafast photonics and few-cycle optical pulses, then presents the laser system used throughout this thesis, and finally discusses how the pulses have been measured and characterized. The laser was presented in detail in **Paper I**.

1 Few-Cycle Optical Pulses

1.1 Superposition of Waves

Light can be understood both as an electromagnetic wave oscillating at a certain frequency, ν, or as a photon; a massless particle with an energy $h\nu$. The wave and photon pictures are always complementary, but often one provides more insight than the other when used for the description of a specific process.

A monochromatic light wave theoretically extends infinitely in time. If more waves are present, their amplitudes are added together according to the principle of superposition, leading to interference effects. The phase of the waves, which indicates the timing of the oscillations, determines the result of that interference. Two waves with a frequency difference, i.e. a different pace of phase evolution, will, as a function of time, either add positively in a case of constructive interference, or cancel each other out due to destructive interference. The result is a beating effect.

When more waves with different frequencies are added, they can only interfere constructively in a smaller and smaller temporal region; they form a pulse, also called a wave packet. The more frequencies–the broader the spectrum of the light–the shorter the possible temporal duration.

Figure 2.1 shows the principle of superposition, where monochromatic waves with different frequencies are added together to form a short light pulse. To the left, the phase of all frequencies is the same in a single instant, and the result is a nicely confined pulse. However, if the phase of different frequency components is random the resulting summed up pulse is distorted, as can be seen to the right. The energy of the right hand pulse is no longer contained in a short time duration, and the maximum power and intensity is considerably reduced.

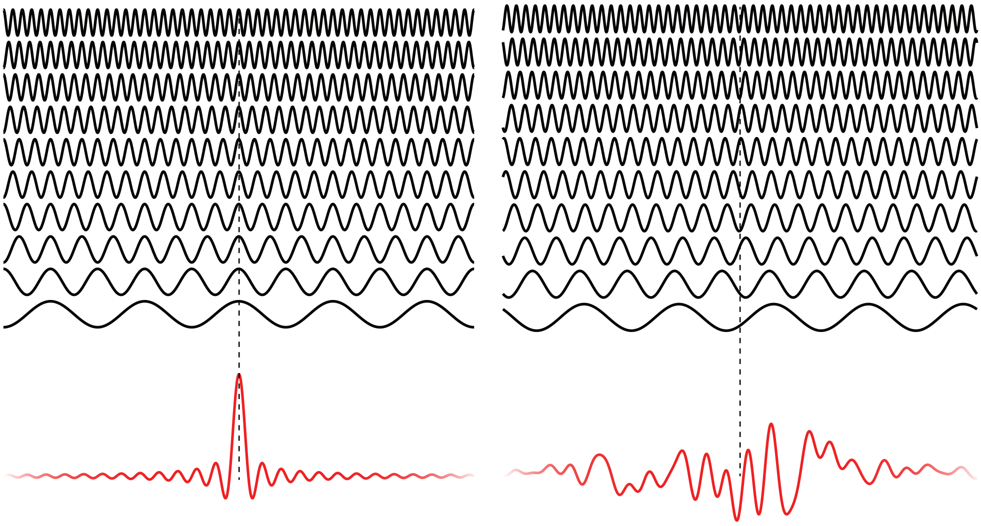

Figure 2.1: Superposition of frequency components. On the left, the different frequencies are in phase and add up to a short pulse. On the right, a random phase relation between the waves results in a chaotic waveform with lower amplitude.

1.2 The Fourier Transform and Spectral Phase

In general, a light pulse can always be described either in the temporal or spectral domain, and the two are connected via the Fourier transform:

$$\begin{aligned}\tilde{E}(\omega) &= \mathcal{F}\{E(t)\} = \int dt E(t) e^{-i\omega t}, \\ E(t) &= \mathcal{F}^{-}1\{\tilde{E}(\omega)\} = \frac{1}{2\pi}\int d\omega \tilde{E}(\omega) e^{i\omega t},\end{aligned} \tag{2.1}$$

where $\omega = 2\pi f$ is the angular frequency. Both the mathematical representations $E(t)$ and $\tilde{E}(\omega)$ are complex quantities; however, the electric field of a pulse is real and thus only half the complex spectrum is required to provide a complete representation.

In the temporal domain, a light pulse can usually be described with a carrier frequency ω_0, corresponding to the central frequency of its spectrum, and a complex envelope $A(t)$:

$$E(t) = A(t) e^{i\omega_0 t}, \tag{2.2}$$

while the spectral representation is usually decomposed as a spectral amplitude and phase:

$$\tilde{E}(\omega) = |\tilde{E}(\omega)| e^{i\phi(\omega)}. \tag{2.3}$$

While in the case of ultrafast pulses, the envelope of the pulse is generally much too short to be usefully characterized by any electronics, the spectral decomposition is particularly useful since all common spectrometers return the spectral power or intensity, $\propto |\tilde{E}(\omega)|^2$. However, since it is the spectral phase that determines the actual waveform of the pulse, as shown in Figure 2.1, measuring the spectrum alone is not enough to characterize a pulse.

It can be instructive to expand the spectral phase into a Taylor series around the central frequency ω_0:

$$\phi(\omega) = \phi_0 + \phi_0'(\omega-\omega_0) + \frac{1}{2!}\phi_0''(\omega-\omega_0)^2 + \frac{1}{3!}\phi_0'''(\omega-\omega_0)^3 + \frac{1}{4!}\phi_0''''(\omega-\omega_0)^4 + \ldots \tag{2.4}$$

The first term is an absolute phase and is referred to as the Carrier-to-Envelope Phase (CEP), which will be discussed further in Section 1.4. The second term is the linear phase or Group Delay (GD), and it corresponds instead to a shift of the pulse in time. The third term varies quadratically with frequency, called Group Delay Dispersion (GDD), and leads to a linear change of instantaneous frequency with time; this is called chirp. It also stretches the pulse duration. The Third Order Dispersion (TOD), leading to a second order variation in instantaneous frequency, and Fourth Order Dispersion (FOD) terms are also shown, since these are the dispersion terms commonly imprinted on pulses by optical elements.

Figure 2.2 shows the waveform of four different pulses with the same spectrum, but with different spectral phases: flat spectral phase (also called transform limited or Fourier-limited), GDD, TOD, and FOD, respectively. At the right, second line, observe how the oscillations

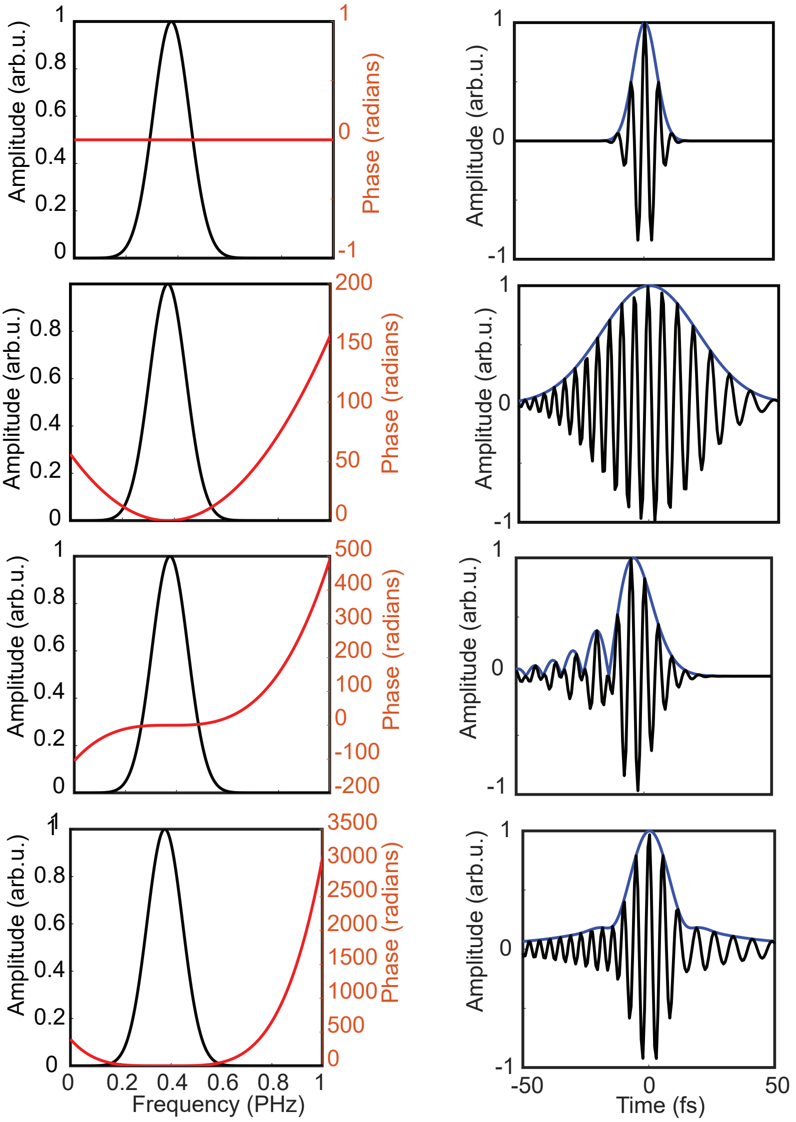

Figure 2.2: Impact of spectral phase on the pulse. The left column shows the spectrum (black) and spectral phase (red), and the right column shows the corresponding waveform (black), and the envelope (blue). From top to bottom, the rows show a flat spectral phase, GDD, TOD and FOD.

of the field are faster early in the pulse, and slower in the trailing edge. This is called negative chirp. The opposite case (low frequencies first), is called positive chirp. Also note in the right plot, third line, the characteristic pre-pulse structure which is the result of TOD.

1.3 Pulse Trains

Most laser systems do not emit single pulses, but rather a train of pulses with a certain temporal separation corresponding to the repetition rate. In the case of two pulses in the temporal domain separated by $T = 1/f_{rep}$, the total spectral amplitude can be written as:

$$\tilde{E}_{tot}(\omega) = |\tilde{E}(\omega)|e^{i\phi(\omega)} + |\tilde{E}(\omega)|e^{i(\phi(\omega)+\omega T))} = |\tilde{E}(\omega)|e^{i\phi(\omega)}(1 + e^{i\omega T}). \tag{2.5}$$

The corresponding spectrum:

$$\tilde{I}(\omega) = |\tilde{E}_{tot}(\omega)|^2 = |\tilde{E}(\omega)|^2 \cdot 4\cos^2(\omega T/2), \tag{2.6}$$

includes a cosine modulation depending on the separation between the pulses, which can interpreted as interference fringes. The maxima appear at $\omega = n \cdot 2\pi/T$, where n is an integer, and the smaller the separation of the pulses in time, the larger the spacing between the fringes in the spectral domain.

If the pulses are identical except for a phase difference, then

$$\tilde{E}_{tot}(\omega) = |\tilde{E}(\omega)|e^{i\phi(\omega)} + |\tilde{E}(\omega)|e^{i(\phi(\omega)+\omega T+\Delta\phi))} = |\tilde{E}(\omega)|e^{i\phi(\omega)}(1 + e^{i(\omega T+\Delta\phi)}), \tag{2.7}$$

which has a corresponding spectrum

$$\tilde{I}(\omega) = |\tilde{E}(\omega)|^2 \cdot 4\cos^2((\omega T + \Delta\phi)/2). \tag{2.8}$$

The spacing between the maxima remain the same but the positions are shifted due to the phase difference.

The interference in the spectral domain is very similar to spatial interference of waves, as demonstrated most famously in Young's double slit interference experiment [27]. Two waves emitted by slits separated by a distance d results in an interference pattern on a distant screen with a fringe separation inversely proportional to the distance of the slits, $1/d$, in exact equivalence with the frequency separation being inversely proportional to the temporal separation, $\Delta f = 1/T$. Figure 2.3 shows an illustration of a double-slit experiment. To the right a small piece of material has been inserted in front of one of the slits, which introduces a phase shift and a subsequent shift of the interference fringes as in Equation 2.8.

Interference in the Fraunhofer regime, i.e. when the curvature of the wave front is negligible, can be shown to correspond to the Fourier transform of the aperture causing the interference—for example a slit system. The Fraunhofer regime is easily reached through simple free space propagation of the light from the near field (close to the slits), to the far field (the distant screen), which disperses the angular components onto real space, or via

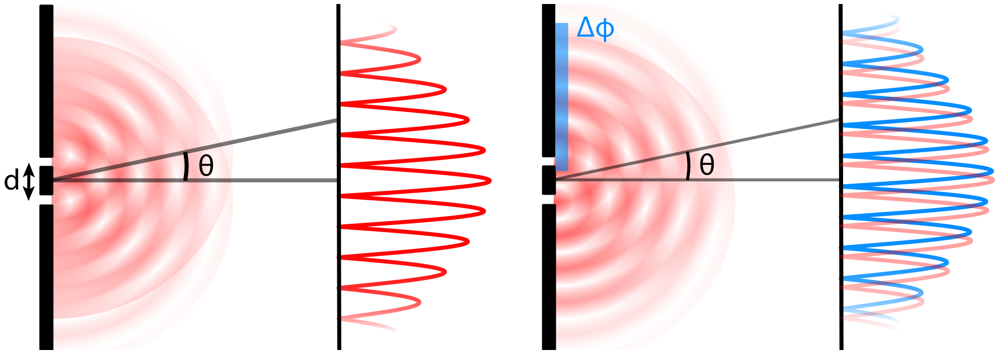

Figure 2.3: Double-Slit Experiment. On the left, a simple double slit experiment with a slit separation d, resulting in spatial interference fringes (red). To the right, the addition of some material resulting in a simple additional phase is added, and the interference fringes are shifted (blue line).

a collimating lens. Slit experiments in space thus are an excellent analogy to the interference effects in the temporal and spectral domain, where the slits correspond directly to the temporal shape of the field and the pattern on the screen to the spectrum.

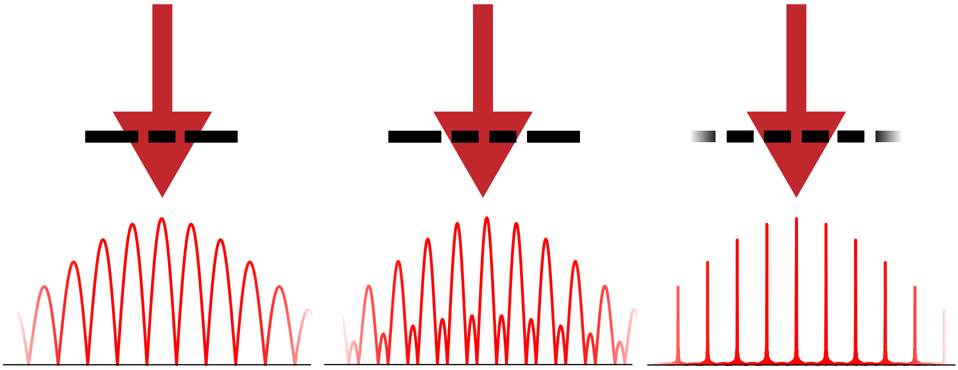

Figure 2.4: Interference From Multiple Slits. From left to right, interference patterns from two, three, and many slits, are shown. In the middle, the three slits result in narrower peaks and the appearance of submaxima, and on the right, a large amount of slits result in narrow interference maxima.

Accordingly, the effects of moving from the case of two pulses towards a pulse train can be understood by considering what happens when additional slits are added to the double slit. The introduction of a third slit will add additional interference. The spacing of these interference fringes will be proportional to the distance between the first and third slit which, assuming the separation between all slits is constant, is $\propto 1/2d$. The coherent sum of the two interference patterns results in narrower interference peaks, as well as the addition of sub-maxima. In a general multi-slit experiment the resulting interference pattern on a screen far away can be expressed as

$$I(\theta) \propto \frac{\sin^2(N\delta)}{\sin^2(\delta)}, \tag{2.9}$$

where N is the number of slits, $\delta = \frac{\pi}{\lambda} d\theta$, with λ as the wavelength of the light, and θ is the angle from the slit system to the screen.

When continuing to increase the number of slits, i.e. N in Equation 2.9, the width of the fringes will continue to narrow, and the strength of the sub-maxima will decrease. In the case of an infinite slit system, the fringes will be infinitely thin. Coming back to the temporal domain, the same result can be expected in the case of a long pulse train where the pulses have a fixed separation in time, such as the output of a pulsed laser. With a high repetition rate and identical pulses, these trains produce in the frequency domain what is called a frequency comb; a series of very narrow spectral lines separated by $T = 1/f_{rep}$. The idea of pulse trains and corresponding spectral combs is fundamental to this thesis work.

1.4 Carrier-to-Envelope Phase

The absolute phase ϕ_0 in Equation 2.4, the CEP, does not change the envelope of a pulse and is therefore often unimportant when it comes to standard laser pulses. However, it becomes essential in the few-cycle regime, since it determines the relative position of the carrier wave under the envelope. With pulses of durations of the same order of magnitude as the oscillation period, this phase can dramatically change the shape of the actual waveform.

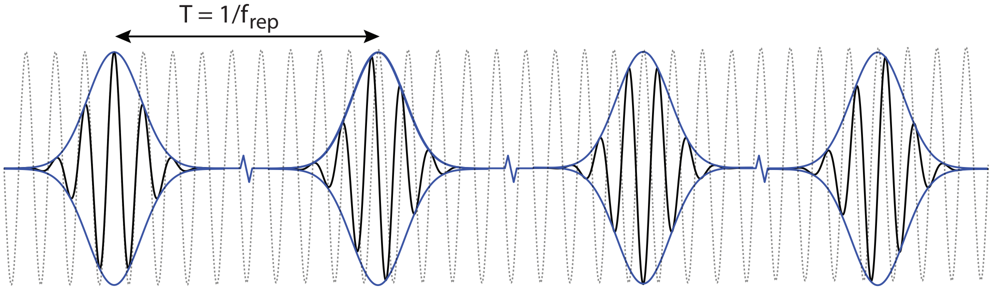

Figure 2.5: CEP. Four different pulses with a separation of T, corresponding to a repetition rate of f_{rep}. The CEO between pulses is $\pi/2$, and their CEP, from left to right, is 0, $\pi/2$, π, and $3\pi/4$.

Figure 2.5 shows three different pulses, identical except for their CEP. The dotted gray line shows a reference wave, which corresponds to zero absolute phase. In this case, in the leftmost pulse, the maximum oscillation amplitude coincides with the peak of the envelope, and the central half-cycle of the pulse has the maximum electric field amplitude. When the CEP is shifted by $\pi/2$, as for the second pulse, this is no longer the case. Here the two central half-cycles reach the same magnitude, although the sign differs. In the third pulse, the CEP is shifted by π and the amplitude is now maximized again, but with opposite sign, and the fourth pulse is in the same way the inverse of the second.

One important feature of these few-cycle pulses is that the symmetry of the pulse in the polarization direction is broken. Integrating a single frequency oscillation over all time always gives zero, and the same is essentially true for long pulses. In this case, however, the integration only yields zero for the $\pm\pi/2$ case, i.e. the second or forth pulse. This symmetry breaking property has several important implications which will be discussed further in the thesis.

In the pulse sequence in Figure 2.5, the CEP changes from pulse to pulse with $\pi/2$. The CEP-slip from pulse to pulse can be associated with the Carrier-to-Envelope Offset (CEO) frequency, f_{CEO}. If a laser system emits pulses at a certain repetition rate f_{rep}, the CEP will repeat itself with a frequency determined by the CEO so that $f_{CEO} = f_{rep}\varphi_{CEO}/2\pi$.

While the generation of near-identical pulses is possible with a modern oscillator, where the spectrum is identical from pulse to pulse, the phase evolution in one roundtrip of a cavity is not generally equal to multiples of 2π. This means there will be some CEP phase slip, which shifts the positions of the frequency comb lines (or more generally the positions of interference maxima as in Equation 2.8) similarly to a piece of glass in a slit experiment, so that a given comb line has a frequency of

$$f_m = f_{rep}\left(m + \frac{\varphi_{CEO}}{2\pi}\right) = mf_{rep} + f_{CEO}, \tag{2.10}$$

where m is an integer. This is shown in Figure 2.6, where the black comb has an offset compared to the red, equal to f_{CEO}.

The field of frequency comb spectroscopy uses the narrow spectral width of the lines produced by stable pulse trains, and the ability to shift them via controlling the f_{CEO} [28]. However, clearly separated spectral lines in a frequency comb also require a very high repetition rate, on the order of hundreds of MHz—at 200 kHz, which is the final repetition rate of the laser system used in this thesis, the line separation is too small to be easily resolvable or useful.

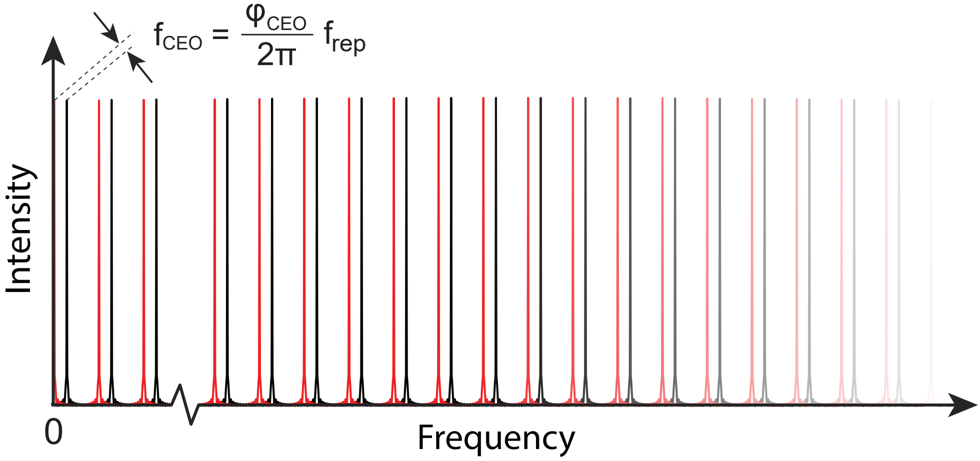

Figure 2.6: Comb Shift From CEO. The black frequency comb is shifted compared to the red, with a frequency that is proportional to the CEO phase (φ_{CEO}) and the repetition rate (f_{rep}).

2 Laser Technology

Since its invention in the 1960s [1, 29], the laser has been an indispensable scientific tool, leading to the discovery of a plethora of novel phenomena. The technological development of lasers has pushed science in new directions, and the advent of more powerful and reliable lasers has been a prerequisite for many exciting discoveries.

Very soon after the laser's invention, the concept of mode-locking was developed [30–33]. A mode-locked oscillator is designed so that the longitudinal modes of the laser cavity (i.e. the frequency comb) are phase locked, which results in a train of short pulses. Together with the development of the CPA technique [5], this gave rise to the field of ultrafast time-resolved studies, where the short time duration of the pulses is used to investigate very short dynamic processes [6]. The CPA technique consists of first stretching the pulses in time; this maintains the pulse energy but dispersed over a longer time interval, therefore lowering the intensity. This long pulse can then be amplified without strong non-linear effects or damage, and then compressed again back, now with a higher power than was previously obtainable; see Figure 2.7. The technique was awarded the Nobel Prize in 2018.

Pulses with a broad spectrum, which can thus be temporally compressed, are often produced with Ti:Sa as gain medium [3, 4]. Ti:Sa oscillators can produce pulses with a central wavelength of 800 nm, with a pulse duration as short as <6 fs, corresponding to a two-cycle pulse. Ti:Sa based CPA lasers have, however, a few drawbacks. One is the so called gain bandwith narrowing, due to the fact that the more intense parts of the spectrum will be

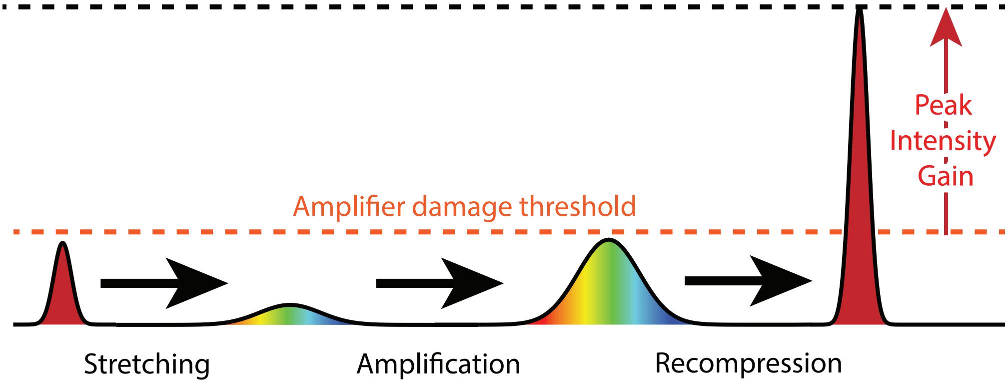

Figure 2.7: Chirped Pulse Amplification. The original pulse is stretched in time, lowering its peak intensity. It is amplified to a point below the damage threshold, and then re-compressed, reaching much higher intensities than would be possible without CPA.

amplified more than the weaker part, effectively limiting the available bandwith. A large quantum defect, which is the energy difference between the pump photon and the laser photon, also means that this energy difference will be dissipated as heat, which requires advanced cooling techniques. The amount of heat that needs to be cooled away is dependent not primarily on the peak energy or peak power of the pulses, but rather the average power. To reduce the average power, but retain the desired high peak power, Ti:Sa systems are forced to operate at a lower repetition rate, typically in the low (1-10) kHz range. Combined with post-compression techniques, ultrashort high-energy pulses have been available from such systems for more than two decades [34, 35]

Fiber based laser systems, with smaller quantum defect and thus less heat production, allow increasing the repetition rate and thus the average power enormously. Ytterbium, for example, is pumped at 970 nm for lasing at 1030 nm [36]. It can also be pumped continuously due to the long lifetime of the upper state. However, these gain materials do not support a bandwidth as broad as the one of Ti:Sa, and thus have a longer transform limit.

The 200 kHz laser system used in this thesis work combines the broadband spectrum of a Ti:Sa front end with the higher repetition rate of a fiber based system though Optical Parametric Amplification (OPA). Amplification of optical pulses using parametric interactions was observed already shortly after the invention of the laser [37], and was combined with the CPA technique in 1992 [38]. Modern Optical Parametric Chirped Pulse Amplifiers (OPCPA) operate at a variety of repetition rates and wavelengths, and typically reach high conversion efficiencies of up to 30% [39].

2.1 Non-Linear Parametric Processes

When light interacts with matter, it distorts the electron cloud and induces a polarization density, **P**. The strength of this polarization density does not scale linearly with the electric field strength at high intensity, but can be expressed as a power series:

$$\mathbf{P} = \epsilon_0(\chi^1\mathbf{E} + \chi^2\mathbf{E}^2 + \chi^3\mathbf{E}^3 + ...), \tag{2.11}$$

where $\chi^{(n)}$ is the n-th order (material-dependent) susceptibility.

To understand the results of non-linear terms, consider an electric field consisting of two different frequencies:

$$E = E_1 e^{i\omega_1 t} + E_2 e^{i\omega_2 t} + c.c. \tag{2.12}$$

When that field interacts with a material with a second-order non-linearity, the polarization induced in the material becomes

$$\begin{aligned} P \propto (E_1 e^{i\omega_1 t} + E_2 e^{i\omega_2 t} + c.c.)^2 =& |E_1|^2 + |E_2|^2 \\ & 2E_1^2 e^{i2\omega_1 t} + E_2^2 e^{i2\omega_2 t} + \\ & 2E_1E_2 e^{i(\omega_1+\omega_2)t} + E_1E_2 e^{i(\omega_1-\omega_2)t} + c.c. \end{aligned} \tag{2.13}$$

Interestingly, the polarization density now contains oscillating terms at new frequencies. The original frequencies have been doubled; the $2\omega_1$ and $2\omega_2$ terms, which are called Second Harmonic Generation (SHG). The sum and difference of the two frequencies, $\omega_1 + \omega_2$ and $\omega_1 - \omega_2$, can also be seen, and this is called Sum Frequency Generation (SFG) and Difference Frequency Generation (DFG), respectively, as well as a non-oscillating term, called optical retification. The process can also be understood in the photon picture; e.g. for SHG, two photons with energy $h\nu$ combine to make one photon with the higher energy $2h\nu$. It can be noted that when a broadband pulse is used for SHG, the process is more complex, since several combinations spectral components can through SFG combine to the same frequency.

Figure 2.8 illustrates, to the left, how different frequency components in a broadband spectrum can through second-order non-linear interactions generate new spectral content. To the right the energy conservation is shown by energy-level diagrams for the three processes; SHG, SFG, and DFG. OPA is a form of DFG, where a high frequency pump photon is converted into a signal photon and idler photon.

Not all of these processes are observed simultaneously—in order for energy transfer to actually occur, the process also needs to be phase matched. In the case of, for example, SHG in a crystal, the second harmonic light generated in the beginning of the crystal will

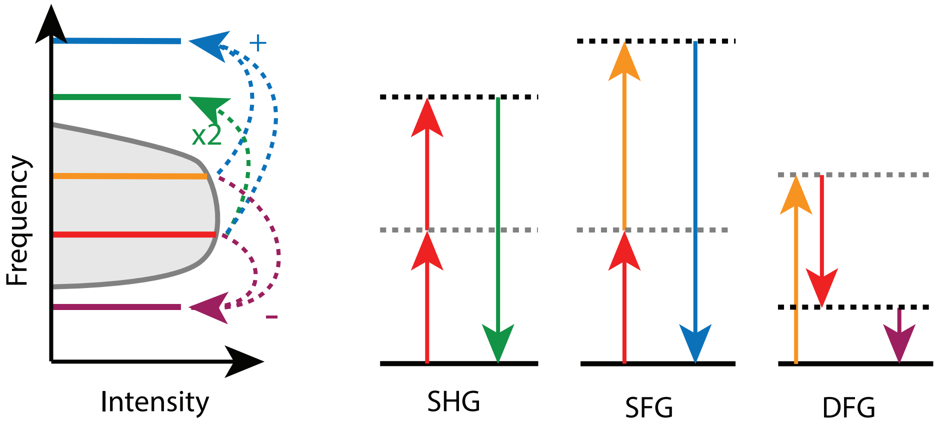

Figure 2.8: Non-Linear Frequency Conversion. Left: different three wave mixing processes possible with a broadband spectrum, SHG (dashed green arrow), SFG (dashed blue arrows), and DFG (dashed purple arrows). To the right are shown the corresponding energy level diagrams.

propagate through the material, acquiring a certain phase:

$$\tilde{E}(\omega, z) = |\tilde{E}(\omega)|e^{i\omega t + ik(\omega)z} \tag{2.14}$$

where $k = nk_0 = n\omega_0/c_0$ is the wavevector, and n is the refractive index. The phase of the newly generated second harmonic at any point z is determined by the phase of the fundamental. In a dispersive material, the refractive index n differs between different frequencies, and thus this leads to a phase mismatch between the second harmonic generated at different points in the crystal. The phase mismatch, $\Delta k = 2k(\omega) - k(2\omega)$, will increase until a distance L where $L\Delta k = \pi$. At this point, the newly generated SHG will be completely out of phase with what was generated at z=0, and no second harmonic can be observed.

Phase matching in an OPA can be expressed mathematically as:

$$\Delta \mathbf{k} = \mathbf{k}_p - \mathbf{k}_s - \mathbf{k}_i, \tag{2.15}$$

where vector notation is used to allow the possibility of non-collinear propagation, and indices p, s,and i indicate pump, signal, and idler, respectively. In a collinear configuration, efficient phase matching can only be achieved in a very small spectral range. However, by using non-collinear configurations, the fact that the angle of only two of the three components have to be fixed can be used to phase-match spectra supporting few-cycle pulses, which allows for use of this technique in ultrafast optics. This is referred to as Non-collinear Optical Parametric Amplification (NOPA). Both collinear and non-collinear OPA is achieved through the use of birefringent crystals. In a birefringent material the refractive index is different depending on the polarization of the light as well as the relative orientation of the crystal structure with respect to the incoming light.

In uniaxial birefringent crystal the index of refraction of the extraordinary wave depends on the angle θ between the propagation axis and the optical axis of the crystal as such:

$$\frac{1}{n(\theta)} = \frac{\cos^2(\theta)}{n_o^2} + \frac{\sin^2(\theta)}{n_e^2} \tag{2.16}$$

where n_o and n_e are the refractive indices for waves with polarization perpendicular and parallel to the optic axis, respectively. Thus the angle θ and the angle α between the two beams can be varied to complete the triangle shown in the left of figure 2.9 and minimize Δk. Using this geometry, the phase mismatch can be expressed as

$$\Delta k = \sqrt{k_p^2 + k_s^2 - 2k_p k_s \cos\alpha} - k_i. \tag{2.17}$$

If the phase mismatch is not precisely zero, the possible phase matched effciency for a crystal of length L is then proportional to $\mathrm{sinc}^2(\Delta kL/2)$.

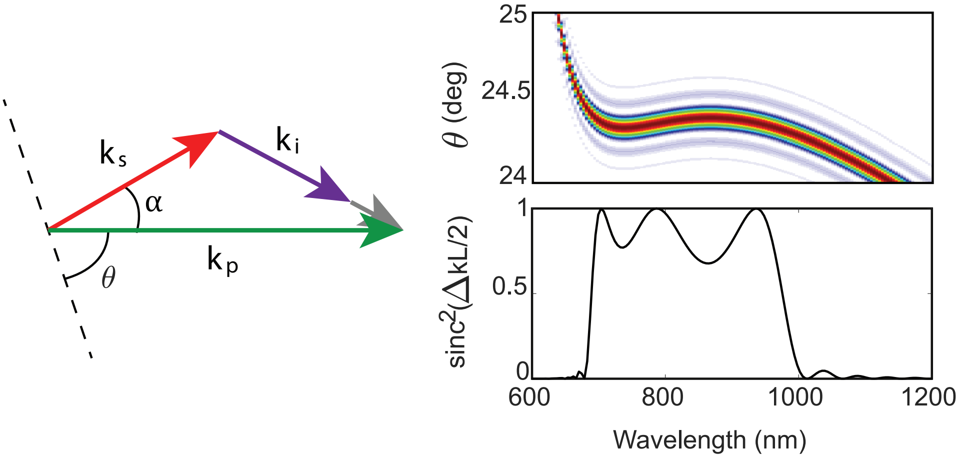

Figure 2.9: NOPA phase mismatch and amplifier gain. The non-collinear geometry for OPA is shown to the left. The upper right shows the phase matching curve for BBO, and on the bottom, the broadband gain curve for $\alpha = 2.44°$ and $\theta = 24.44$.

The most common crystal used for NOPAs in the near IR spectral region is β barium borate (BBO), where a near octave spanning phase matching bandwidth can be achieved with the so called "magic angle", which can be found at $\alpha = 2.44°$ and $\theta = 24.44°$ [40–42]. In the upper right of Figure 2.9, the phase matched efficiency is shown as a function of wavelength and crystal angle θ. To the lower right, the gain curve for an optimal angle $\theta = 24.44°$ is shown, demonstrating the broad spectral region in which amplification is possible in ideal conditions. Note that the ideal phase matching angle varies up to the first digit depending on which Sellmeier equation is used to describe the refractive index; here coefficients from [43] have been used.

Even though the phase mismatch is close to zero in this broad region, it is clear that it cannot be completely cancelled. This remaining mismatch results in a loss of relative gain, as seen in the bottom right of Figure 2.9, and also influences the phase of the amplified pulse [44]. Mathematically, the amplification phase can be written as:

$$\varphi_{amp} = \Delta kL/2 + (\Delta k\gamma_s^2)/2 \int dz \frac{1}{f + \gamma_s^2} \tag{2.18}$$

where γ_s is the gain and f is the fractional depletion of the pump beam. Thus if the gain remains low, an additional phase directly proportional to $\Delta kL/2$ is expected. A more complicated behavior is expected as soon as significant gain is achieved.

2.2 200 kHz Laser Source

The 200 kHz laser system at the Lund Laser Center provides few cycle near IR laser pulses, after amplification through two NOPA stages reaching an energy of 15 μJ after compression. A schematic overview of the laser system is shown in Figure 2.10.

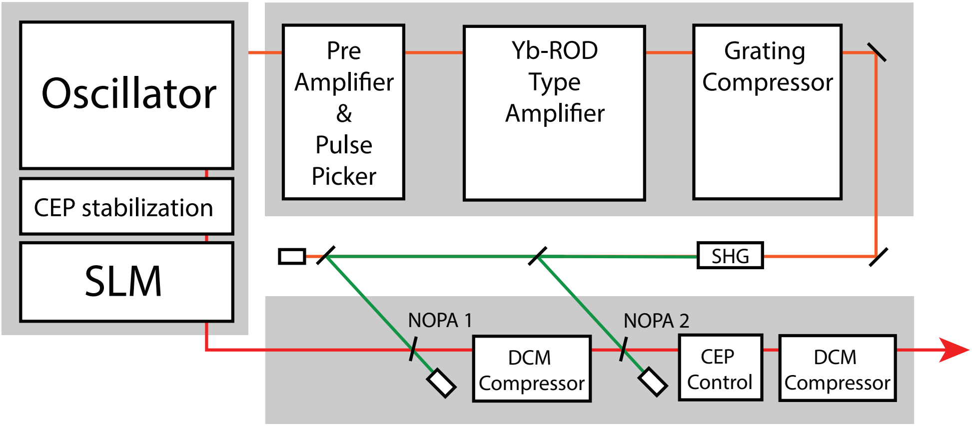

Figure 2.10: Laser layout. Simple schematic of the laser chain, consisting of the oscillator source, the amplification of the 130 nm pump, and the NOPA stages.

The oscillator front-end (VENTEON) provides ultrabroadband pulses with sub 6-fs pulse duration at 80 MHz repetition rate, with a stabilized $f_{CEO} = f_{rep}/4$. A small portion of the oscillator spectrum around 1030 nm is sent to a fiber pre-amplifier. This consists of a chirped fiber Bragg grating, three amplification stages and two pulse pickers, reducing the repetition rate to 200 kHz. The output is sent on to a 1 m long Yb-doped rod-type amplifier (NKT Photonics), delivering an output power of approximately 50 W. After recompression by a grating compressor, the power is reduced to $\sim$35 W (175 μJ), which is used to generate the second harmonic at 515 nm. The resulting $\sim$18 W of green is split into two arms (4W vs. 14W) and used to pump two NOPA stages.

The remaining oscillator output is sent through a Spatial Light Modulator (SLM), capable of both phase and amplitude shaping [45], which is used to pre-compensate for primarily third-order phase distortions inherent to the parametric amplification process. The pulses are then sent to the NOPA stages with two 2 mm thick BBO crystals in the magic angle configuration. The first stage amplifies the oscillator seed from 10 mW (0.125 nJ at 80 MHz) to $\sim$250 mW, and the second stage amplifies the pulses further to $\sim$3.8 W (19 μJ). Finally, the pulses are compressed by double chirped mirrors (VENTEON). The laser delivers output pulses with a duration of <6 fs with an energy of 15 μJ. There is another synchronized rod-type amplifier currently used to pump a mid-IR (MIR) OPCPA.

During the thesis work, the rod-type fibers were upgraded after a move of the laser system, resulting in a significant increase in output power. For the experiments in **Paper I**, **III**, and **VI**, the output power of the laser was 9 μJ. The upgrade resulted in a 50% increased power without any loss of pulse duration or quality. While the system has previously been able to reach pulse energies sufficient for generation of high harmonics, see Chapter 3, the goal of the beamline is to perform pump-probe type experiments. This requires that a portion of the power can be separated before generation in order to provide the probe. Previously, only very little power could be spared for the probe arm, making attempts of pump-probe experiments unsuccessful—since the upgrade, this problem has been solved, as shown in Chapter 4 and **Paper IV**.

2.3 Characterization

One of the main difficulties in generating ultrashort pulses is that they cannot be easily measured. As mentioned earlier, common optical spectrometers measure only spectral power and not the phase, and thus all time information is lost. Since many applications of broadband laser sources depend on short pulses, the development and proper utilization of characterization techniques for ultrashort pulses is thus essential in a research group that claims to operate in this challenging regime.

A number of different techniques for characterizing very short pulses exist, see for example [46] for an overview. A few methods are worth mentioning. The SPIDER (Spectral Phase

Interferometry for Direct Electric-field Reconstruction) technique relies on self-referenced spectral interferometry to find the spectral phase [47]. In the FROG (Frequency-Resolved Optical Gating) technique [48, 49], the spectrum of the second harmonic generated by two time-delayed replica pulses is measured, generating a 2D trace from which the spectral phase can be retrieved through iterative algorithms. A third possibility is the MIIPS (Multiphoton Intrapulse Interference Phase Scan) approach [50], where the second harmonic is measured as the phase of the pulse is manipulated with the help of a spectral phase shaper, resulting in a similar trace as in FROG.

All of these techniques adequately characterize ultrashort pulses, and each have their own advantages. In this thesis, the dispersion scan (d-scan) technique [51], which was developed in Lund and Porto, has been used throughout. It is conceptually similar to the MIIPs approach. The d-scan is the topic of **Paper II**, and used in **Paper I**, **III**, **IV**, and **VII**. The spatio-temporal characterization used in **Paper I** is also presented here briefly.

2.3.1 Second Harmonic Dispersion Scan

In the d-scan, variable dispersion is added around the optimal compression point of the pulse while the SHG spectrum is measured. First the pulse is negatively chirped, and then positive dispersion is added past the compression point until the pulse is positively chirped. A d-scan setup typically consists of a pair of dispersive wedges and a chirped mirror compressor; the chirped mirrors provide a constant negative phase, overcompressing the pulse, and the amount of positive dispersion can then be varied by changing the wedge insertion. The pulse is then focused into a crystal for second harmonic generation, and the spectrum of the second harmonic, which depends strongly on the spectral phase of the fundamental, is recorded as a function of wedge insertion. Other implementations of the d-scan method are presented in **Paper II**.

The simplicity of the approach is evident in Figure 2.11, showing a schematic of the setup. Many modern laser systems use chirped mirror compressors, which consists of mirrors and a wedge pair, as a part of the laser itself. In such setups the only needed addition is in principle a lens, a second harmonic crystal, and a spectrometer. This is the case in the 200 kHz system used in this thesis. In practice, a few additional things must be considered: the second harmonic crystal should be able to phase match the whole spectrum simultaneously, and the dispersive elements must be able to provide a dispersion window large enough to stretch the pulse significantly both the positive and negative direction.

Mathematically, the d-scan can be described in the following way. Propagation though a transparent dispersive medium is represented by a simple multiplication with a phase factor in the spectral domain:

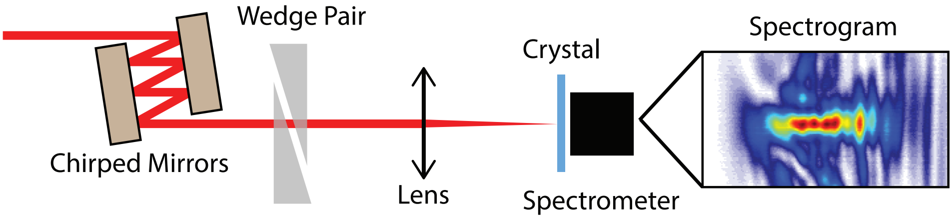

Figure 2.11: Dispersion Scan. The beam, coming from the left, passes double chirped mirrors, providing negative chirp, and then a wedge pair with a variable insertion. The beam is focused into an SHG crystal, and the SHG spectrum is recorded as a function of wedge insertion to acquire a d-scan trace.

$$\tilde{E}(\omega,z) = |\tilde{E}(\omega)|e^{i\phi(\omega)}e^{in(\omega)k_0(\omega)z} \tag{2.19}$$

The non-linear second harmonic interaction is proportional to the square of the electric field in the time domain:

$$E_{SHG}(t,z) \propto \left(\int \tilde{E}(z,\omega)e^{i\omega t}d\omega\right)^2 \tag{2.20}$$

The measurement is performed in the spectral domain, and the spectral power is recorded with a spectrometer:

$$S(\omega,t) \propto \left|\int E_{SHG}(t,z)e^{-i\omega t}dt\right|^2 \tag{2.21}$$

which yields an expression for the total SHG signal as:

$$S(\omega,t) \propto \left|\int \left(\int \tilde{E}(\omega)e^{i\omega t}e^{in(\omega)k_0(\omega)z}d\omega\right)^2 e^{-i\omega t}dt\right|^2 \tag{2.22}$$

Figure 2.12 shows d-scan traces for pulses with a few different spectral phases. The same pulses as in Figure 2.2 are shown. The different orders of spectral phase terms result in clearly identifiable features in the trace; e.g. a third order phase results in a tilt of the observed trace, while a second order term simply shifts the trace along the glass insertion axis. The d-scan trace is intuitive to interpret by eye and provides instantaneous feedback regarding the pulse quality, which is invaluable during laboratory work.

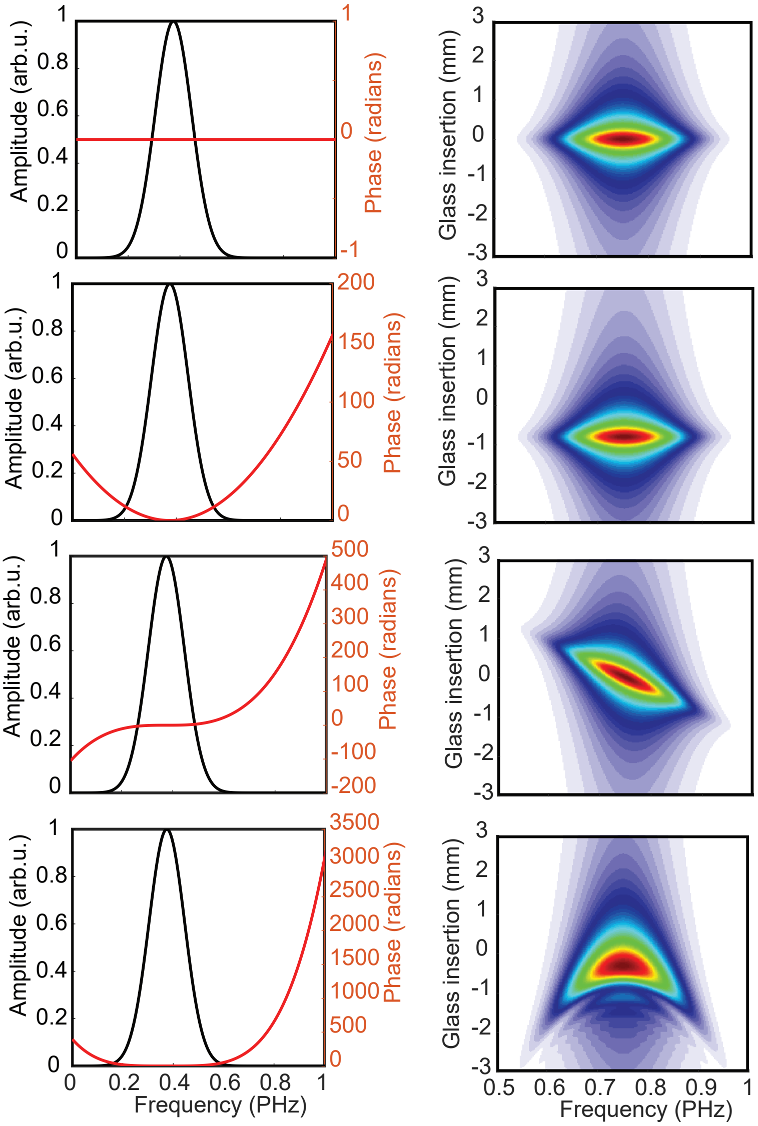

Figure 2.12: Dispersion Scan Traces. The left column show spectrum (black) and spectral phase (red), and the right column shows the corresponding calculated d-scan trances. From top to bottom, the rows show: a Fourier-limited pulse with a flat phase, a pulse with applied GDD, TOD, and FOD, respectively.

The d-scan trace provides access to the spectral phase and thus the temporal characterization of the pulse through iterative algorithms. These algorithms aim at finding the pulse that as closely as possible replicates a measured trace. In principle, standard least-squares solvers can be implemented in a relatively straightforward manner, by calculating an error between the measured and retrieved case and letting the solver minimize the error. In early works on the d-scan, the Nelder-Mead algorithm, also called downhill simplex method, was used [51, 52], giving robust results. Another retrieval algorithm which can retrieve both spectral amplitude and phase was introduced in [53], and is a form of constraint-based inversion algorithm inspired by early work on diffractive imaging [54]. Similar approaches have previously been implemented for FROG [55, 56].

Apart from pulse characterization, the d-scan has been used to study the parametric amplification process. For example, we measured the parametric amplification phase introduced in Equation 2.18. Figure 2.13, shows, to the left, the spectrum of the un-amplified seed (gray) and after amplification in one NOPA stage with increasing pump power (light to dark blue), corresponding to 150 mW, 200 mW, and 300 mW of output power. To the right the phase difference between the un-amplified signal and the three increasing amplification conditions is shown in the color of the corresponding spectrum. The calculated amplification phase according to 2.18 is shown in dashed red. The phase gained through amplification follows this curve for low gain. As the power increases additional structure can be seen, particularly noticeable around 900 nm, where parasitic SHG is expected.

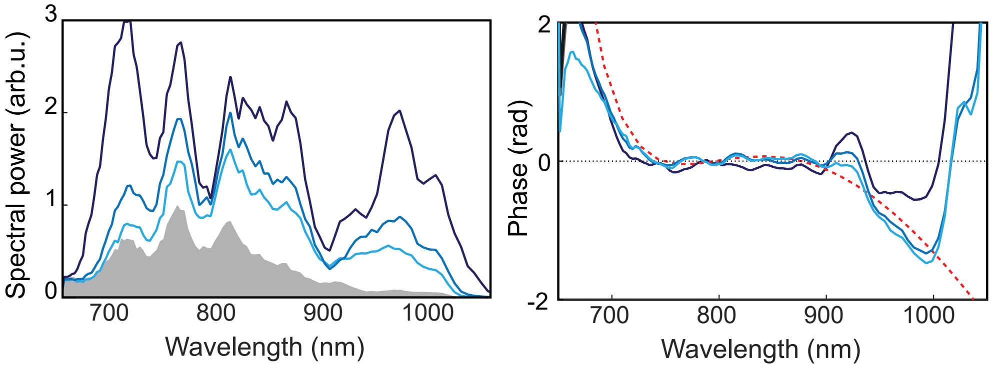

Figure 2.13: Phase gain through NOPA amplification. Spectrum (left) and spectral phase (right), for different levels of amplification. In gray, the original spectrum. Lighter colors correspond to lower amplification. The calculated amplification phase is plotted as a red curve to the right.

This amplification phase is unavoidable when using the NOPA technique. The resulting spectral phase will be dominated by this primarily third-order feature, leading to a significant amount of power being dispersed from the main pulse to pre- or post-pulse structures. As the amplification phase is well behaved and predictable, the spectral phase of the seed pulses can be pre-compensated in the pulse shaper, where the inverse phase is applied. This results in pulses with an overall almost flat spectral phase.

Figure 2.14 shows the result of a real d-scan measurement of the final output pulses of the

200 kHz laser system, as presented in **Paper IV**. Although the trace shows much more structure than the simple pulses presented in Figure 2.12, the fact that the overall trace is almost entirely flat (i.e. the center of mass along the glass insertion is similar for all wavelengths) already reveals a short time duration. The retrieved spectral phase is also shown. The FWHM time duration is 5.8 fs. The pulse energy for this measurement was approximately 15 μJ.

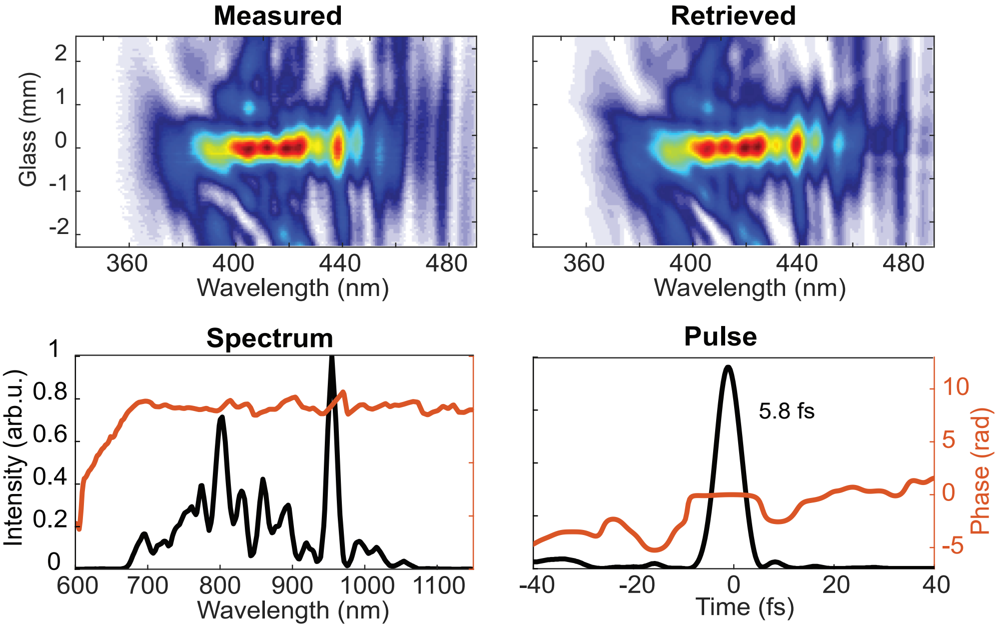

Figure 2.14: Pulse Characterization of 200 kHz Source. Top row shows the measured and retrived d-scan trace. Bottom row show the retrieved spectrum and spectral phase, to the left, and the corresponding pulse, to the right.

2.3.2 CEP Stabilization

As presented in **Paper I** and **IV**, the laser system used for this thesis work is CEP stabilized. The 200 kHz system in Lund uses two different methods for CEP stabilization, one for the oscillator output and one to stabilize the slow drift from the laser chain, both of which are based on f:2f interferometry.

The method used to stabilize the oscillator output uses the frequency comb properties. When generating the second harmonic of a frequency comb, an offset between the fundamental and up-converted modes will be introduced, which depends on the f_{CEO}. This offset can be written as:

$$2f_m - f_{2m} = (2mf_{rep} + 2f_{CEO}) - (2mf_{rep} + f_{CEO}) = f_{CEO}, \qquad (2.23)$$

i.e. the beating of the fundamental and the second harmonic is the CEO frequency, and indirectly the phase slip between pulses. An Avalanche Photo Diode (APD) is used to detect the beating signal between the fundamental and the second harmonic, which is sent to Radio-Frequency (RF) analyzer. The beating frequency, i.e. f_{CEO}, can then be locked by modulating the oscillator pump power, and thus cavity dispersion, through e.g. an Acousto Optical Modulator (AOM) or the pump driver directly [57]. If the spectrum is octave spanning, i.e. contains frequencies f_1 and f_2 so that $f_2 = 2f_1$, the fundamental and second harmonic spectrum will overlap already; otherwise, CEP-maintaining white-light-generation can be used for broadening. Note that this method stabilizes the carrier-to-envelope *offset* (f_{CEO}), not the absolute carrier-to-envelope *phase* (CEP).

In the system used in this thesis, the f_{CEO} is stabilized to $f_{rep}/4$, meaning that every fourth pulse in the pulse train has the same CEP. Since the laser only amplifies every 400th (which is dividable by four) pulse due to the reduction of the repetition rate from 80 MHz to 200 kHz, the CEP of the laser output is fixed. For **Paper VII**, however, the pulse pickers were set to result in a final repetition rate of 199 kHz in such a way that every other pulse has the same CEP and the CEP between consecutive pulses is flipped by π.

Through the amplifier chain there is a possibility of additional CEP drift, due to e.g. thermal drift, power fluctuations, or mechanical vibrations. This drift can be assumed to be slow, but must still be corrected for if the source is to operate in a stable condition over hours or days. In order to do this, a small portion of the amplified spectrum is split off before compression and sent to an additional f:2f interferometer for CEP detection. Since the repetition rate is reduced to 200 kHz, the spectral separation of the frequency modes is now too small to be easily detectable. Additionally, it is not possible to stabilize the CEO to zero, where the offset between the two combs would be nonexistent. Another method for stabilization is used instead, based on the interference in a small spectral region [58]. The spectrum must now first be broadened through white light generation, to be octave spanning, and then SHG is generated. The region of spectral overlap is filtered out, and the temporal separation of the fundamental vs. the second harmonic results in interference fringes. Although there is no straight-forward relation between these fringes and the actual value of the CEP, stabilizing the fringe position corresponds to a stabilization of the CEP.

In general, this slow feedback loop detection is done with a standard fiber spectrometer, with a minimum read-out time of around 1 ms, meaning that the measurement is averaged over many pulses. While this is certainly enough to stabilize for a slow continuous drift, any measurement done will not accurately reflect the CEP fluctuations. To accurately measure the CEP-instability of the laser chain, a single-shot setup is required. This was achieved

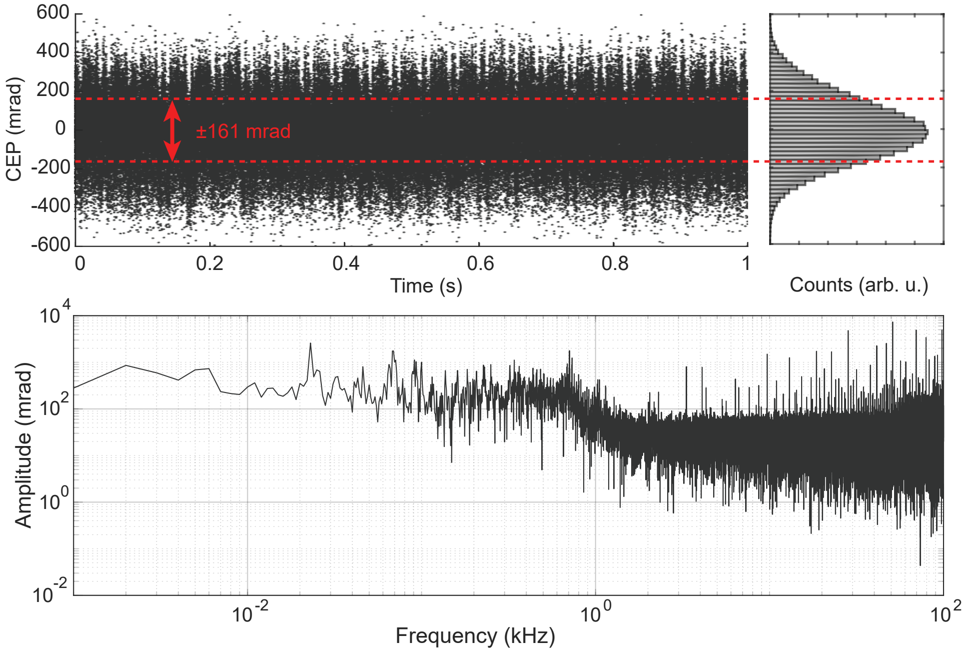

Figure 2.15: Single-shot CEP characterization. Top row shows the single shot CEP measurement, and to the right, statistics in the form of a histogram. The RMS is indicated in red. The bottom row shows the amplitude spectrum of the same measurement.

for our system by the use of a high-speed line camera, capable of >200kHz read-out rate, to record the spectral interference. The results in Figure 2.15, as presented in **Paper IV**, show an achieved short-time Root Mean Square (RMS) error of the CEP corresponding to 160 as. The repeated structures in the measured CEP can be attributed to small power fluctuations that originate from the pre-amplifier due to a slight mismatch between the pulse pickers, which has been rectified in a recent upgrade. They are also visible in the amplitude spectrum as a series of structures below 100 Hz, shown in Figure 2.15, bottom.

2.3.3 Spatio-Temporal Characterization

In a system where the available pulse energy is already low, a reduction of focused intensity is highly detrimental, especially for a highly non-linear processes. In HHG, which the laser is primarily designed to drive, even a very small change in intensity may severely reduce the conversion efficiency. Furthermore, distortions of the fundamental will impair the quality of the generated XUV attosecond pulses.

One possible source of such intensity reduction is spatio-temporal couplings, which occur when a the field of a pulse cannot be completely separated into a product of spatial and temporal factors, i.e. $E(x, y, t) \neq g(x, y) \cdot T(t)$. For a thorough background on spatio-temporal couplings in ultrashort pulses see [59]. Two relevant spatio-temporal couplings are so called spatial and angular chirp. If a pulse has angular chirp, the different spectral components propagate in different directions. This eventually leads also to a spatial chirp, i.e. a separation between spectral components in real space. It is possible to have spatial chirp without angular chirp—this, however, does not automatically reduce focusability. Any angular chirp, however, will reduce focusability and the maximum achievable intensity.

In light of their possible deterious effects, characterizing the spatio-temporal couplings in the system is crucial in order to ensure high quality pulses. Such a characterization investigates the quality of the pulse regarding the focusability, as presented in **Paper I**.

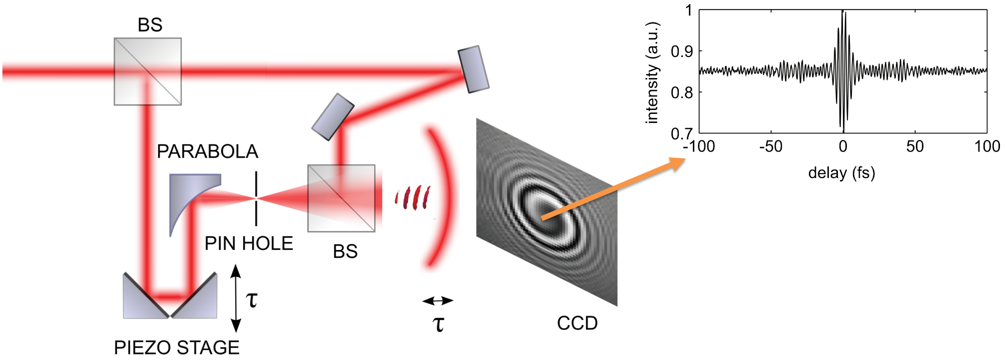

Figure 2.16: Spatio Temporal Characterization Setup. Schematic of the spatio-temporal measurement setup. The incoming beam is split into two parts, where one is used as a reference pulse and is focused with an off-axis parabola and can be delayed with respect to the pulse to be characterized by a piezo stage. An example of the spatial interference pattern as recorded by a camera is shown, as well as a sample lineout of the intensity at a pixel as a function of delay.

A technique developed simultaneously in Lund and Saclay [60, 61], has been used for these measurements. The technique combines holography and Fourier transform spectroscopy, by interfering the pulse to be measured with a reference beam and then varying the delay between the two. The principle is shown in Figure 2.16. The incoming pulse is split into two replicas. One of them is focused and spatially filtered with a pinhole, and the diverging spherical wave front provides a spatially homogeneous reference for the pulse to be measured. The reference and second delayed replica interfere at a CCD chip, and each pixel gives an interferogram. By assuming the center of the pulse is the same as the reference, the variation in spectrum and spectral phase over the pulse profile can be determined. For a complete characterization of the pulse, the spectral phase of the central part of the pulse used as reference also must be characterized, for example by the d-scan. This technique measures the field of the pulses in the far-field. The result can then be numerically propagated to e.g. the focus.

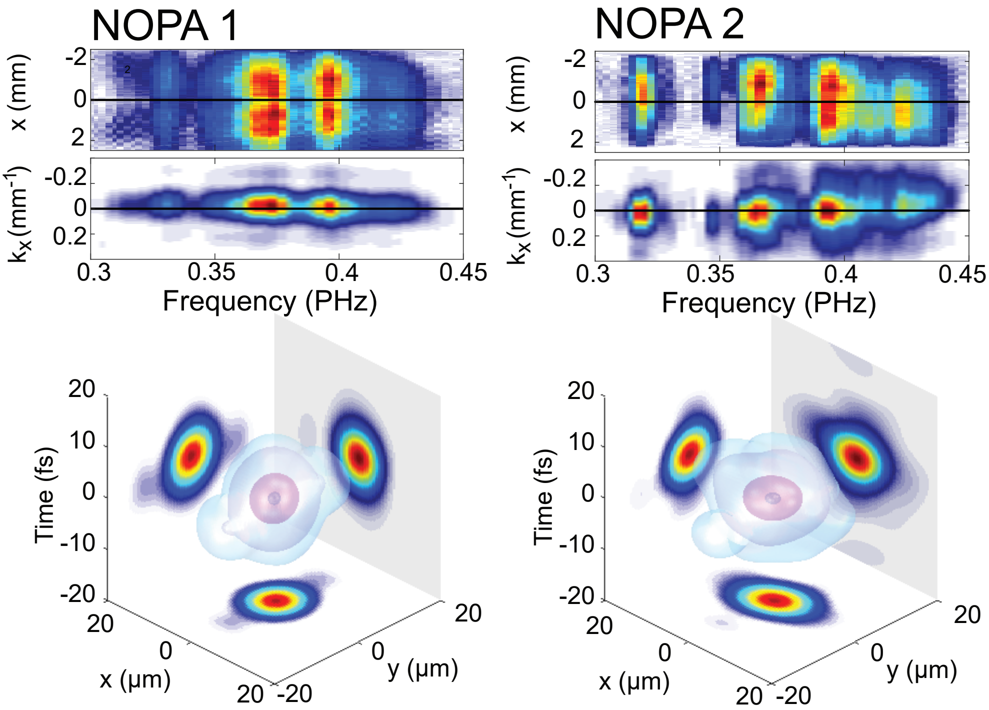

Figure 2.17: Spatio-Temporal Characterization. Measurements of the first NOPA stage are show to the left, and the second NOPA stage to the right. On top, the spectral content as a function of spatial position x and spatial frequency k_x va. ω is shown. On the bottom, 3D representations of the pulses after numerical propagation to the focus are plotted.

Figure 2.17 shows the result of such a spatio-temporal characterization of the output after both the first and second NOPA stages. Only the variation compared to the reference is shown, i.e. the center of the pulse is assumed to be Fourier-limited. This gives a better illustration of the spatio-temporal quality of the pulses and directly shows the focusability.

The spectral variation both in real and reciprocal space is shown, where reciprocal space represents the spatial frequency content and corresponds to angle of propagation. The variation in the x-direction is presented, representing the direction of the non-collinear angle in the NOPA, and therefore the direction in which spatio-temporal effects are expected. After the first stage, the spectral variation in both real and reciprocal space is minimal. Only a minor tilt can be seen in reciprocal space. After the second stage, some aberrations can be seen. In real space, it is clear that as one goes from lower to higher frequencies, the x-position changes, indicating spatial chirp. Also in reciprocal space we see a similar tilt at high frequencies, indicating some angular chirp.

The effect becomes obvious when the pulses are propagated numerically to the focus. After the first stage, no major distortions can be seen by eye in the y direction and along the time axis, and only some small additional structure is observed in the x-direction. After the second stage, however, the effects of the spatial and angular chirp are clearly visible as the pulse profile in the y-t plane has no longer a nice circular shape.

Determining the quality of the pules from these plots is not always easy, and one may also estimate the pulse quality quantitatively by using a three-dimensional Strehl ratio. This is a number between 0 and 1, obtained by comparing the maximum intensity of the measured pulse to the one obtained with a perfectly flat spatial phase, i.e. no spatio-temporal variation. For the first stage, this ratio is 0.81 and for the second 0.71. These values were obtained after careful alignments—in **Paper I** it is shown that a misaligned first stage easily leads to a Strehl ratio as low as 0.6. When the temporal distortions are also taken into account, i.e. when the spectral phase retrieved from the d-scan is applied, the Strehl ratio drops to 0.53 even in the case of optimized alignment. This illustrates the importance of minimizing the spatio-temporal couplings in a system like this.

The advanced pulse characterization tools presented in this section, i.e. pulse duration measurements (d-scan), CEP measurements, and assesment of spatio-temporal couplings and focusability, have been essential to ensure high-quality output pulses of the 200 kHz laser. This, in turn, is a key factor in being able to efficiently generate HHG, and the successful implementation of attosecond pump-probe measurements, as presented in Chapters 3 and 4.

Chapter 3

Generation of Attosecond Pulse Trains

In the late 80's, it was discovered that when an intense laser pulse is focused into an atomic gas, very high order harmonics of the impinging laser frequency can be generated [7, 8]. Unlike nonlinear interactions in crystals, where the second or third harmonics may be generated, these high-order harmonics do not decay in amplitude exponentially with increasing order, as would be expected by a perturbative process. Instead, they form a plateau with equal amplitude up until a certain cut-off, where the amplitude then rapidly drops, and only the odd-order harmonics of the fundamental driving frequency are observed.

It was quickly recognized that such spectral structure of peaks repeated at a certain interval could be the result of repeated temporal structure—i.e. a pulse train—and if the different harmonics were phase-locked and coherent, the total bandwidth of the harmonics would imply a long train of pulses with attosecond duration [62–64]. The first experimental verification of the temporal duration was obtained in the early 2000's [10, 65], finally providing proof that the HHG process results in coherent light pulses with a time duration that is still unprecedented. The current record for the shortest light pulse ever recorded is 43 attoseconds, produced though HHG using an OPA based light source with a central wavelength of 1.8μm [66]; however, pushing towards the shortest possible pulse is not necessarily the only way to obtain pulses that can be used for exciting experiments.

While the HHG process generally results in pulse trains, it is possible to isolate single attosecond pulses (SAP) [67], which can be well characterized [68, 69]. Long pulse trains are also often used in combination with the RABBIT technique which allows for the determination of the phase of the average pulse in such an attosecond pulse train (APT) [70].

This thesis work concerns the intermediate region, where the pulse train includes only a few pulses, with a more complex structure. Since the HHG process is sensitive to the electric field and not just the envelope, it is intuitive to understand that control of the CEP is important when generating with ultrashort pulses. It has been shown that when using few-cycle driving pulses the structure of the harmonic spectrum indeed is dependent on the CEP [71–73].

In this thesis, a simple model based on the three step model was used to model HHG driven by the laser presented in Chapter 2. This model provides insight into the structure of the attosecond pulse train and its spectrum, and how in the few-cycle regime this is influenced by the CEP. Due to the lower pulse energy of the laser compared to standard sources, tight focusing is required to reach the necessary intensities. Efficient HHG was achieved with a special gas target design. While the technical implementation is challenging, a combination of sophisticated engineering solutions and a thorough understanding of the physics of the process makes an efficient high-repetition rate attosecond light source possible.

In this chapter the process of HHG is explained, both its basics and the particularities that apply to the regime of few-cycle driving pulses. The impact of dispersion and CEP as covered in **Paper III** is discussed, and the specific engineering solutions used to ensure efficient HHG with very short, low energy pulses, as discussed in both **Paper I** and **IV**.

1 Theory of HHG

The process of HHG is highly non-linear and occurs when the magnitude of the impinging light field reaches the same order as the Coulomb potential that binds the electrons to the nucleus in an atom. The process can be well understood by a simple re-collision model developed already in the early nineties by Kulander et al. [74] and Corkum [75]. This semi-classical model divides the process into three distinct phases, and is therefore usually referred to as the three step model. Soon afterwards a fully quantum mechanical interpretation was also developed, commonly referred to as the Strong Field Approximation (SFA) [76]. While the SFA gives very good agreement with experiments, the simpler three step model provides physical insight and can be used to understand several important properties of HHG.

Figure 3.1 shows a representation of the three steps. In the first, the Coulomb potential (gray) is distorted by the potential of the impinging electric field (red). If the field is intense enough ($\sim 10^{14}$W/cm^2), the resulting distorted potential (black) creates a potential barrier which the electron can tunnel through. In the second step, starting when the electron has reached the continuum with zero kinetic energy, the electron is accelerated by the electric field—first away from the core, but as the oscillating electric field changes sign, it is driven back again. Depending on when the electron is born into the continuum, this classical motion can lead it all the way back to the nucleus, where it can potentially recombine

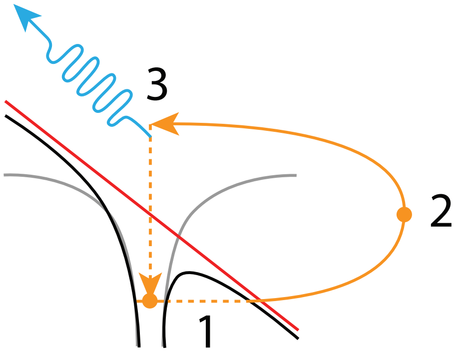

Figure 3.1: Illustration of the three step model. The electron is tunnel ionized in 1, is accelerated in the continuum in 2, and and recombines with the core in 3, resulting in the emission of light.

with the atom in the final third step. If it does so, its potential energy together with the energy it has gained through acceleration in the field is released as high energy photons, $E_{pot} + E_{kin} = I_p + 3.17U_p$. When using a driving laser in the near infrared, these high energy photons are in the XUV spectral regime.

1.1 Analysis of Classical Trajectories

While the tunnel ionization and recombination probabilities in this model are quantum mechanical, the electron trajectories can easily be derived by classical mechanics calculations. The electron is accelerated by the Coulomb force according to Newton's equation of motion:

$$\frac{d^2x}{dt^2} = -\frac{-e}{m_e}E(t) = \frac{e}{m_e}E_0 \sin\omega_0 t, \tag{3.1}$$

where e is the elementary charge, m_e the mass of the electron, E_0 the amplitude of the field, and w_0 the frequency of the field. Assuming the electron is born at an initial time t_i with zero momentum, integration yields the velocity and position:

$$\begin{aligned} v(t) &= \frac{eE_0}{m_e\omega_0}\left(\cos\omega_0 t - \cos\omega_0 t_i\right), \\ x(t) &= \frac{eE_0}{m_e\omega_0^2}\left(\sin\omega_0 t - \sin\omega_0 t_i - (\omega_0 t - \omega_0 t_i)\cos(\omega_0 t_i)\right). \end{aligned} \tag{3.2}$$

The trajectories described by these equations are plotted in Figure 3.2 for one half cycle of the driving field, marked in red. If the electron never returns to the core, i.e. $x(t > 0) \neq 0$, the trajectory is plotted in gray. If it does, the color of the trajectory is proportional to the return energy, where blue is the highest energy and red is the lowest. It is clear that far from all trajectories return to the core; such a return is only possible during a duration of a quarter cycle after the magnitude of the electric field strength peaks. It can also be observed that different trajectories can lead to the same kinetic energy at return. These can be separated into long trajectories, where the electron is ionized early after the peak of the half cycle and return late after a large excursion, and short trajectories, where the electron is ionized close to the end of the half cycle and return quickly.

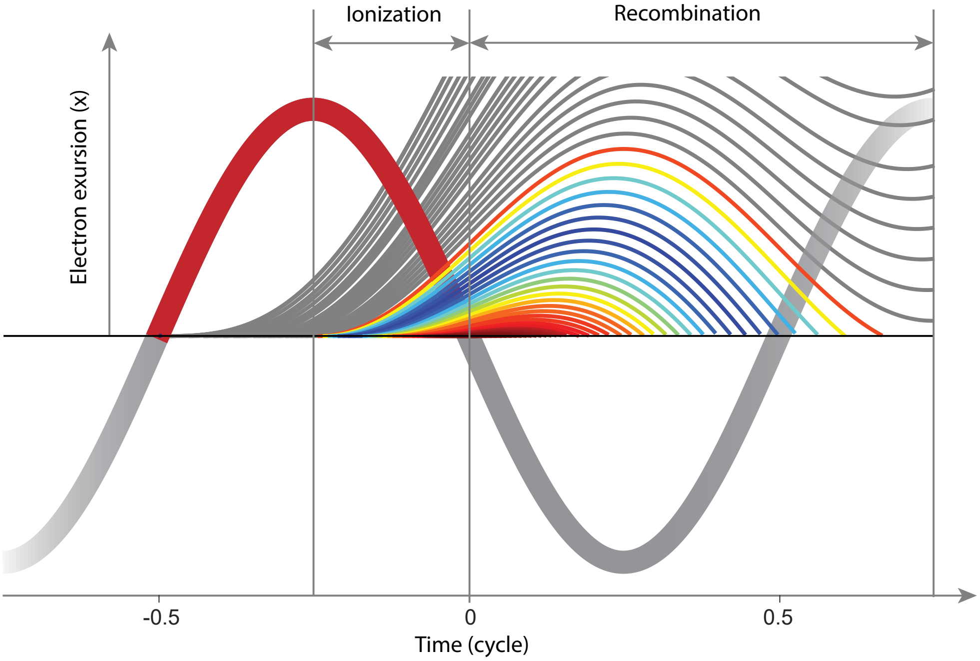

Figure 3.2: Classical electron trajectories. The electron trajectories during one half-cycle of the driving field, marked in red. Trajectories that do not return to the core are marked in grey. Trajectories that do return to the core colored reflecting the amount of kinetic energy the electron carries at return, from red (low energies) to blue (high energies).

The electron can recombine with the core $x(t_r) = 0$, where t_r is the time of return. Solving that equation analytically is hard, but numerically straightforward. As can be seen in Figure 3.2, the electron returns if it has been ionized during the second half of the half-cycle of the driving field, i.e. after the peak, and the maximum possible photon energy after recombination is found to be

$$E_c = I_p + 3.17U_p, \tag{3.3}$$

where I_p is the ionization potential of the atom and $U_p = E_0^2 e^2/4m_e\omega^2$ is the ponderomotive potential; the average kinetic energy of an electron in an oscillating electric field with frequency ω. E_c is called the cut-off energy.

The HHG process repeats itself every half cycle of the driving field, and the spectrum with odd-order harmonics can be simply understood as a result of the interference of the coherent pulse train; since the separation between pulses is half the driving IR field period $T = T_{IR}/2$, the separation between the resulting interference fringes in the spectral domain will be $\Delta\Omega = \Omega_{rep} = 2\pi/T = 2 \cdot 2\pi/T_0 = 2\omega_0$. The flipping sign of the IR half cycles results in a π phase shift between consecutive pulses, which can be interpreted as a CEO as introduced Section 1.3. With $\phi_{CEO} = \pi$ the frequency comb is shifted by $\phi_{CEO}/2\pi\Delta\Omega = \omega_0$, i.e. the result is only odd harmonics.

If the electron can recombine, it carries at this time t_r a kinetic energy $m_e v(t_r)^2/2$, which along with the potential energy is released as a photon. Thus by finding the possible return times t_r and corresponding energies, it is possible to find the instantaneous released photon energy and how it evolves over time; i.e. the three-step model provides a detailed description of the temporal structure of the generated XUV pulses for each half cycle.

1.2 Modelling Pulse Trains

Plotting the return energy as a function of first ionization time ($t < 0$) and then return time ($t > 0$) gives Figure 3.3. Again, the long and short trajectories can be clearly identified, marked by yellow and purple, respectively. Since the electron instantly releases its energy at recombination, the total energy versus return time relation for the electron is identical to the instantaneous frequency versus time relation for the attosecond pulses—in other words, the recombination curve of Figure 3.3 corresponds to the frequency dependent GD of the generated attosecond pulse.

Separating long and short trajectories, these curves can be approximated by a linear function with the a slope equal to the tangent at $(\Omega_c - \Omega_p)/2$, plotted in Figure 3.3 in black, where Ω_c is the cut-off energy and Ω_p is the ionization potential. This linear approximation crosses Ω_p at a time t_{pi}, and it intersects with Ω_c at a time t_{ci}, where the subscript $i = s, l$ refers to the short or long trajectory. These times can be shown to be intensity-independent and their value can be extracted numerically. For the short trajectory they are $t_{ps} = 0.1784T_0$ and $t_{cs} = 0.401T_0$, where T_0 is the carrier period.

Using the linear approximation, we can write the GD of the resulting attosecond pulse as

$$GD(\Omega) = t_{pi} + \frac{t_{ci} - t_{pi}}{\Omega_c - \Omega_p}(\Omega - \Omega_p) \tag{3.4}$$

where $\Omega_p = I_p/\hbar$ is the ionization potential and $\Omega_c = (3.17U_p + I_p)/\hbar$ is the cut-off

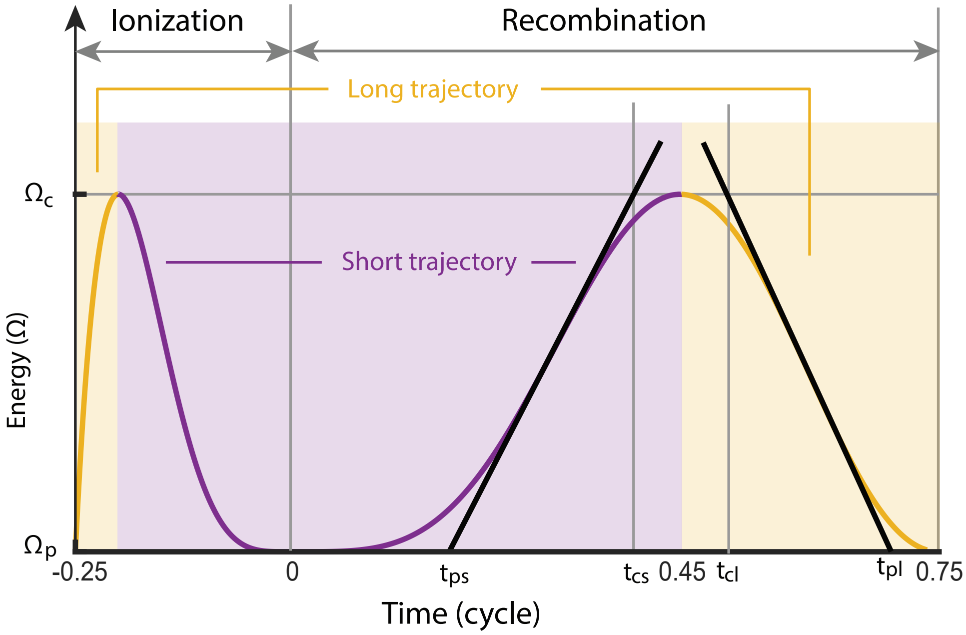

Figure 3.3: Return energies. Return energy of the electron as a function of ionization time and return time, separated into long (yellow) and short (purple) trajectories. A linear approximation of the time dependence of the return energy in shown in black, for both long and short trajectories.

energy. Integration now yields the spectral phase:

$$\phi(\Omega) = \phi_i(\Omega_p) + t_{pi}(\Omega - \Omega_p) + \frac{t_{ci} - t_{pi}}{2(\Omega_c - \Omega_p)}(\Omega - \Omega_p)^2. \tag{3.5}$$

where $\phi_s(\Omega_p) = 0$ for the short trajectory and $\phi_l(\Omega_p) = \alpha_l I$, for the long. The second term is linear and thus places the pulse in time in relation to the driving field. The last term gives the chirp of the pulse. An important observation is that $\Omega_c - \Omega_p = 3.17U_p \propto I$, and with a proportionality constant γ we can write

$$\phi(\Omega) = \phi_i(\Omega_p) + t_{pi}(\Omega - \Omega_p) + \frac{\gamma}{I}(\Omega - \Omega_p)^2. \tag{3.6}$$

Traditionally, the phase imprinted on the attosecond pulses from the HHG process is called the dipole phase, and is approximated by the simple relation $\phi(\Omega) = \alpha_j I$, where the index j indicates the harmonic order [70, 77, 78]. The dipole phase also differs between the long and short trajectory. While Equation 3.6 is more complex, we can attempt to recover α (for the short trajectories) by taking its derivative with respect to intensity:

$$\alpha = \frac{\partial \varphi}{\partial I} = \frac{\gamma}{I^2}(\Omega - \Omega_p)^2. \tag{3.7}$$

In the case where $(\Omega - \Omega_p) \propto I$, α would become intensity independent and the simpler relation for the dipole phase would hold. This is true in the middle of the plateau region where $\Omega = (\Omega_c + \Omega_p)/2$, since $(\Omega - \Omega_p) = (\Omega_c + \Omega_p)/2 - \Omega_p = (\Omega_c - \Omega_p)/2 \propto I$.

This model describes the spectral phase of the XUV generated from a single half cycle. The spectral amplitude also needs to be determined in order to be able to calculate an attosecond pulse and apply this to the modeling of pulse trains. The spectral amplitude of a single pulse, $\tilde{E}(\Omega)$, is initially assumed to span from the ionization threshold to the cut-off and have a super-Gaussian shape. The spectral intensity is then weighed according to the photoionization cross section for the chosen generation gas [79]. Finally, the integrated power spectrum, i.e. the energy of the XUV pulse, is assumed to vary with pulse intensity as the ionization rate, which is calculated according to the Ammosov-Delone-Krainov approximation [80].

With both the spectral amplitude and phase, and knowing that the process repeats every half cycle of the driving field, this may now be used to calculate pulse trains from any given driver. Since the dipole phase is strongly intensity dependent, the spatio-temporal couplings of the harmonic beam due to the intensity variation across the transverse focus at generation can also be modelled, as shown in [81].

1.2.1 Multiple Pulse Interference

The individual pulses, with an amplitude and phase according to the model and an additional π phase shift between consecutive pulses, can be coherently added in the spectral domain:

$$\tilde{E}(\Omega) = \sum_m \tilde{E}_m(\Omega) e^{i(m\pi + t_m\Omega + \phi(\Omega))}, \tag{3.8}$$

where $m\pi$ gives the phase flip, t_m is the starting time of half-cycle m, marked as 0 in Figure 3.3, and $\phi(\Omega)$ is the dipole phase given by equation 3.6 and delays the pulse further as well as adds chirp. The values of t_m can easily be found by identifying the zero-crossings of the driving waveform. In the case of a simple Gaussian driving pulse with only second order dispersion, t_m and the corresponding instantaneous intensity I can be found analytically, as derived in **Paper III**. For more complicated pulses that cannot be well approximated to a Gaussian, for example one experimentally obtained pulses by the d-scan technique, t_m and I can be found numerically. These parameters can then be used as input to the model which in a straightforward way returns the APT for an arbitrary input pulse.

Since the spectral phase depends on the intensity, a variation of the spectral phase of the pulses in the train is expected, corresponding to the variation of the intensity of the half-cycles of the driving field. For a hypothetical single-frequency driving field, with continuous intensity, all pulses would be identical (apart from the intrinsic π phase flip between consecutive pulses).

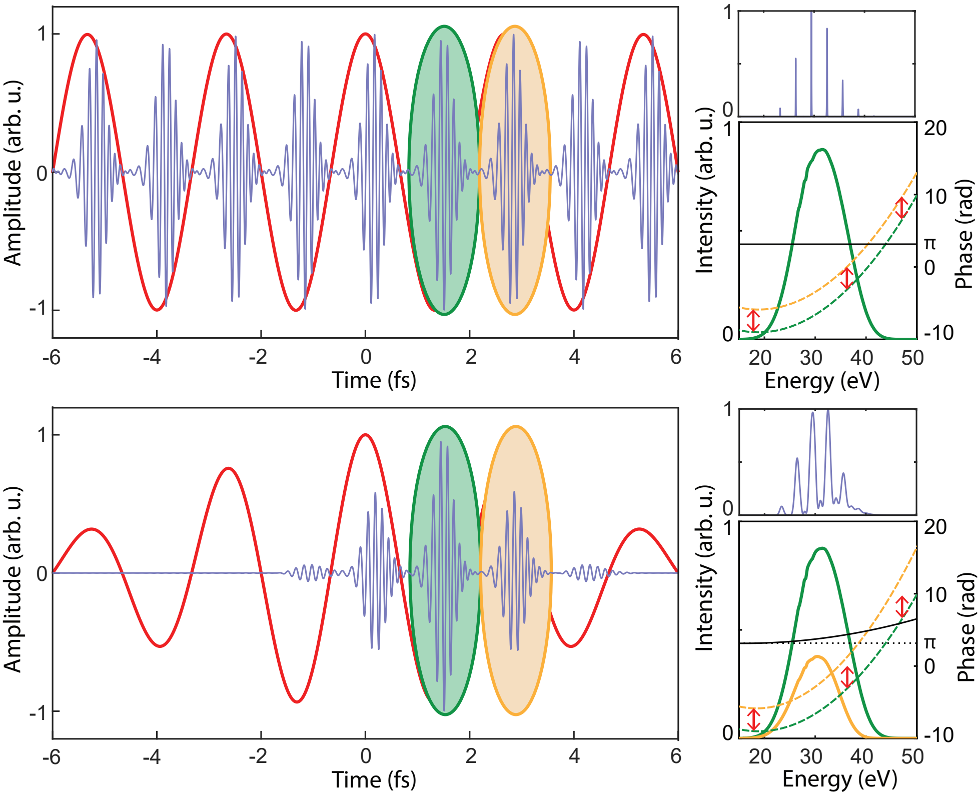

Figure 3.4: Differences between consecutive pulses. Top row: APT from a 100 fs IR pulse. Bottom row: APT from a 5.8 fs IR pulse. The driving field and XUV pulses are shown to the left. To the right, the total XUV spectrum (top) and spectrum and spectral phase of the individual pulses marked with yellow and green, respectively. The phase difference between the pulses is plotted in black. The red arrows are all the same length and emphasize the increasing phase difference in the short pulse case.

Figure 3.4 shows the difference between consecutive pulses in the train for both a long and a short driving field, calculated according to the multiple pulse interference model. In the top row, the pulse train, total spectrum, and difference between two adjacent pulses are shown for a 100 fs driving pulse. As evident by the bottom right plot in the top row, the two consecutive pulses generated by the center of the driving pulse have an identical spectrum and a constant spectral phase difference of π (black line). Note that all red arrows are the same length. In the bottom row, the same is shown for an APT generated by a 5.8 fs pulse with the same carrier frequency. The harmonics are now much broader, and some sub-maxima can be observed.

Again, one can use the analogy of diffraction, with the pulses in time as the slits. The long pulse train has enough pulses/slits that the diffraction/harmonic peaks are very narrow. In the bottom of Figure 3.4, it is clear that the short pulse has instead generated only three dominant pulses. A diffraction pattern from three slits is expected to have one sub-maximum—as is also observed. It is immediately obvious, however, in the time domain that consecutive pulses are no longer identical, due to the varying spectral phase. The bottom right plot shows the obvious difference in spectral amplitude, but also how the phase difference now varies across the spectrum, and can no longer be considered to be just π.

1.2.2 Temporal Characteristics of APTs from Few-Cycle Pulses

When using a standard 20 fs driving pulse it is a fair assumption to say that the pulses in the train are very similar, however, this is no longer true approaching the few cycle regime; see Figure 3.4. The overall temporal structure of the pulse train also varies significantly with CEP.

This fact has been used as an effective gating mechanism to produce single attosecond pulses [67, 82]. For a near single cycle driving pulse with CEP = 0, there is a single half-cycle which has a significantly larger amplitude than the rest of the pulse—consequently, this half-cycle produces an XUV pulse with significantly higher energies. By locking the CEP and filtering the high energy range, a single attosecond pulse remains [67]. However, this is done at the expense of essentially throwing away a significant amount of XUV energy, and to do it well, additional gating techniques are often required to further suppress harmonic generation from the weaker half-cycles [83]. When the available energy is already in short supply, it would be advantageous to use all generated XUV. While isolated attosecond pulses certainly provide a more straightforward conceptual picture when used for experiments, with a proper understanding of the structure of a short pulse train and how it may be manipulated, it may even provide certain advantages.

In Figure 3.5, pulse trains generated by a typical pulse from the 200 kHz laser system at LLC are shown for two different CEPs, CEP=0 and CEP=π. When the intensity, i.e. the envelope of the attosecond pulses is plotted, it is obvious how the fundamental structure of the train changes from two to three pulses. By looking closely at the two-pulse case, we also see that the two pulses are, in fact, in this case very similar (apart from the π phase flip)—due to the fact that they are generated by equally strong half-cycles.

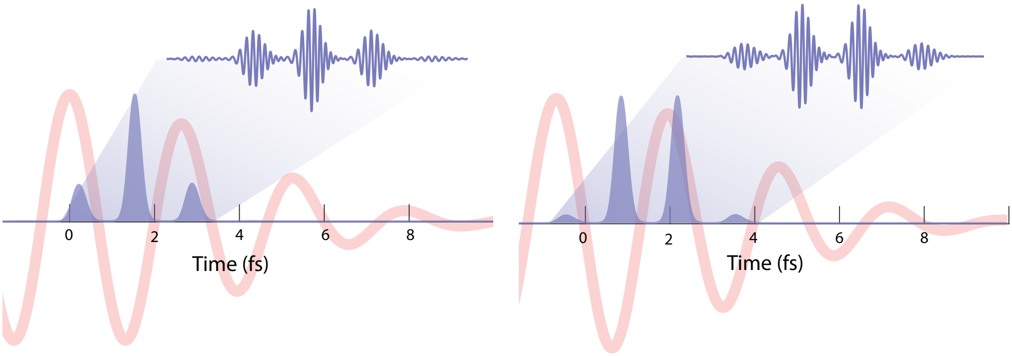

Figure 3.5: CEP dependance of short pulse train in the temporal domain. To the left, three XUV pulses generated by a driving field with CEP = 0. To the right, two XUV pulses generated by a driving field with CEP = $\pi/2$.

Knowing the amount of pulses in the train is important since it allows for certain approximations when describing photoionization, as utilized in **Papers IV** and **VI** and discussed in Chapter 4.

1.3 Phase Matching

As with the more common non-linear processes that were presented in Chapter 2, high harmonic generation must be phase matched in order to result in a significant build-up of XUV radiation. Simply put, the XUV emitted by atoms in the first part of the gas medium must oscillate in phase with emitters in the later part of the medium, and any phase mismatch will lead to destructive interference and reduced efficiency of the process. This phase mismatch can, in general, be expressed as

$$\Delta\mathbf{k}(q) = q\mathbf{k} - \mathbf{k}_q \tag{3.9}$$

for an harmonic with frequency $q\omega_0$. We can split the phase mismatch contributions into four components:

$$\Delta\mathbf{k} = \Delta\mathbf{k}_g + \Delta\mathbf{k}_d + \Delta\mathbf{k}_n + \Delta\mathbf{k}_p, \tag{3.10}$$

where $\Delta\mathbf{k}_g$ is the mismatch due to the Gouy phase, $\Delta\mathbf{k}_d$ is the mismatch due to the dipole phase, $\Delta\mathbf{k}_n$ is the mismatch due to dispersion in the neutral gas, and $\Delta\mathbf{k}_p$ is the mismatch due to the generated plasma [84, 85]. These phase matching parameters are defined experimentally by the field intensity, the focusing geometry and position, and the length and density of the generation gas. A formal discussion on phase matching can be found in [86].

In practice the focusing geometry is determined by the available pulse energy of the laser system. The pulses must be focused tightly enough that sufficient intensities for HHG can be reached; however, a too high intensity will ionize large parts of the medium, resulting in large values of Δk_p that cannot be balanced. The lighter noble gases generally have lower ionization rates which allows for higher intensities, and therefore also higher photon energies. This, however, comes at the expense of a lower conversion efficiency, mostly attributed to a lower recombination probability.

The chosen focusing geometry determines the Gouy phase, which is the phase difference between the on-axis phase fronts of a focused Gaussian beam and a plane wave. For the harmonics, this phase can usually be neglected, and only the driving field contribution is considered. The derivative of this phase gives the phase mismatch term Δk_g, and it is always negative:

$$\Delta k_g = q\frac{d\zeta}{dz} = -\frac{qz_R}{z^2 + z_R^2} \xrightarrow[\frac{z}{z_R}\to 0]{} -\frac{q}{z_R}. \tag{3.11}$$

The phase mismatch due to the dipole phase can be expressed as

$$\Delta k_d = \frac{\partial \phi(\Omega)}{\partial z}. \tag{3.12}$$

Since the dipole phase is, as shown earlier, strongly dependent on the intensity, which varies along z across the focus, we get a strong variation of this phase matching term, including a switch of sign: it is positive before the focus and negative after. Since the dipole phase also has a different sign for the long and short trajectory, and in general is larger for the long trajectory, this also means that phase matching both trajectories simultaneously is not possible. In practice, the aim is usually to phase match the short trajectory.

The mismatch due to the neutral gas and plasma both scale linearly with gas density: $\Delta k_n = \rho \Delta\kappa_n$ and $\Delta k_p = \rho\eta_p\Delta\kappa_p$ [87]. They also have opposite sign; $\Delta k_n > 0$ and $\Delta k_p < 0$. With the right gas density, the four terms can be transiently balanced. At the laser focus, $\partial I/\partial z \approx 0$, and the contribution of the dipole phase can be neglected. Then the gas density that results in phase matched generation is given by [87]:

$$\rho = -\frac{\Delta k_g}{\Delta\kappa_n + \eta_p\Delta\kappa_p} = \frac{q}{z_R(\Delta\kappa_n + \eta_p\Delta\kappa_p)}. \tag{3.13}$$

Since the gas density is inversely proportional to the Rayleigh length of the focusing geometry, this means that for efficient HHG tightly focused beams require a high gas density, and vice versa.

Even with good phase matching the length of the gas target must be limited properly to prevent re-absorption of the XUV. The degree of absorption depends on the gas density, where a higher density leads to higher absorption. This means that a HHG gas target with a high pressure must also be short. Beamlines for HHG designed for low energy pulses thus tends to be very compact, while for systems with large energies the focusing geometries can stretch over tens of meters.

While the compactness of low pulse energy HHG setups gives them a small footprint suitable for regular research labs, they also present a set of engineering challenges. Designing a gas target with a high localized gas density in an otherwise high vacuum environment is not trivial, and the solution implemented for the high repetition rate system used in this thesis is presented further in Section 2.1.

2 Experimental Implementation

2.1 Gas Target Design

In order to achieve optimal phase matching conditions and generate harmonics efficiently, a special gas target has been designed for the beamline. The design is described in **Paper I**, and more recently simulations were performed to determine the best conditions for the gas target, as described in **Paper IV**.

As presented in **Paper IV**, calculations show that generation in argon with a pulse energy of 15 μJ at 850 nm, focused with an f-number of approximately 8, requires a gas target density of 8.9 kg/m^3 (corresponding to a pressure of $\sim$5 bar), and a medium length of 40 μm. This poses a significant engineering challenge. Due to the high repetition rate, the gas flow cannot easily be pulsed, and thus a continuous mass flow rate of 4×10^{-3}g/s will be injected into the vacuum while the ambient pressure must be kept low to prevent re-absorption of the generated XUV. It is most efficient to catch the ejected gas before it has diffused too much. To solve this issue, a gas catcher design has been implemented, as presented in **Paper I**. The design is shown in Figure 3.6.

Simulations using the compressible flow solver within the STARCCM+ program package were performed to confirm that the design can achieve high localized gas pressure without contaminating the surrounding vacuum. The results are shown on the right of Figure 3.6. The 2D density map shows how the 43 μm nozzle opening, backed by 12 bar of argon, ejects the gas so that the catcher, situated at a distance of <200 μm, catches almost all of the gas. Note that the horizontal axis of the 2D map only covers a range of 180 μm, while the actual catcher opening is 1 mm. The simulations indicate that such an opening can catch >90% of the gas injected into the chamber. This has also been confirmed by comparing the pressure in the surrounding chamber when the catcher is on or off.

The rightmost graph in Figure 3.6 shows the gas density variation along the gas flow direc-

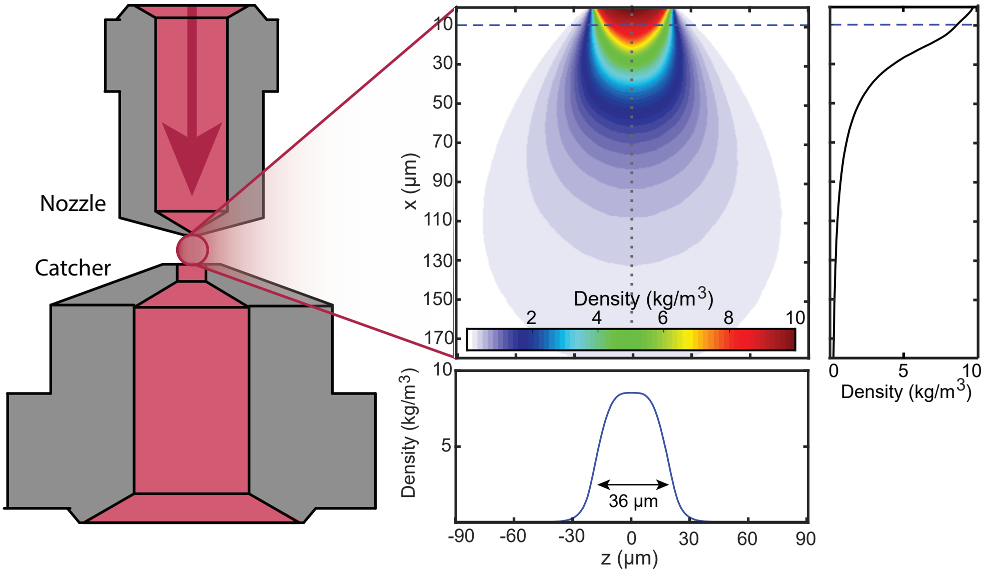

Figure 3.6: Gas target. Left: an illustration of the nozzle-catcher setup. Right: gas density simulation results, consisting of a 2D density map (top left), a line-out along the dotted grey line where z=0 (top right), and a line-out along the dashed blue line where x = 10μm (bottom).

tion, with a sharp drop quickly after the nozzle exit. The dashed blue line in this line-out and in the 2D map indicates a position 10 μm away from the exit, where the focused generation laser beam traverses the gas target. At this position, the maximum gas density is 8.5 kg/m^3. The bottom line out shows the gas density variation along this dashed line, perpendicular to the gas flow. The FWHM of this gas density profile is 36 μm, and it has roughly a super-Gaussian shape. In summary, the simulations show that this gas target design comes very close to the calculated ideal phase matching conditions of a medium length of 40 μm and gas density of 8.9 kg/m^3, while avoiding contamination of the surrounding vacuum almost entirely.

Finally, the simulation results were confirmed by using the pump-probe interferometer to measure the temporal delay introduced by the beam passing through the gas target. With the help of the HeNe used for active stabilization of the interferometer a delay of 0.65 rad was measured between moving the gas target in and out of the beam, while ensuring the beam path was as close as possible to the nozzle exit. The corresponding calculated phase shift from the data presented in Figure 3.6, using refractive index data for argon [88], is 0.625 rad—again, closely matching the measured 0.65 rad.

2.2 XUV-IR interferometer

During the thesis work the experimental setup for the HHG has been redesigned and an XUV-IR interferometer has been installed. Figure 3.7 shows the footprint of the vacuum chamber and the beam path of interferometer. The interferometer design is presented in detail in **Paper IV**.

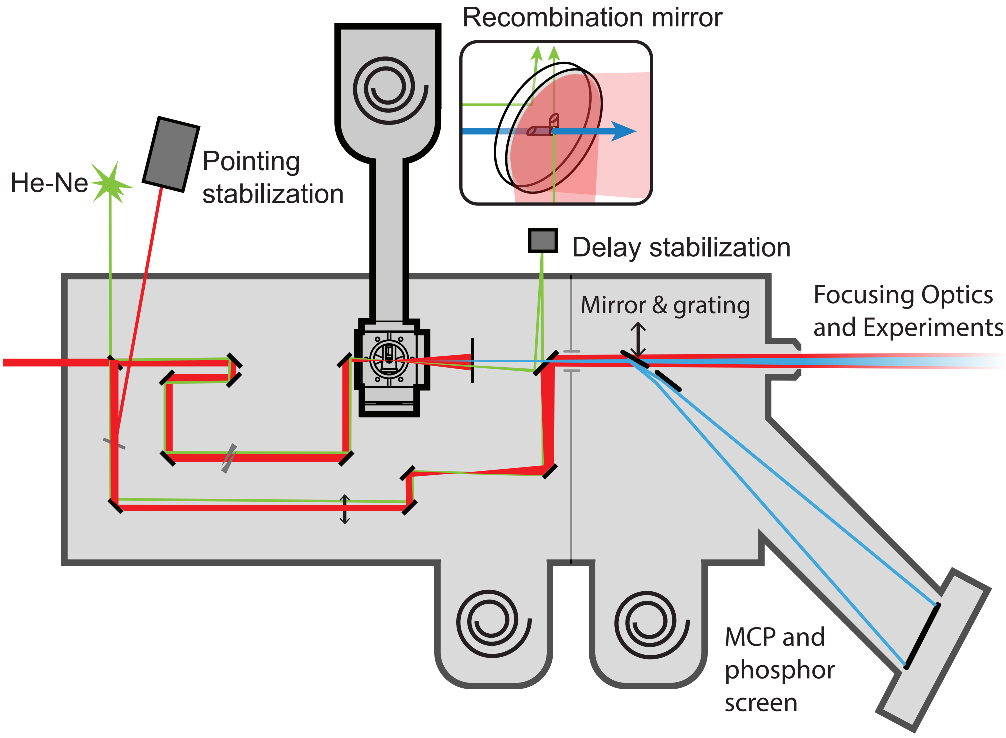

Figure 3.7: XUV-IR interferometer. The IR beam enters from the left. The beam paths for the pump and probe are shown, along with the XUV spectrometer. The recombination mirror is shown in an insert.

The IR beam, red, enters the vacuum chamber from the left and a beamsplitter divides it into two paths. 80% is transmitted to the pump arm. After a piezo controlled retroreflector and a pair of glass wedges for dispersion control, the XUV is generated by focusing into the HHG gas target using an off-axis parabola with a focal length of $f = 5$ cm. The remaining IR is removed by a metallic filter, leaving only the XUV attosecond pulse train. The probe arm consists of the remaining 20% of IR which is reflected by the beamsplitter. In this arm, a 1 mm AR coated glass plate is used to split off a small fraction of the probe for pointing stabilization. A fused silica lens is placed to introduce a focus at the same relative distance as the focus in the pump arm.

The probe is recombined with the pump arm via the use of a recombination holey mirror. The XUV beam from the pump arm has a smaller divergence and is transmitted through the small hole, while the rest of the mirror surface still reflects the majority of the probe beam. The recombined XUV pump and IR probe are then sent to a toroidal mirror which focuses them for experiments. The toroidal is designed to operate in 2f:2f condition, re-imaging the XUV generation focus one-to-one in the application interaction region. The focus introduced in the probe arm ensures that the XUV and IR focii are overlapped longitudinally. The focal length of the lens in the probe arm is chosen to match its size to the recombination and toroidal mirror. This ensures a high IR intensity in the experiment.

A flat gold mirror may be inserted into the beam, guiding the light to a flat-field XUV spectrometer consisting of a grating and an MCP detector and phosphor screen. The concave aberration-corrected grating (Hitachi, 001-0640, 1200 groves/mm), refocuses the diverging XUV onto the detector for good spectral resolution. The phosphor screen is then imaged by a camera to record the spectrum.

The time delay between the two arms is controlled by the retroreflector, placed on a piezo controlled translation stage in the pump beam. In order to successfully perform pump-probe experiments, the time delay must be controllable with a precision of fractions of an IR cycle time duration—i.e. attoseconds. While the piezo stage itself is precise enough, all additional causes of timing jitter between the two arms should be minimized. In order to optimize passive interferometer stability, the breadboard for all optical components is vibrationally decoupled from the surrounding vacuum chamber. An improvement by a factor of two in passive stability is achieved when the chamber and breadboard are properly decoupled, compared to when the breadboard and vacuum chamber are in contact, and a final RMS error of 23 as can be achieved as shown in **Paper III**.

Other sources of drift such as e.g. thermal expansion can be continuously compensated for by active stabilization using a helium-neon (HeNe) laser, coupled into the beam path through the beam splitter, shown in green in Figure 3.7. With the holey mirror and a metallic filter, a spatial interference pattern can be recorded and used for active stabilization of the delay. The filter is made so that the metallic film is suspended on a transparent medium, which then blocks the IR in the center of the beam but lets the surrounding IR and HeNe beam through. The holey mirror, shown in the insert in Figure 3.7, has a polished backside which reflects the HeNe out of the chamber. It also has an extra drilled hole for the HeNe beam that has gone through the probe arm. The spatial interference of these two beams outside the chamber then encodes the time delay.

An additional notable design choice is the small secondary cube within the main vacuum chamber, where the HHG gas target is placed. The laser enters and exits the cube through differential pumping holes placed at a few millimeters to the gas target, and the interior of the cube is pumped by an additional turbo pump marked at the top of the figure. The gas target inside is mounted on a 3D translation stage controllable from outside the vacuum chamber, so that it can be moved relative to the laser focus.

2.3 Experiment—HHG dispersion scans

In **Paper III**, the multiple interference model is used to interpret experiments where the harmonic spectrum is measured as a function of dispersion in the form of glass insertion by the same BK7 wedges as used for the d-scan measurement. Figure 3.8 shows, to the left, the result of such a measurement when generating in argon, and to the right, a calculation done by the numerical multiple pulse interference model.

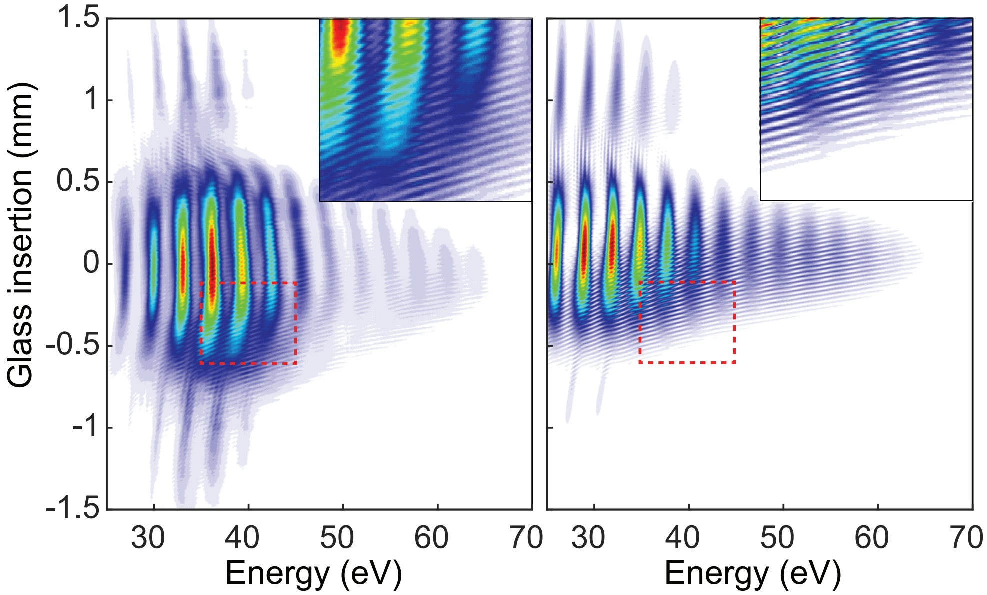

Figure 3.8: HHG dispersion scan in argon. Measured (left) and calculated (right) spectograms. The inserts show a magnification of the same region for both measurement and simulation, marked with dashed red lines.

In both the measurement and the calculation the spectogram has ”wings” for small and large glass insertions. These result from the complicated spectrum and complicated spectral phase of the driving pulses, which, for some amounts of GDD, briefly becomes more compressed again. The width of the harmonics changes across the scan, and they are maximally compressed at different glass insertions; this is discussed in detail in **Paper III**. Finally, distinct fringes can be observed all across the spectogram in both the measurement and the calculation. The slope of these fringes changes along the glass insertion axis, and when the pulse is well compressed, follow the changing CEP. For lower energies, the harmonic structure is strong, imposed by the interference between multiple pulses. At the higher energies that are only generated by the central strong half-cycles of the driving pulse, and where the number of pulses depend strongly on the CEP, the fringes are more dominant.

The same measurement can be performed for generation in other gases; Figure 3.9 shows an HHG dispersion scan in neon with a zirconium filter, resulting in much higher photon energies than in Figure 3.8. In this measurement the harmonic structure is entirely lost and only diagonal fringes can be seen. The filtering of higher energies also implicitly leads to the filtering of the cut-off region, which is only generated by the strongest half cycles of the driver. In this case, interference from only these corresponding attosecond pulses can be seen. Indeed, the continuous shift of the position of the harmonic peaks while their spacing remains the same, agrees with generation of only two pulses. A continuous shift of interference peaks is what happens in the interference between two slits, when the phase difference between the two is varied. Imposing a fixed odd harmonic structure would require at least a third slit—or in this case, pulse.

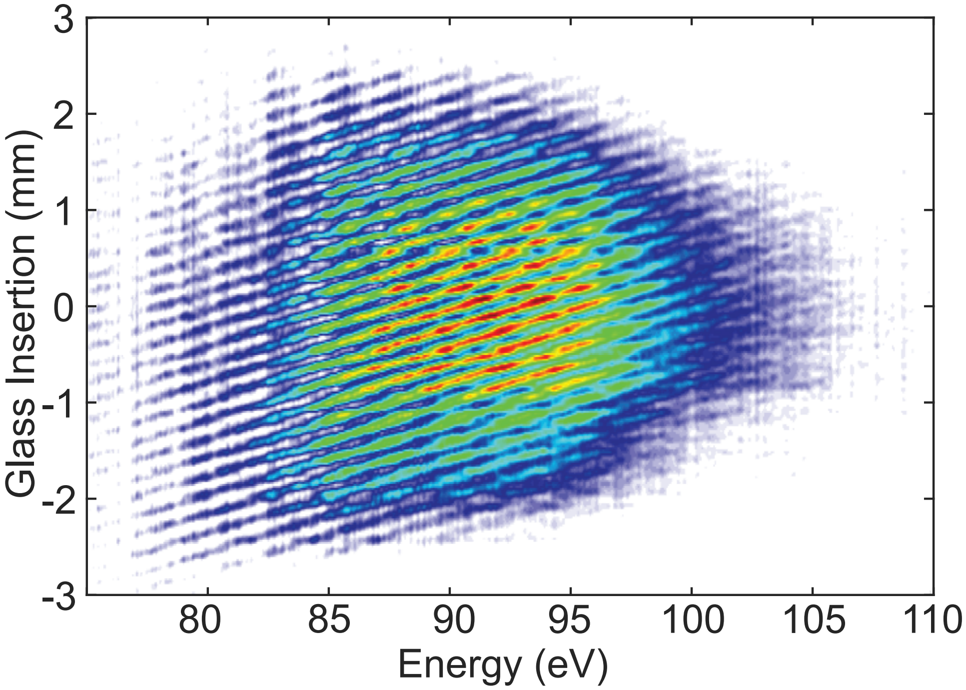

Figure 3.9: HHG dispersion scan in neon. HHG spectrum from neon as a function of glass insertion.

Chapter 4

Photoionization

When a photon with sufficient energy interacts with an atom, an electron may be ejected in a process referred to as photoionization [89, 90]. The photoelectron, leaving the parent ion, will have an energy equal to that of the photon minus the ionization potential of the bound electron. In the XUV range—i.e. for the light produced by most HHG sources—this energy condition is easily reached, and XUV light is in general strongly absorbed by matter.

Most traditional spectroscopy methods, such as those used at synchrotron XUV sources for decades, rely on measuring the spectrum of the photoelectrons. While investigations into the structure of matter at these facilities have proven to be enormously successful, measuring only the spectrum of the photoelectron introduces the same problem as in the optical domain—i.e. all phase information is lost. Electrons, in fact, have wave properties in the same way as light, which has been observed since the early 1900s [91]. The properties of photoelectrons are in fact strongly dependent on the properties of the ionizing light field—i.e. in the present case the high harmonics. In the case of photoionization by attosecond pulse trains, the possible interference between ionized electrons makes it more useful to talk about electron wave packets (EWP) instead of electrons as particles.

The field of attosecond science has traditionally studied photoionization and the properties and interference of EWPs. The following chapter explores how this may be done in the few-cycle regime. The chapter begins with a presentation of the spectrometer used to measure photoelectron kinetic energy, then, photoionization by combined XUV-IR fields is discussed. It is shown how this differs from traditional methods used in attosecond science in the few-cycle regime. Finally, a first step towards applying the time resolution promised by attosecond pulses to highly correlated systems is presented. The experiment on single-photon double ionization, the process of a very energetic photon knocking out two electrons at once, is shown.

1 3D Momentum Spectrometer—The CIEL

Many different types of spectrometers can be used for photoelectron spectroscopy, but most of these are based on the time-of-flight (TOF) principle—particles with different kinetic energy will hit a distant detector at different times. When detecting charged particles, electric and magnetic fields can also be used to guide the particles to eventually image the momentum distribution in the interaction region. In attosecond science, a standard device is the Magnetic Bottle Electron Spectrometer (MBES). With such a spectrometer, a strong magnetic field is used to re-direct electrons in up to a 4π solid angle collection efficiency, before they are guided into a flight tube and then to a detector [92, 93]. Also commonly used is the Velocity Map Imaging (VMI) spectrometer, which uses electric fields to create a 2D projection of the 3D momentum distribution of the photoelectrons on a detector [94]. A VMI spectrometer can also be designed so that both electrons and ions can be detected simultaneously, and possibly in coincidence [95].

In order to perform so called kinematically complete experiments, however, where the momentum of all fragments after interaction is measured, more advanced spectrometers have been developed. These are called 3D momentum imaging instruments, and the most common type is called a REaction MIcroscope (REMI) [96]. Combined with a gas target cooled by supersonic expansion, the resulting technique is called Cold Target Recoil Ion Momentum Spectroscopy (COLTRIMS) [97]. These instruments are specifically suited to measure ions and electrons in coincidence, which allows for a complete characterization of a photoionization event. In order to statistically ensure that the measured charged particles come from the same event, the event-rate must not exceed a tenth of the total repetition rate of the measurement—this means that their powerful imaging capabilities are best exploited in combination with a high repetition rate light source.

In this thesis work, a 3D momentum spectrometer based on the "Coïncidences entre Ions et Electrons Localisés" (CIEL) principle [98–100] has been used for the photoelectron spectroscopy experiments from **Paper IV** and **VI**. The design is presented in further detail in [101]. A sketch of the working principle of the spectrometer can be seen in Figure 4.1, along with the coordinate system used to represent any 3D data in this thesis, either from real measurements or simulations. The polarization of the light is along the z-axis, the light propagates along the x-axis, and in this illustration the spectrometer axis is along the y-axis. The azimutal angle φ, ranging from $-\pi$ to π, is that of the momentum projection in the x-y plane, while the elevation angle θ, ranging from 0 to π, refers to the angle relative to the z axis.

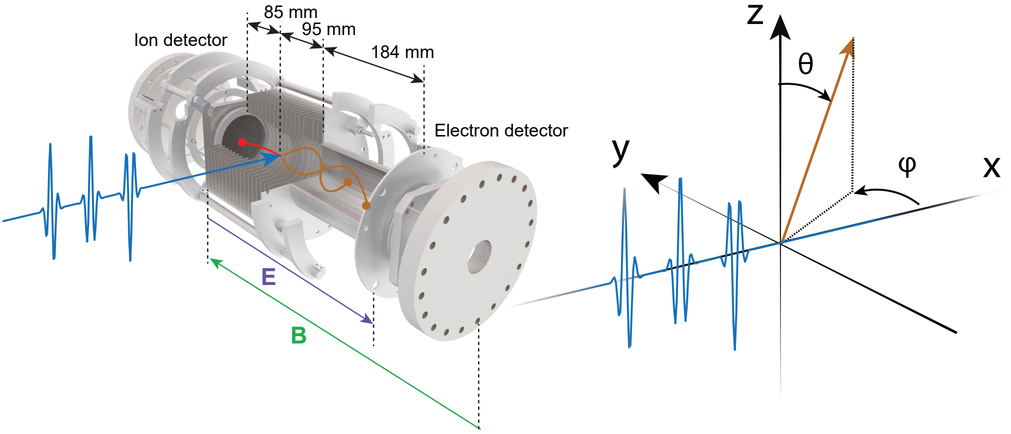

Figure 4.1: The CIEL. Schematic of the spectrometer, left and coordinate system, right.

1.1 Operating Principle

The goal of a reaction microscope is to collect all charged particles resulting from an interaction point and to record them in such a way that their initial momentum can be determined. In the CIEL spectrometer, as in a regular REMI, this is achieved by the application of electric and magnetic fields. A uniform electric field is applied over an extraction region, which drives the electrons and ions in opposite directions towards their respective detectors, but leaves their transverse momentum unchanged. Electrons with high kinetic energies and significant transverse momentum components are likely to escape the spectrometer before they reach the detector, and in order to confine them a uniform magnetic field is applied.

The motion of charged particles in electromagnetic fields is governed by the simple Lorentz force equation:

$$\mathbf{F} = q(\mathbf{E} + \mathbf{v} \times \mathbf{B}). \tag{4.1}$$

The magnetic field acts only on the transverse momentum components, and as a result the electrons follow helical-like trajectories, with a radius that depends on their transverse momentum. While the impact is large on the electrons, the ions have a higher mass and the impact of the magnetic field on them can be neglected. Their higher mass also means that they travel slower and thus a shorter distance to the detector is required. The ion side of the spectrometer thus only consists of an extractor region, and the detector is placed directly after the electric field.

The electron spectrometer consists of an extraction region and a flight tube, see Figure 4.1. The additional acceleration-free drift region in the flight tube serves to separate the electrons further in time thus increasing the time resolution, and to ensure the electrons complete the right amount of turns of helical motion. For TOF spectrometers that aim for an exceptional energy resolution, the flight tube can be as long as several meters. The CIEL docked at the HHG beamline is, in contrast, remarkably compact. The electron side fulfills the Wiley McLaren design criteria with the flight tube being twice as long as the extraction region [102], and the dimensions can be seen in Figure 4.1.

When using the spectrometer, the gas is delivered to the interaction region via a customized effusive jet with a long needle, mounted on a 3D translation stage for alignment. It can be biased to match the potential of the extraction field, thus minimizing distortions. In order to ensure a directional and confined effusive jet for the gas target, the needle has a length-diameter ratio of approximately 1000 [103]. In comparison to a molecular jet as commonly used in a COLTRIMS setup, this arrangement allows us to reach much higher gas densities in the interaction region.

Depending on the initial momentum of the electron, it will arrive at the detector at a time t and at a position x, y. By separating Equation 4.1 into longitudinal and transverse parts

$$\begin{aligned} \mathbf{F}_{||} &= eE\mathbf{z}, \\ \mathbf{F}_{\perp} &= -e\mathbf{v}_{\perp} \times B\mathbf{z} \end{aligned} \tag{4.2}$$

and solving the motion equations, it can be determined that the electron will arrive at the detector at a time

$$t = \frac{\sqrt{p_z^2 + 2meEd} - p_z}{eE} + \frac{mL}{\sqrt{p_z^2 + 2meEd}}, \tag{4.3}$$

where d is the length of the extraction region, and L is the length of the flight tube. This can be expressed as a polynomial equation in p_z which can be solved analytically [100]. In practice, if the energy gained through acceleration is much larger than the initial energy, $2meEd \gg p_z^2$, the solution can be well approximated by the simple equation:

$$p_z = eE(t_0 - t). \tag{4.4}$$

Here t_0 is the nominal time of flight of an electron with zero initial momentum:

$$t_0 = \sqrt{\frac{2md}{eE}\left(\frac{2d + L}{2d}\right)} \tag{4.5}$$

The transverse motion is independent from the accelerating electric field, and the electrons move in circular motion with a cyclotron frequency ω_c and period T_c:

$$\omega_c = \frac{eB}{m}, T_c = \frac{2\pi m}{eB}. \tag{4.6}$$

In order to detect the electron, the radius of this motion must be within the dimensions of the detector (assuming the interaction region is aligned well to the center of said detector). Again, through classical Newtonian equations of motions, the initial transverse momentum can be found to be:

$$
\begin{aligned}
p_x &= \frac{m\omega_c}{2}(x \cot \frac{\omega_c t}{2} + y), \\
p_y &= \frac{m\omega_c}{2}(y \cot \frac{\omega_c t}{2} - x).
\end{aligned}
\tag{4.7}
$$

After a cyclotron period, the electrons will return to their initial transverse position, and the corresponding time of flight is called a magnetic node. If the detector would be placed at a position corresponding to this time of flight, all electrons would hit the same position on the detector and Equation 4.7 could not be used: the momentum is not retrievable. These magnetic nodes reoccur after time of flights corresponding to the cyclotron period, but if the whole of the momentum distribution can be fitted within two such nodes, a complete reconstruction is possible without any loss of data. This is done with CIEL, and unlike in a regular REMI design where a few magnetic nodes can be present, this allows for recording of data in only one configuration and still obtain a complete dataset.

1.2 Detectors

Both the electron and ion sides of the CIEL are equipped with Position Sensitive Detectors (PSD), commercially available from RoentDek Handels GmbH. These detectors consist of a two stage Micro Channel Plate (MCP) followed by a delay-line anode. A charged particle hits the MCP and creates an electron avalanche (typically 10^7-10^8 charges) which in turn reaches the delay-line, consisting of two or more layers of copper wires. The electron cloud causes a signal to travel along the wires, and by measuring the relative delay between the signals as they arrive at the two ends, the position of the particle impact can be determined [104].

On the ion side of the spectrometer, a standard two-layer anode is installed. In principle, two orthogonal layers of wires is enough to determine exactly the position of impact—however, if several particles hit the detector within a time window shorter than the readout time of the wires, an ambiguity as to which signal originates from which event is introduced. This may be resolved if the events are sufficiently separated in position, but this is far from always the case. This becomes a problem especially if one intends to measure several electrons in coincidence, as their difference of TOF is short relative to the ions, and several hits may be expected within the readout time. To resolve this issue, a three layer anode Hexanode (HEX) delay-line was installed on the electron side of the detector. The added redundancy of the third layer significantly adds to the possibility of unambiguously reconstructing multi-hit events [105], and the spectrometer can be therefore be used to detect one ion in coincidence with several electrons.

2 XUV-IR Pump-Probe Photoionization Experiments

The methods commonly used today for attosecond science were first introduced as techniques for characterizing the temporal structure of XUV. Due to the lack of possible non-linear processes suited for the pulse energy of a typical attosecond pulse source, methods that are otherwise used to characterize ultrashort pulses as those discussed in Chapter 2 cannot be used. Instead, techniques using atomic gases in order to obtain a non-linear interaction were proposed [106, 107]. After the successful application of these techniques to characterize the XUV light, they have also been extensively used to study the photoionization process itself [11, 14, 16, 108].

The techniques used today in attosecond science are primarily attosecond streaking [68, 109] and RABBIT [10]. Both rely on two-color photoionization—specifically the photoionization by the XUV from HHG together with a weak near-IR pulse, usually a replica of the driving field, also often called a dressing field. The attosecond streaking technique requires single attosecond pulses, while RABBIT, which is traditionally used in Lund, instead requires a long pulse train. For HHG driven by the few-cycle system as used in this thesis, neither condition is practically achievable. The few-cycle driving pulses inherently leads to short pulse trains with only a handful of pulses, as described in Chapter 3. Neither stretching the driving pulses in order to generate long ATPs, nor additional compression in order to obtain SAPs, are preferable strategies since they are both rather wasteful approaches not suited for driving lasers with low energy. It is possible to retrieve an arbitrary XUV field from a two-color photoionization measurement using techniques such as Frequency-Resolved Optical Gating for Complete Reconstruction of Attosecond Bursts (FROG-CRAB) [110], but a better understanding of the underlying physics would be beneficial when applying these pulses for atomic physics applications.

In this thesis work, the characteristics of photoionization by short attosecond pulse trains was explored, and is presented in this section. The basics of photoionization by attosecond pulses are introduced, first by only an XUV field, and then also in the presence of a dressing IR field. Simulation and experiment results from XUV-IR ionization by SAPs, pulse trains and by a few attosecond pulses are presented, and the results of **Papers IV**, **V**, and **VI** are discussed.

2.1 Theory

2.1.1 Single color ionization

The probability $P(\mathbf{p})$ of detecting an electron with momentum **p** depends on the transition amplitude $a(\mathbf{p})$:

$$P(\mathbf{p}) \propto |a(\mathbf{p})|^2. \tag{4.8}$$

Perturbation theory can be used to derive an expression for the transition amplitude [111]:

$$a(\mathbf{p}) = -i \int_{-\infty}^{\infty} \mathrm{d}t \, \mathbf{d}(\mathbf{p}) \cdot \mathbf{E}_{\mathrm{XUV}}(t) \exp\left[\frac{i}{\hbar}\left(I_{\mathrm{p}} + \frac{\mathbf{p}^2}{2m}\right) t\right] \tag{4.9}$$

where $\mathbf{E}_{\mathrm{XUV}}$ is the light field, I_p is the ionization potential, and

$$\mathbf{d}(\mathbf{p}) = \mu(\mathbf{p}) e^{-i\phi_{at}(\mathbf{p})} \tag{4.10}$$

is the dipole transition matrix element, which contains all information about the atom. For hydrogen-like systems, this takes a relatively simple form [112]:

$$\mu(\mathbf{p}) \propto \frac{\mathbf{p}}{(\mathbf{p}^2 + 2I_{\mathrm{p}})^3}, \quad \phi_{at}(\mathbf{p}) \equiv 0. \tag{4.11}$$

Figure 4.2 shows the resulting photoelectron momentum distribution calculated according to this model in the simplest possible case. Here helium is photoionized by a single attosecond pulse with a central energy of 30.6 eV, corresponding to the 21st harmonic of 800 nm, and a duration of 300 as. The energy of the light pulse exceeds that of the ionization potential of the helium atom, 24.6 eV, and the result is an EWP from ionization with a probability distribution according to Equations 4.8 and 4.9. To the left in Figure 4.2 is a 3D representation, where the distribution is plotted as an isosurface at a third of the maximum probability density. Two lobes along the polarization axis can be seen, typical of a dipole transition from an s-state to a p-continuum. Due to the symmetry around the polarization axis, the distribution can be integrated along the azimutal angle φ without any information being lost, and the result is shown to the right.

When using a pulse train instead of an SAP, the interference between the EWPs ionized by the different attosecond pulses can be observed as in Figure 4.3. Since the EWPs directly take on the properties of the ionizing optical pulse, we expect photoelectron peaks corresponding to absorption by odd order harmonics of the driving IR field, although shifted down by the ionization potential. The 3D distribution now looks like a series of nested bowls, while the 2D distribution shows half-circle structures.

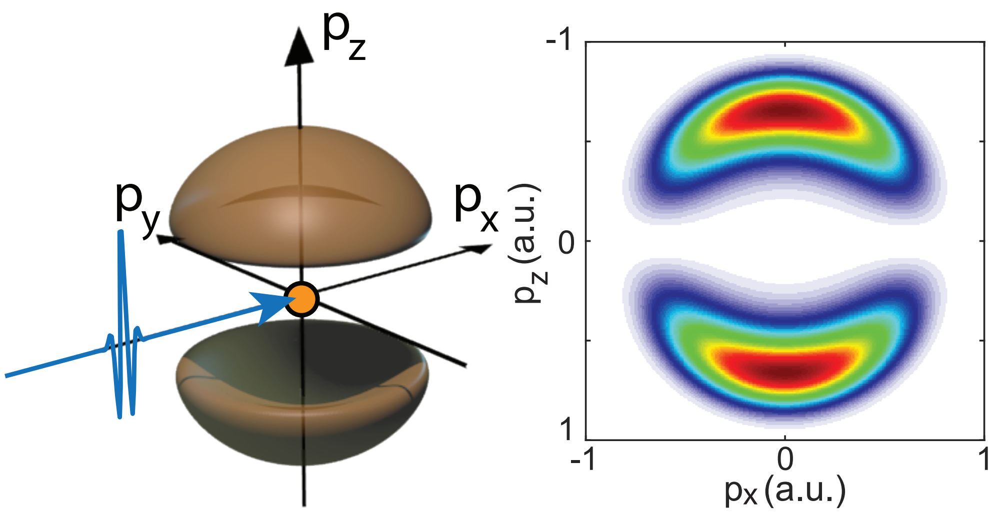

Figure 4.2: Ionization by SAP. To the left: 3D representation of an EWP in momentum space ionized by a 300 as SAP with a central energy of 30.6 eV, shown as an isosurface at a third of the maximum probability density. To the right: The same EWP integrated along the azimutal angle.

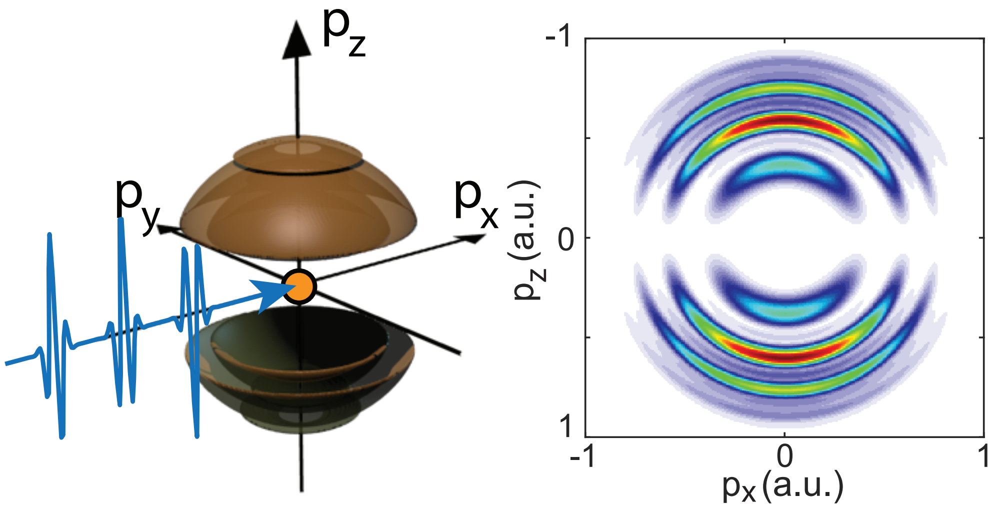

Figure 4.3: Ionization by APT. To the left: 3D representation of an EWP in momentum space ionized by an attosecond pulse train, shown as an isosurface at a third of the maximum probability density. To the right: The same EWP integrated along the azimutal angle.

2.1.2 Two-color ionization

In order to understand two-color photoionization techniques such as streaking or RABBIT, an additional dressing field must be added to the ionization description. The addition of such a laser field can be described within the SFA [76, 113], which was developed to describe high-harmonic generation and other strong field effects. Note that in the case described here neither a strong XUV nor IR field is assumed. The approximation still holds since the XUV ionization step ensures that the subsequent behavior of the photoelectron is not significantly impacted by the atomic potential [109]. According to the SFA, the transition amplitude becomes:

$$a(\mathbf{p}) = -i\int_{-\infty}^{\infty} \mathrm{d}t\, \mathbf{d}\left[\mathbf{p} + e\mathbf{A}(t)\right]\cdot \mathbf{E}_{\mathrm{XUV}}(t) \times \exp\left[\frac{i}{\hbar}\left(I_{\mathrm{p}} + \frac{\mathbf{p}^2}{2m}\right)t\right] \times \exp\left[i\phi_{IR}(\mathbf{p},t)\right] \tag{4.12}$$

where $\mathbf{A}(t) = -\partial\mathbf{E}(t)/\partial t$ is the vector potential of the dressing field and $\phi_{IR}(\mathbf{p},t)$ takes the form

$$\phi_{IR}(\mathbf{p},t) = -\frac{1}{2m\hbar}\int_{t}^{+\infty} \mathrm{d}t' \left[2e\mathbf{p}\cdot\mathbf{A}(t') + e^2\mathbf{A}^2(t')\right]. \tag{4.13}$$

The expression can be understood as a semi-classical two step process; the ionization step (which is the same as Equation 4.9), with the dipole transition element altered in the presence of the dressing field: $\mathbf{d}\left[\mathbf{p} + e\mathbf{A}(t)\right]$, and then the motion in the continuum after ionization as represented by the phase $\phi_{IR}(\mathbf{p},t)$.

In the case of XUV-IR pump-probe measurements using attosecond pulses or pulse trains, the intensity of the dressing IR field is generally weak, motivating the assumption that $|e\mathbf{A}| \ll |\mathbf{p}|$. This allows for simplification of Equations 4.12 and 4.13 to

$$a(\mathbf{p}) = -i\int_{-\infty}^{\infty} \mathrm{d}t\, \mathbf{d}(\mathbf{p})\cdot \mathbf{E}_{\mathrm{XUV}}(t) \times \exp\left[\frac{i}{\hbar}\left(I_{\mathrm{p}} + \frac{\mathbf{p}^2}{2m}\right)t\right] \times \exp\left[i\phi_{IR}(\mathbf{p},t)\right] \tag{4.14}$$

with

$$\phi_{IR}(\mathbf{p},t) = -\frac{1}{2m\hbar}\int_{t}^{+\infty} \mathrm{d}t' 2e\mathbf{p}\cdot\mathbf{A}(t'). \tag{4.15}$$

As a first approximation it can be assumed that the strength of $\mathbf{A}(t)$ does not vary significantly over the pulse train, i.e. $\mathbf{A}(t) = \mathbf{A}_0\cos(\omega_0(t-\tau))$, where τ is a temporal delay indicating the timing between the two fields, which gives:

$$\begin{aligned}\phi_{\mathrm{IR}}(\mathbf{p},t) =& -\frac{e}{m_e\hbar}\int_{t}^{+\infty} dt'\ \mathbf{p}\cdot\mathbf{A}_0\cos[\omega(t'-\tau)]\\ =& \frac{e\mathbf{p}\cdot\mathbf{A}_0}{m_e\hbar\omega}\sin[\omega(t-\tau)].\end{aligned} \tag{4.16}$$

If the attosecond pulses are short enough that there is no significant variation of $\mathbf{A}(t)$ over a single pulse, each pulse in the train receives the same phase but with opposite sign. For pulse number m in the train, the phase term then further reduces to

$$\phi_{\text{IR}}\left(\mathbf{p}, m\right) = -\frac{e\mathbf{p}\cdot\mathbf{A}_0}{m_e\hbar\omega}(-1)^m \sin(\omega\tau) = \eta_p(-1)^m. \tag{4.17}$$

where $\eta_p = -\frac{e\mathbf{p}\cdot\mathbf{A}_0}{m_e\hbar\omega}\sin(\omega\tau)$.

By regarding the XUV field as a train of pulses labelled by an index m, and introducing the denotation $\Omega_p = I_p/\hbar + \mathbf{p}^2/2m_e\hbar$, the transition amplitude becomes

$$a(\mathbf{p}) \approx -i\mathbf{d}(\mathbf{p})\cdot\sum_m \exp(i\phi_{\text{IR}}\left(\mathbf{p}, m\right))\int_{-\infty}^{+\infty} dt\mathbf{E}_m(t)\ \exp(i\Omega_p t). \tag{4.18}$$

By replacing the Fourier integral with the XUV amplitude in the spectral domain, Equation 4.18 becomes:

$$a(\mathbf{p}) \approx -i\mathbf{d}(\mathbf{p})\cdot\sum_m \tilde{\mathbf{E}}_m(\Omega_p)\exp(i\eta_p(-1)^m). \tag{4.19}$$

If $|\eta_p| \ll 1$, then

$$\exp(i\phi_{IR}(\mathbf{p}, m)) \approx 1 - i\eta_p(-1)^m, \tag{4.20}$$

and finally,

$$a(\mathbf{p}) \approx -i\mathbf{d}(\mathbf{p})\cdot\sum_m \tilde{\mathbf{E}}_m(\Omega_p)\left[1 - i\eta_p(-1)^m\right]. \tag{4.21}$$

Here the sum over the individual pulses $\tilde{\mathbf{E}_m}$ can be recognized as using the same principle as the multiple interference model in Chapter 3. That model can easily be plugged into 4.21. To continue the analysis, the multiple interference model from 3.8 can be expressed as

$$\tilde{\mathbf{E}}_m(\Omega)\exp\left[i(m\pi + t_m\Omega + \phi(\Omega))\right] = (-1)^m\tilde{\mathbf{E}}'_m(\Omega)\exp\left[im(\pi/\omega)\Omega\right], \tag{4.22}$$

where the π phase flip is identified as simply a sign flip and the train is assumed to be centered at zero.

This gives the transition amplitude as the sum of two terms

$$\begin{aligned}
a(\mathbf{p}) &\approx a_1(\mathbf{p}) + a_2(\mathbf{p}),\\
a_1(\mathbf{p}) &= -i\mathbf{d}(\mathbf{p})\cdot\sum_m(-1)^m\tilde{\mathbf{E}}'_m(\Omega)\exp\left[im(\pi/\omega)\Omega\right]\\
a_2(\mathbf{p}) &= -\eta_p\mathbf{d}(\mathbf{p})\sum_m \tilde{\mathbf{E}}'_m(\Omega)\exp\left[im(\pi/\omega)\Omega\right].
\end{aligned} \tag{4.23}$$

The two terms represent the one-photon transition and two-photon transition, respectively, and the coherent sum of the two gives the total probability density. In fact, the two terms are two different trains of EWPs, where single-photon transition $a_1(\mathbf{p})$ retains the phase flip that results in electron peaks corresponding to ionization by odd order harmonics while the two-photon transition term does not, and therefore results in a spectrum of peaks corresponding to even harmonics.

$$\begin{aligned} \mathbf{E}_o &= \sum_m (-1)^m \tilde{\mathbf{E}}'_m(\Omega) \exp\left[im(\pi/\omega)\Omega\right] \\ \mathbf{E}_e &= \sum_m \tilde{\mathbf{E}}'_m(\Omega) \exp\left[im(\pi/\omega)\Omega\right]. \end{aligned} \tag{4.24}$$

It can also be immediately noted that if the two terms have no spectral overlap, then $P(\mathbf{p}) = \left[a_1(\mathbf{p}) + a_2(\mathbf{p})\right]^2 = a_1(\mathbf{p})^2 + a_2(\mathbf{p})^2$. If, however, the harmonics are broad enough that there is overlap between the even and odd orders, interference effects are to be expected. Especially it can be observed that the sign of η_p depends on the sign of the final momentum component along the polarization axis—i.e. the emission direction along the polarization axis. In general, an additional π phase shift is to be expected when comparing emission along the polarization axis in the positive direction (up), versus the negative direction (down).

2.2 Simulations and Experiments

2.2.1 Single Attosecond Pulses and Attosecond Streaking

In the case of an SAP, the description of interference between EWPs becomes redundant. The effect of the presence of the IR field can easily be understood as the ionized electron being classically accelerated in the IR field after ionization. Figure 4.4 shows the result of an SFA simulation for an SAP in the presence of a 6 fs IR field with an intensity of $1{\cdot}10^{13}$W/cm^2. The left shows the waveform of the IR field and the envelope of the XUV, and the XUV spectrum (blue), which lies above the ionization potential of helium (gray line). To the right is the photoelectron momentum distribution. The same two lobes are observed as in the XUV only case in Figure 4.2, only shifted upwards along the polarization axis and with some minor distortions at the wings of the lobes.

This shift can be understood as a simple exchange of momentum with the IR field in the continuum. The size of the shift in the momentum distribution is proportional to the integration of the vector potential $\mathbf{A}(t)$ from the time of ionization by the XUV pulse to infinity.

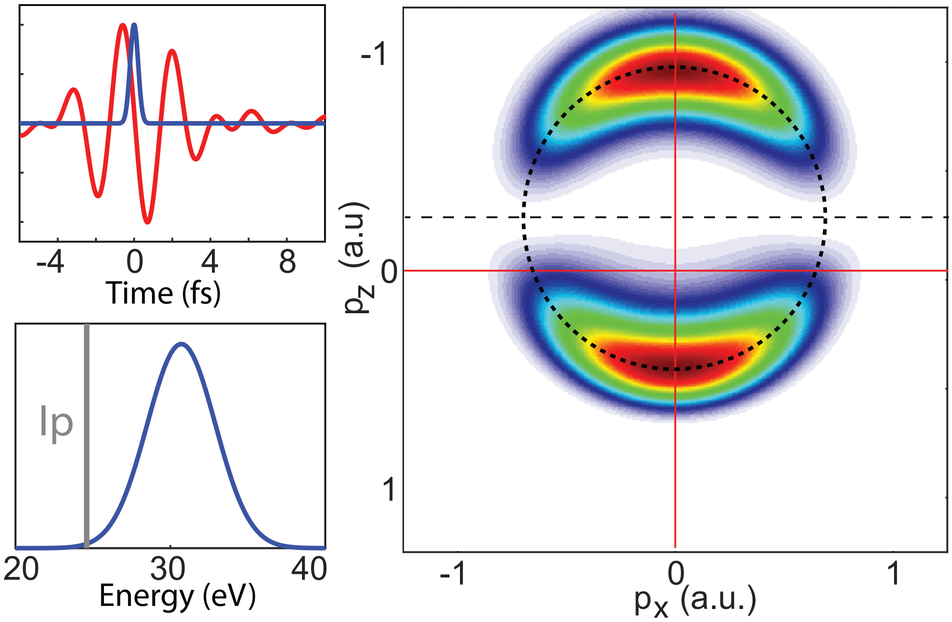

Figure 4.4: Two-color ionization of a SAP and a IR dressing field. Top left: The IR waveform and envelope of the SAP. Bottom left: The spectrum of the SAP (blue), and the ionization potential of helium (gray). Right: The resulting EWP momentum distribution given a IR intensity of $1{\cdot}10^{13}$ W/cm^2.

By analogy to conventional streaking, where time information is mapped onto space, in attosecond streaking, time information is mapped in the energy domain through the acceleration and deceleration of the emitted photoelectrons by the IR field. Depending on the timing between the IR and XUV field, the shift will vary, essentially tracing the vector potential of the IR field. In order to obtain a clear streaking trace, the IR field must be linearly polarized and CEP stabilized. The momentum of the emitted electron is changed by the IR field according to the simple classical relations:

$$\mathbf{p} = \mathbf{p}_0 - e\mathbf{A}_{IR}(\tau), \tag{4.25}$$

where τ is the delay between the XUV and IR fields. In order for this classical, intuitive regime to hold, the electron kinetic energy gained through ionization must also be high enough that it is not significantly affected by interactions with the parent ion [114].

Figure 4.5 shows a simulated streaking trace with an SAP numerically produced by spectrally gating the cut-off region of HHG driven by a single cycle 2.6 fs pulse. The same driver is then used as a probe for the streaking measurement with an intensity of $1.2{\cdot}10^{11}$ W/cm^2. Such experimental conditions could theoretically be possible in our laboratory, if additional

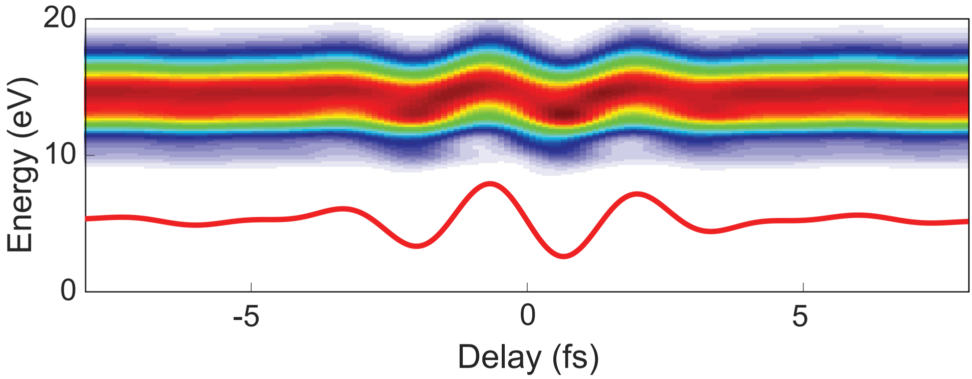

Figure 4.5: Streaking. A streaking trace of an SAP by a 2.6 fs dressing field with an intensity of 1.2·10^{11} W/cm^2. The vector potential $A(t)$ is shown below the streaking trace in red.

pulse compression was applied to the laser output. The red line added below the streaking trace is the vector potential of the IR field. Clearly the shape of the streaking trace follows the waveform of the vector potential. At the lower edge of the spectrum, some distortions are visible, which hint at interference effects due to imperfect filtering to achieve an SAP at these energies.

The attosecond streaking technique has been applied to measure photoionization dynamics by comparing streaking traces from different processes, for example ionization from different states of the same atom. In this case two traces will be recorded, at different energies, and any possible delay or phase shift between the two ionization processes will be encoded as a shift between the two streaking traces.

2.2.2 Long Pulse Trains and RABBIT

Figure 4.6 shows the result of an SFA simulation for a long attosecond pulse, generated by a 20 fs IR pulse in the presence of an IR field of the same duration. Again, the waveform of the IR field and XUV envelope, and the XUV spectrum is shown to the left. To the right is the photoelectron momentum distribution, with a dressing IR field intensity of 2·10^{11}W/cm^2—note that this is almost two orders of magnitude lower field strength compared to the SAP case.

In contrast to the SAP result, now the momentum distribution remains centered. The IR field instead results in new structures which appear between the half-circles which correspond to the harmonics—these are called sidebands. Since this is the result of a two photon transition, they appear in the position corresponding to absorption of even harmonics, in accordance with equation 4.24. In this case there is no significant overlap between the

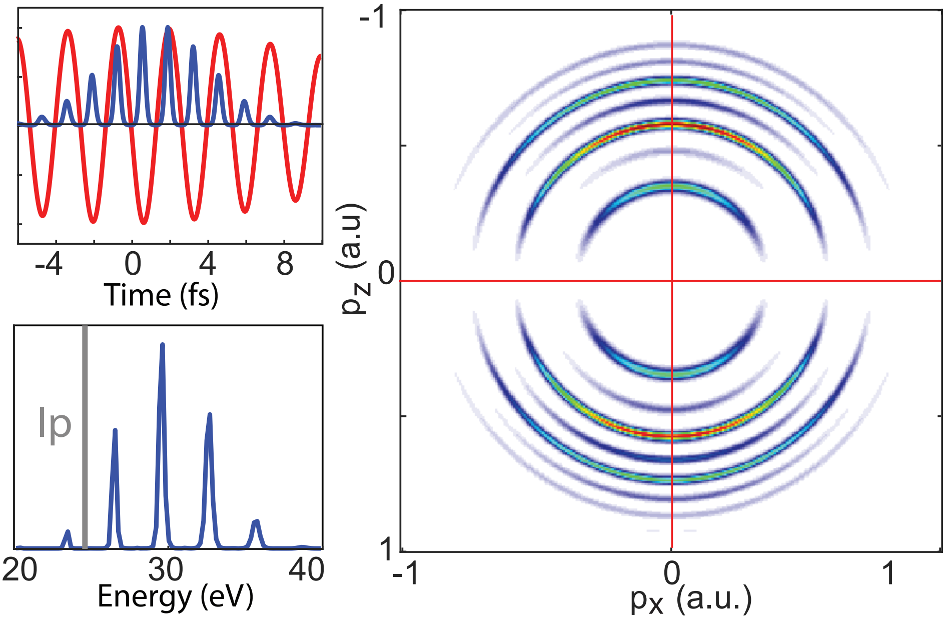

Figure 4.6: Two-color ionization with an APT and a IR dressing field. Top left: The IR waveform and envelope of the APT. Bottom left: The spectrum of the APT (blue), and the ionization potential of helium (gray). Right: The resulting EWP momentum distribution given a IR intensity of $1.2{\cdot}10^{11}$ W/cm^2.

spectrum of the one and two photon transitions. The strength of the sidebands is simply determined by η_p so that $a_2(\mathbf{p})^2 \propto \sin^2(\omega\tau)$, and results in oscillations at 2ω when the delay is varied.

These sideband oscillations are used in the interferometric technique called RABBIT – reconstruction of attosecond beating by interference of two-photon transitions. In the previous discussion, the apperance of the sidebands has been explained using the SFA model, and understood as a result of interference between EWPs; in this model, no information about the atom is present. In the RABBIT picture, the sidebands are explained in a fully quantum mechanical picture as the results of two photon transitions and their associated transition matrix elements, which depend explicitly on the atom. A sideband can be reached through two different quantum paths–the absorption of one XUV photon plus one IR photon, or absorption of one XUV photon of the subsequent harmonic plus emission of one IR photon, as shown to the right in Figure 4.7. Accordingly, the signal of sideband q, at a position corresponding to absorption of the q-th harmonic of the fundamental field, is the coherent sum of the transition amplitude of the two paths:

$$\begin{aligned} S_q &= |\mathcal{A}_{abs} + \mathcal{A}_{emi}|^2 \\ &= |\mathcal{A}_{abs}|^2 + |\mathcal{A}_{emi}|^2 + 2|\mathcal{A}_{abs}||\mathcal{A}_{emi}|\cos(2\omega\tau - \Delta\varphi) \end{aligned} \tag{4.26}$$

where $\mathcal{A}_{abs}$ and $\mathcal{A}_{emi}$ denote the two-photon transition amplitudes of the absorption of the $q-1$ harmonic plus absorption of an IR photon, and absorption of the $q+1$ harmonic and emission of an IR photon, respectively, τ is the delay between the IR and XUV fields, and $\Delta\varphi$ is an additional phase difference between the two different paths. If the delay τ is well controlled, the variation of $\Delta\varphi$ over the harmonics can be extracted by measuring the oscillation phase of the sidebands. The main contribution to this phase comes from the harmonics themselves, and the technique was indeed first suggested as a means to measure the phase differences between harmonics [106] and used experimentally to reconstruct the attosecond pulse train [10].

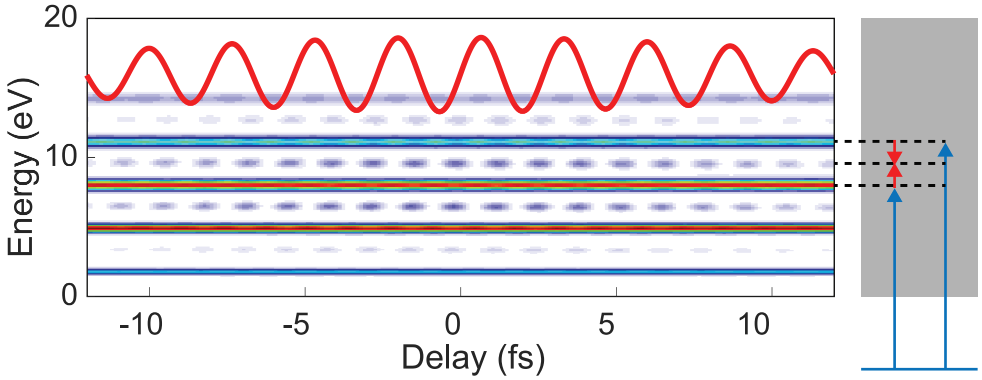

Figure 4.7: RABBIT. A RABBIT trace of an ATP by a 20 fs dressing field with an intensity of 1.2·10^{11} W/cm^2. The vector potential $A(t)$ is at the top in red.

Figure 4.7 shows, to the left, a RABBIT trace simulated by using the multiple interference model for HHG and SFA for the ionization step. The dressing IR field during the photoionization step has an intensity of 1.2·10^{11}W/cm^2. The vector potential of the dressing field is shown in red. Oscillations of the sidebands at twice the driving frequency of the IR field can be seen, in accordance with Equation 4.26. Note that the sideband oscillations coincide with the zero-crossings of the vector potential, i.e. the maximum alteration from the XUV only case appears at a half-cycle offset from the streaking trace.

This can be understood by seeing the RABBIT trace as pulse train interference, where a phase shift is applied through the IR field. If the same phase is applied to all pulses, then no change should be observed. For a single EWP, the phase shift from the ϕ_{IR} term in Equation 4.12 comes from the integration of the vector potential from the time the

EWP is born in the continuum, to the end of the IR pulse. If the EWP is born at a zero-crossing of the vector potential, all subsequent half cycles will more or less cancel each other out. Thus the streaking shift is maximized when the EWP is born at the peak of the half cycle. In a pulse train, however, the appearance of sidebands occurs when there is a phase difference between subsequent EWPs, so that their interference condition changes. The main contribution to that phase difference then comes from the integration of the vector potential from the time the EWP is born in the continuum, to the next zero-crossing—after which the following half-cycles will more or less cancel each other out. If the EWP is born at a zero crossing, this phase is maximized, and so is the alteration to the pulse train interference; the sidebands.

Paper V investigates the possible sources for errors when using RABBIT. It shows the importance of interferometer stability, and that for a set acquisition time, one should aim for a large number of sampling points rather than counts per point. Most importantly for the other work of this thesis, it was shown through SFA simulations how the error in a RABBIT analysis increases significantly once the pulse duration of the driver falls below 10 fs. This is a consequence of the fact that the RABBIT technique finds the average pulse in the pulse train, and when using a few-cycle driver, there is no such average. For a few cycle system such as the one used in this thesis, the RABBIT analysis is then no longer appropriate.

In contrast to the classical picture used when describing attosecond streaking, a quantum mechanical picture based of photons and quantum path interference is used to describe RABBIT. If the SAP and long APT train represent two different extremes, then one would expect in the few-cycle regime to at some point observe the transition from where a photon picture is most useful, to instead a classical framework.

2.2.3 Few-Cycle Regime/Short Pulse Trains

When considering XUV+IR ionization by a short pulse train generated by a few-cycle driver, it must from the outset be taken into account that the CEP of the driving field plays a major role. In Chapter 3, it was found that the structure of the APT depends strongly on the CEP, with the biggest difference being the number of pulses in the train. Figure 4.8 shows the XUV+IR 2D momentum distributions for the two extreme cases, CEP = 0 (three attosecond pulses), top row, and CEP = $\pi/2$ (two attosecond pulses), bottom row. The IR waveform, XUV envelope, and XUV spectrum are shown to the left. In the middle row, the 2D momentum distribution is shown, with distinctly different results in the two cases. For the CEP=0 case, a significant change can be observed in the up direction, where new structures appear between the original peaks corresponding to the harmonics. In the case of CEP= $\pi/2$, however, this is not the case. In fact, at first glance the difference between the XUV only and XUV+IR case is not obvious. Closer observation reveals that the half-circles corresponding to the harmonics have all been shifted slightly downwards. In both these cases, then, the symmetry has been broken—reminiscent of the SAP case—and we observe interference effects—reminiscent of the long APT case.

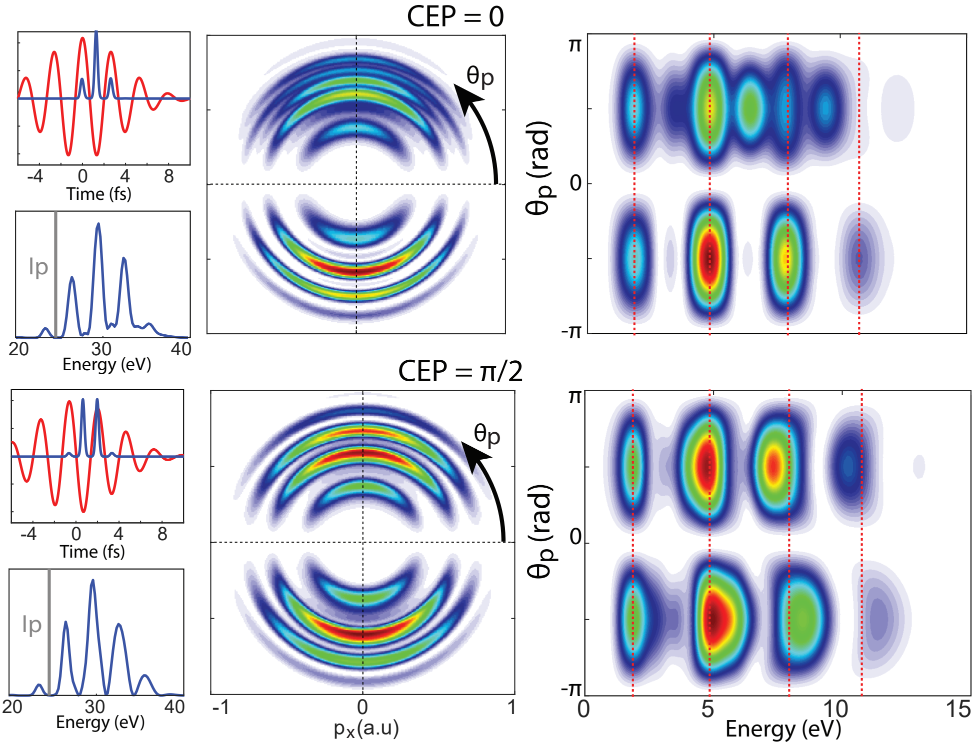

Figure 4.8: Two-color ionization by short pulse trains. The top (bottom) row shows the case where the driving field has a CEP=0 (CEP=$pi/2$), which results in three (two) attosecond pulses. Top left: The IR waveform and envelope of the APT. Bottom left: The spectrum of the APT (blue), and the ionization potential of helium (gray). Center: The resulting EWP momentum distribution given a IR intensity of 1.2·10^{11} W/cm^2. Right: The same EWP distribution plotted as polar angle vs. energy.

To better illustrate the case, the rightmost column show the two cases, but now as a function of kinetic energy and polar angle θ_p (marked in the central column). The positions corresponding to the absorption of odd harmonics are marked with dashed red lines. The effects are now much clearer—in the CEP=0 case indeed new structures are observed at the position corresponding to even harmonics, same as sidebands in the long APT case. However, they only appear in the up direction. In the CEP=$\pi/2$ case, instead the photoelectron peaks appear shifted from the position corresponding to odd harmonics, towards lower energies in the up-direction and higher energies in the down-direction—each individual harmonic is shifted like in the SAP case.

With the CIEL installed in the beamline the 3D momentum distribution in the cases simulated in Figure 4.8 was measured. In **Paper VI** the co-propagating XUV and IR after XUV generation were directly focused into the CIEL and a helium target. This utilizes the inherent synchronization between the two fields to fix a single delay. In Figure 4.9, results obtained after the installation of the interferometer are shown instead. To the left, experimental results and simulations are shown without IR, for reference. In the middle the two pulse case is shown. The shift of the harmonics, bigger at higher energies, can be clearly seen. To the right is the three pulse case, where sideband-like structures are observed in the down direction, while the main peaks in the up-direction remain the same.

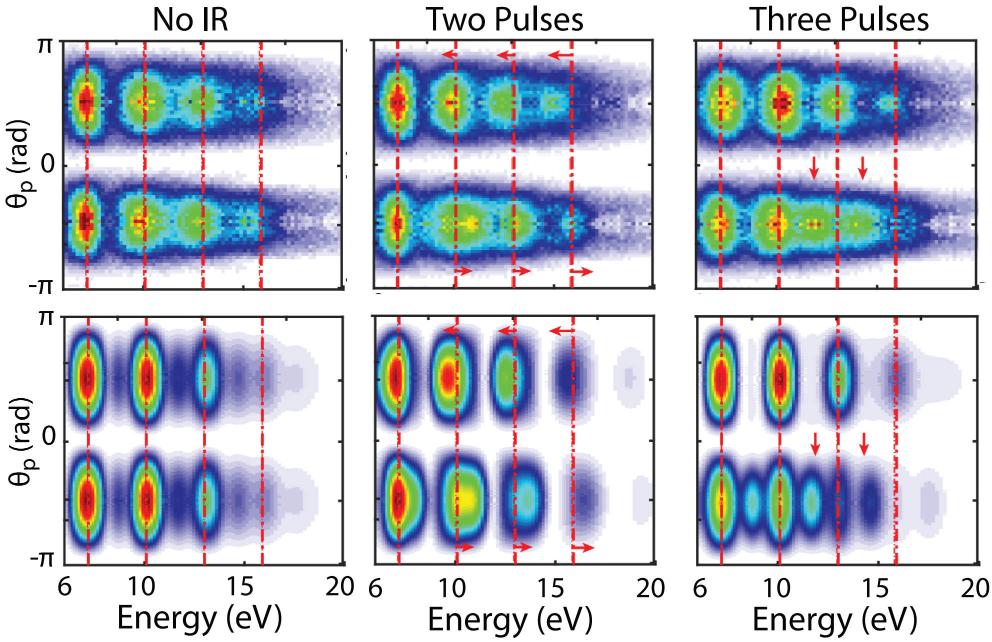

Figure 4.9: Comparison of 2D Photoelecton Spectrum. In all plots, the position corresponding to absorption of odd harmonics of the HHG driving field is marked by dashed red lines. Top row: Experimental results, bottom row: simulations. Leftmost column: XUV only. Middle column: XUV+IR with two attosecond pulses, corresponding to a CEP of the driver of $\pi/2$, showing shifts of the photoelectron peaks marked by red arrows. Rightmost column: XUV+IR with three attosecond pulses, corresponding to a CEP of the driver of 0, showing new structures for $\theta_p < 0$ (down direction), marked by red arrows.

Fundamentally, these results can be understood through the analogy of slit diffraction experiments, as introduced in Chapter 2.

2.2.3.1 Two Pulses The two pulse case is most analogous to the simplest double slit experiment, where the two EWPs ionized by the XUV are the slits. The IR introduces a phase modulation, which is opposite for the two slits—in practice, this can be thought of as a phase shift from some dispersive media, see Section 1.3, and shifts the resulting interference peaks. This case is illustrated in Figure 4.10. To the left are shown the EWP envelopes in time, and to the right, the kinetic energy spectrum. In the first row, two EWPs in blue produce a classic interference pattern with equal fringe separation. An additional phase introduced to one of them shifts the fringes equally over the whole spectrum.

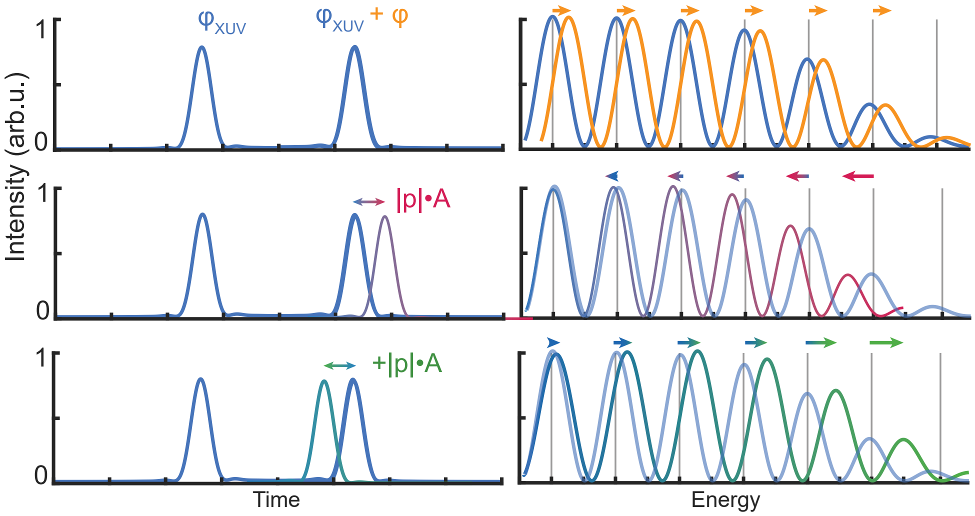

Figure 4.10: Interference between two EWPs. Left column: EWPs in time. Right column: Resulting interference in the energy domain. Top row: Two EWPs with a temporal separation results in interference peaks (blue). An additional phase applied to one of the pulses shifts the interference pattern along the energy axis. Middle row: An energy dependent phase shift applied to one of the pulses shown as a temporal shift, leading to a shift of the interference maxima which is bigger at higher energies (purple). Bottom row: Changing the sign of the phase shift from the middle row leads to shifts in the opposite direction (green).

In the case of our experiment, the IR field induces a phase difference which depends on the direction of emission, **p**, and the direction and magnitude of **A**. The phase difference is here shown applied to one of the pulses, instead of half of it applied to both with differing sign. Since $E_{kin} \propto \mathbf{p}.^2$, the phase shift is no longer constant over the spectrum, as observed in the experiment. If the sign of **p** changes, i.e. in the opposite direction, the shift will also reverse—compare row two and three in the figure.

An analytical model can also be made based on Equation 4.23. For two pulses ($m = 0, 1$)

with equal amplitude and phase, $E_m(\Omega) = E_0(\Omega)$,

$$E_e(\Omega) = E_0(\Omega)\left(1 - e^{i\frac{\Omega\pi}{\omega}}\right) = -2iE_0(\Omega)e^{i\frac{\Omega\pi}{2\omega}}\sin(\tfrac{\Omega\pi}{2\omega}) \tag{4.27a}$$

$$E_o(\Omega) = E_0(\Omega)\left(1 + e^{i\frac{\Omega\pi}{\omega}}\right) = 2E_0(\Omega)e^{i\frac{\Omega\pi}{2\omega}}\cos(\tfrac{\Omega\pi}{2\omega}). \tag{4.27b}$$

Which gives:

$$a_1(\mathbf{p}) = -2d(\mathbf{p})E_0(\Omega)e^{i\frac{\Omega\pi}{2\omega}}\sin(\tfrac{\Omega\pi}{2\omega}) \tag{4.28}$$

$$a_2(\mathbf{p}) = -2\eta_p(\tau)d(\mathbf{p})E_0(\Omega)e^{i\frac{\Omega\pi}{2\omega}}\cos(\tfrac{\Omega\pi}{2\omega}), \tag{4.29}$$

so that

$$\begin{aligned}&a_1(\mathbf{p}) + a_2(\mathbf{p}) = \\ &-2d(\mathbf{p})E_0(\Omega)e^{i\frac{\Omega\pi}{2\omega}}\left[\sin(\tfrac{\Omega\pi}{2\omega}) + \eta_p(\tau)\cos\left(\tfrac{\Omega\pi}{2\omega}\right)\right] \approx \\ &-2d(\mathbf{p})E_0(\Omega)e^{i\frac{\Omega\pi}{2\omega}}\sin(\tfrac{\Omega\pi}{2\omega} + \eta_p(\tau))\end{aligned} \tag{4.30}$$

This leads to

$$|a(\mathbf{p})|^2 \propto \sin^2(\tfrac{\pi\Omega}{2\omega} + \eta_p(\tau)). \tag{4.31}$$

When $\eta_p(\tau) = 0$, this represents a photo-electron distribution peaked at $\Omega = (2q + 1)\omega$, as excepted. The additional phase term provides a shift of the peaks towards higher or lower energies depending on the delay τ, i.e. the whole interference structure is streaked, much like the SAP spectrum in attosecond streaking. Since this phase term depends on the final momentum, the streaking amplitude increases together with the kinetic energy of the electrons.

2.2.3.2 Three Pulses The introduction of a third pulse/slit changes the nature of the interference. The addition of the interference between the first and the third pulse narrows the interference peaks and adds a sub-maximum in between the original peaks (although these are practically almost negligible if the amplitudes of the pulses in the train follow a Gaussian distribution). The addition of the phase shift introduced by the IR, however, will change the distribution of the main maxima and submaxima. Due to the fact that the IR field only changes sign with each consecutive pulse, the phase applied to the first and third pulses is in fact the same, and their phase relation does not change. This means that the structure imposed by those two pulses—harmonics at ω, since the separation between them is a whole IR period—will not change. However, the phase relation between the two satellites and the central pulse will change. This results in a change in distribution between the odd harmonics (main maxima) and the even harmonics (submaxima).

This is illustrated in Figure 4.11, similarly to the two pulse case. Again, the EWP envelopes

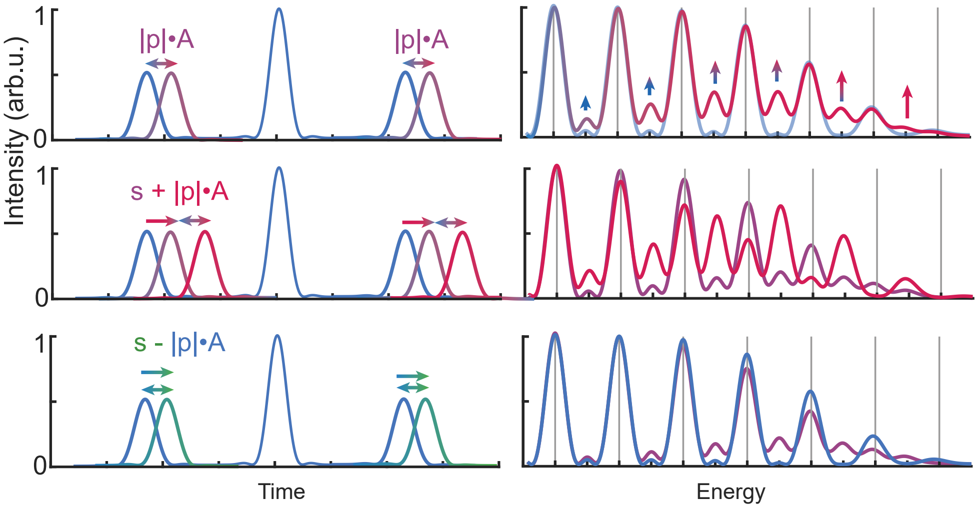

Figure 4.11: Interference between three EWPs. Left column: EWPs in time. Right column: Resulting interference in the energy domain. Top row: three EWPs with a temporal separation results in interference peaks (blue). An additional phase energy dependent phase applied the satellite pulses results in the appearance of sub-maxima (sidebands), that are stronger for higher energies (red). Middle row: With an starting phase difference s between the central and satellite pulses, the sideband amplitude is not originally zero (purple), and is increased further when an additional phase shift is applied (red). Bottom row: Changing the sign of the addition phase shift from the middle row leads instead to a decrease of the submaxima originally present (blue).

in time are shown to the left, and to the right, the kinetic energy spectrum. In this case, the phase shift is illustrated on the satellite pulses. In the first row, it is assumed that the pulse train is symmetrical, the only phase difference between the pulses is a π phase flip. When the phase shift is applied, this results is an increase of the amplitude of the submaxima. As in the two pulse case, this effect is stronger for higher energies. However, if the sign of $\mathbf{p}$ is now flipped, the result remains the same. Whether it is the left or the right satellite pulse that moves closer to the central one does not matter for the interference structure. An additional effect is required to break the symmetry.

This turns out to be the phase difference imprinted by the HHG, as explained in the discussion of the multiple interference model. In this representation, that means the pulses are not from the beginning equally spaced around the central pulse. This phase difference either adds with the phase shift from the IR, as in the second row in Figure 4.11, or counteracts it, as in the third row, depending on sign of $\mathbf{p}$, i.e. emission direction. This has the result of amplifying the sideband amplitude as in the second row, or suppressing it, as in the third row.

Let us now also analytically consider the case of three pulses, where we take $m = 0$ as the central pulse. This gives

$$E_o(\Omega) = E_0(\Omega)\left(1 - re^{i\frac{\Omega\pi}{\omega}+is} - re^{-i\frac{\Omega\pi}{\omega}+is}\right) = E_0(\Omega)\left(1 - 2re^{is}\cos(\tfrac{\Omega\pi}{\omega})\right) \tag{4.32a}$$

$$E_e(\Omega) = E_0(\Omega)\left(1 + re^{i\frac{\Omega\pi}{\omega}+is} + re^{-i\frac{\Omega\pi}{\omega}+is}\right) = E_0(\Omega)\left(1 + 2re^{is}\cos(\tfrac{\Omega\pi}{\omega})\right) \tag{4.32b}$$

where r is the amplitude ratio between the two outer 'small' pulses and the central one and s is the difference in spectral phase between the middle and the other pulses. This gives

$$a_1(\mathbf{p}) = -id(\mathbf{p})E_0(\Omega)\left(1 - 2re^{is}\cos(\tfrac{\Omega\pi}{\omega})\right) \tag{4.33a}$$

$$a_2(\mathbf{p}) = -\eta_p(\tau)d(\mathbf{p})E_0(\Omega)\left(1 + 2re^{is}\cos(\tfrac{\Omega\pi}{\omega})\right) \tag{4.33b}$$

so that

$$a_1(\mathbf{p}) + a_2(\mathbf{p}) = -d(\mathbf{p})E_0(\Omega)\left[i + \eta_p(\tau) + (-i + \eta_p(\tau))2re^{is}\cos(\tfrac{\Omega\pi}{\omega})\right]. \tag{4.34}$$

This leads to

$$\begin{aligned} |a(\mathbf{p})|^2 \propto & [1 + \eta_p(\tau)^2]\left(1 + 4r^2\cos^2(\tfrac{\Omega\pi}{\omega})\right) \\ & -[1 - \eta_p(\tau)^2]\cdot 4r\cos(\tfrac{\Omega\pi}{\omega})\cos(s) \\ & +[2\eta_p(\tau)]\cdot 4r\cos(\tfrac{\Omega\pi}{\omega})\sin(s). \end{aligned} \tag{4.35}$$

Neglecting the terms proportional to $\eta_p(\tau)^2$, approximating $2\eta_p(\tau)$ by $\tan(2\eta_p(\tau))$ and using the trigonometric identity $\cos(s+2\eta_p(\tau)) = \cos(s)\cos(2\eta_p(\tau)) - \sin(s)\sin(2\eta_p(\tau))$, finally expression 4.35 becomes:

$$|a(\mathbf{p})|^2 \propto 1 + 4r^2\cos^2(\tfrac{\Omega\pi}{\omega}) - 4r\cos(\tfrac{\Omega\pi}{\omega})\cos(s + 2\eta_p(\tau)) \tag{4.36}$$

The first two terms in this equation describe a base oscillation of the photoelectron distribution that peaks at all harmonics. This structure is then modulated by the last term, which, if the terms s and $\eta_p(\tau)$ are zero, will selectively cancel the even harmonic peaks. The combination of these phase terms then determine the nature of this suppression; when shifted by π, instead the odd harmonics are completely suppressed and only "sidebands" may be observed. Unlike in the two pulse case, the position of the peaks does not move, but rather only appear at multiples of the driving IR frequency, resembling the RABBIT situation with absorption/emission of photons.

2.2.4 Pump-Probe with a Few Attosecond Pulses

Due to the qualitative differences between the two and three pulse case when looking at a single delay between the XUV and IR field, the pump-probe spectrograms can also be expected to behave differently. Indeed, Figure 4.12 shows results in the same conditions as those used to simulate attosecond streaking and RABBIT. Here the driving pulse was 5.8 fs FWHM long, corresponding to the d-scan measurements of the laser system. With a CEP of $\pi/2$, this leads to the generation of primarily two pulses, see Figure 4.12 on the left. The resulting spectogram can be seen to be shifted up and down by the IR probe, much like an individual attosecond streaking trace for each harmonic. On the right, instead, a CEP of 0 leads to the generation of three pulses, and instead of shifting the photoelectron peaks as in the two pulse case, new peaks at the sideband positions appear. Unlike in a RABBIT trace, however, they now oscillate at the fundamental IR frequency instead of twice the IR frequency. This is due to the broken symmetry as described previously—when a sideband that would be expected in a RABBIT measurement is suppressed in one emission direction, it is instead observed in the opposite direction. The electrons emitted in the up/down direction are shown in the upper/lower row in Figure 4.12, respectively.

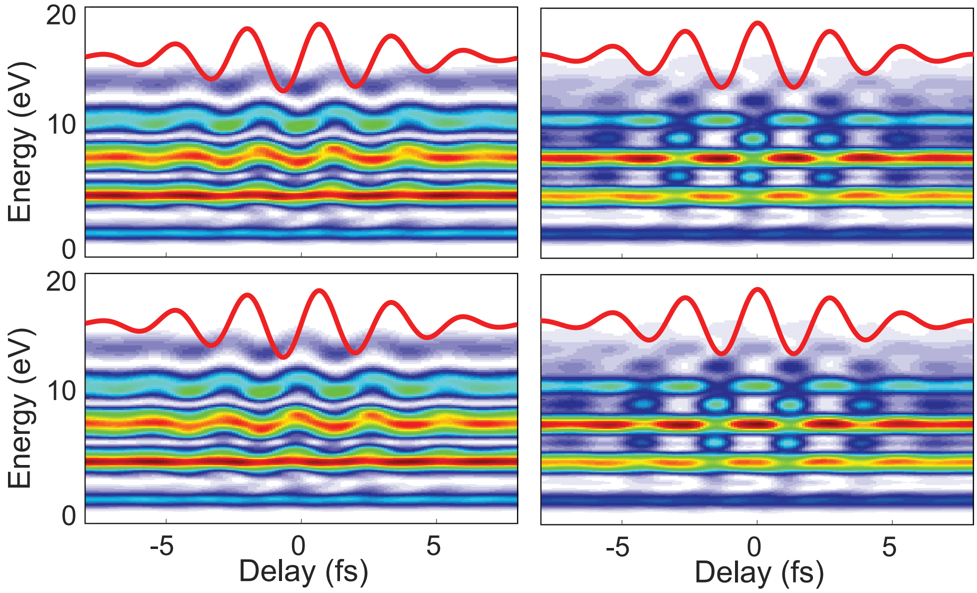

Figure 4.12: Simulated Delay Scans of Short Pulse Trains. Left column: two pulses (CEP=π/2). Right column: three pulses (CEP=0). Top row shows the spectrum in the up direction as a function of delay, and the bottom row the same in the down direction. The vector potential of the streaking field is indicated in red.

Again, it should be noted that for the two pulse case, although the result resembles a streaking trace for each harmonic, an interesting difference is that the oscillations no longer coincide with the vector potential. This is, again, because the shifts are best understood as an interference effect, and thus are maximized when the phase difference between the two pulses is maximized.

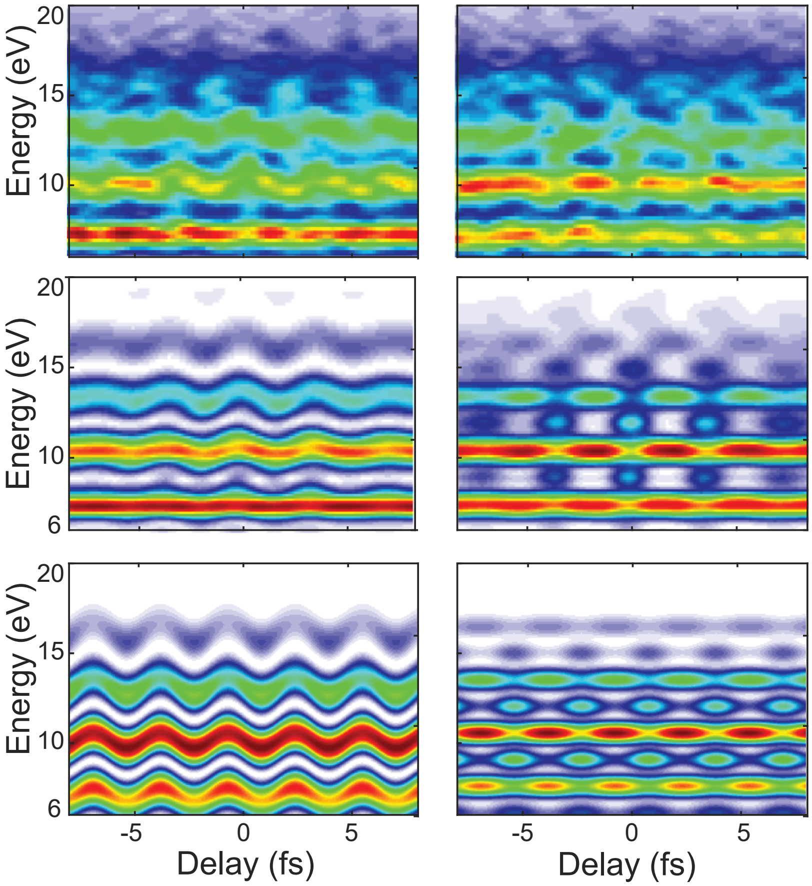

Figure 4.13: Delay Scans of Short Pulse Trains. Top row: Experimental Results. Middle row: SFA simulations. Bottom row: Simplified model. Left column shows the two pulse case (CEP=$\pi/2$) and the right column the three pulse case (CEP=0).

With the installation of the XUV-IR interferometer, measurements of XUV+IR photoelectron spectrum have been recorded as a function of delay. Figure 4.13 shows the experimental results (top row) and matching simulations, both using the full SFA (middle) and the simplified expressions in Equations 4.31 and 4.36 (bottom). Although the signal to noise ratio in the measurement is unfortunately not ideal, it is still possible to observe the same qualitative features in both the measured and simulated traces. Comparing the middle and bottom row, it should be noted that while the overall XUV spectrum has been chosen to fit the experiment, the complete structure of the vector potential of the IR is not taken into account in the simplified expression, only its carrier frequency. Still, the features of the delay traces are clearly replicated. The largest mismatch can be seen in the two pulse case for the lower energies, where the simple model shows strong modulation of the harmonic around 6 eV while this is not present in neither the SFA simulation nor the experiment. The reason is that the pulse train in this energy region no longer consist of just two pulses but rather four, and therefore the model no longer holds.

3 Double Ionization

Attosecond science has been very successful in investigating the phenomena of photoionization by a single photon. As the technology develops, the application of the techniques to new phenomena is a natural step. One such area of interest is the study of highly correlated systems. The concept of correlations, and, in its most extreme case, entanglement, is one of the most surprising and non-intuitive predictions of the theory of quantum mechanics. Although no longer controversial, the apparent contradiction to the nature of reality as observable by humans makes it a fascinating area of study.

One of the most fundamental processes that may produce highly correlated electron pairs is single-photon double ionization in atoms or molecules [115–117]. This happens when a single photon with a very high energy interacts with more than one bound electron in an atom at once, and two electrons may simultaneously leave the atom. Much effort has been put into finding a theoretical description of such a two-electron wavefunction, started already in the seventies [118, 119]. In 1991 Huetz et. al. [120] gave a detailed description of the wavefunctions given the quantum numbers L, M, S, and π (total orbital momentum, its projection, spin and parity). This was later extended into a description of general selection rules [121].

In particular, helium, with only two electrons in total, provides a good model system in which to study this fundamental three-body Coulumb problem [122]. In this case, the transition between singlet ground and continuum states $^1\mathrm{S}^e \rightarrow ^1\mathrm{P}^o$, also fulfills the criteria posed in [115] so that the continuum state may be entangled, and since the spin state does not change, the properties of this correlation are expected to be encoded in the spatial part of the wavefunction, which, unlike the spin, is possible to measure directly.

Measuring the spatial properties of the two electron wavefunctions has been practically possible for a long time at synchrotron facilities, where the threshold for single photon double ionization of helium at 79 eV is easily reached. By measuring the two electrons in coincidence, it is possible to determine the probability of emission direction of the second electron at a certain energy, given the defined direction and energy of the first. This so called Triply Differential Cross Section (TDCS) has been measured successfully for a range of excess energies and angular configurations [122, 123]. These measurements, however, are not capable of following the evolution of the correlation between the two emitted electrons in time. The application of techniques developed by attosecond science would open up that exciting possibility. Previously, attosecond interferometric techniques have been applied to double ionization of xenon, showing that different ionization mechanisms can be separated [124]—however, the repetition rate of the light sources available has, until now, been a huge limitation. In this thesis work, the double photoionization of helium has been studied with the high repetition rate laser system already presented, and as shown in **Paper IV**, with the CIEL spectrometer. For the first time, double photoionization of helium has been measured with an attosecond light source and the TDCS could be measured for different excitation energies.

3.1 Theory

The TDCS at threshold for helium can be derived analytically [120, 123, 125]. For a two-electron state with $^1\mathrm{P}^\mathrm{o}$ symmetry and equal energy sharing, meaning that both photoelectrons have equal energy $E_1 = E_2 = \hbar\omega/2$, this takes the form of:

$$\frac{d^3\sigma}{dE_1 d\Omega_1 d\Omega_2} = a_g(E_1, E_2, \theta_{12})\left(\cos\theta_1 + \cos\theta_2\right)^2, \tag{4.37}$$

where θ_1 and θ_2 are the emission angles of the two electrons with respect to the polarization axis, and Ω_1 and Ω_2 in this case denote the solid angle. The complex amplitude a_g can be parametrized according to a Gaussian ansatz as [120, 122]:

$$a_g(E_1, E_2, \theta_{12}) = a \exp\left(-4\ln 2\left[(\theta_{12} - 180^o)/\gamma\right]^2\right), \tag{4.38}$$

where a is a scaling factor, θ_{12} is the mutual angle between the two electrons, and γ is the full-width at half maximum correlation factor, which depends on the excess energy.

Figure 4.14 illustrates the characteristics of Equation 4.37. The black arrows represent the emission angle of the first electron, the purple arrows the XUV polarization direction, and the black lobes the full TDCS. The blue dashed line represents the $(\cos\theta_1 + \cos\theta_2)^2$ term, showing two lobes along the polarization direction. This term arises from the light matter interaction within the dipole approximation. The red dashed line shows the $a_g(E_1, E_2, \theta_{12})$ term, a single lobe oriented in the opposite direction of the first electron, and the combination of the two terms results in a typical two lobe structure (black), with the opening between the two lobes decided by γ. The top right illustration shows the impact of the emission angle of the first electron, for 90° (solid), 60° (dotted), and 30° (dashed). The bottom right show the effect of changing γ. The dotted line for $\gamma = 180^\circ$, the full line for

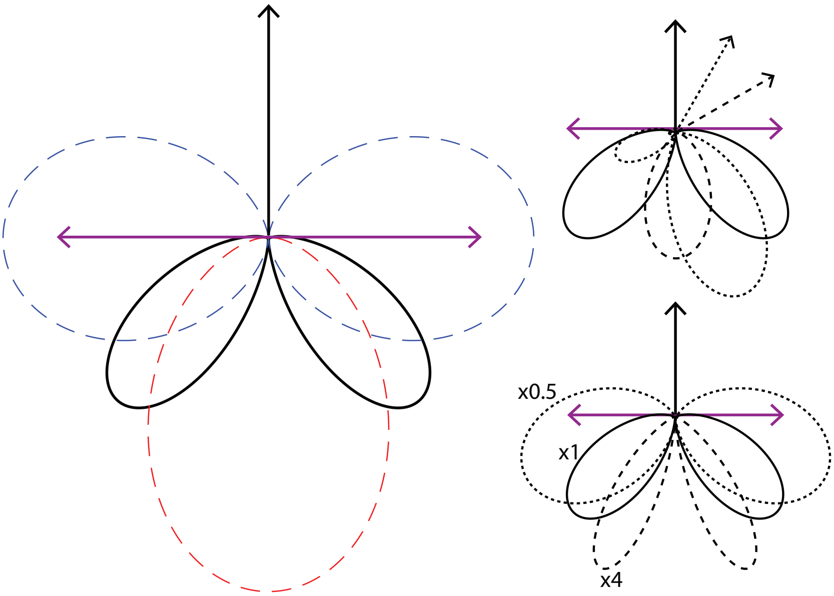

Figure 4.14: Theoretical TDCS. The polarization direction of the XUV is shown as a purple arrow. The black arrows show the emission direction of the first electron. Left: Illustration of the different part of Equation 4.37. In dashed blue, the light-matter interaction term, and in dashed red, the electron correlation term a_g. The combined TDCS is shown as a solid black. Top right: The TDCS for different emission angles of the first electron, 90° (solid), 60° (dotted), and 30° (dashed). Bottom right: The TDSC for different values of γ, $180°$ (dotted, scaled by a factor 0.5), $90°$ (solid), and $\gamma = 45°$ (dashed, scaled by a factor 4).

$\gamma = 90°$, and the dashed line for $\gamma = 45°$.

The most striking feature of these TDCS distributions is the node for back-to-back emission, which can be understood to be a result of the symmetry and selection rules. In the case of equal energy sharing, it may be explained as follows: With a final state of ${}^1\mathrm{P}^o$, the total wavefuntion has an odd parity, i.e. it should change sign after a spatial inversion operation:

$$\Psi(\mathbf{k}_1, \mathbf{k}_2) = -\Psi(-\mathbf{k}_1, -\mathbf{k}_2) \tag{4.39}$$

The total wavefunction must also be anti-symmetric according to the Pauli principle, i.e. it should change sign after an exchange operation. Since the singlet spin state is anti-symmetric, the orbital part must be symmetric:

$$\Psi(\mathbf{k}_1, \mathbf{k}_2) = \Psi(\mathbf{k}_2, \mathbf{k}_1) \tag{4.40}$$

In the special case of equal energy back-to-back emission, $\mathbf{k}_2 = -\mathbf{k}_1$, these two properties cannot hold at the same time, since:

$$-\Psi(-\mathbf{k}_1, -\mathbf{k}_2) = -\Psi(-\mathbf{k}_1, \mathbf{k}_1) \neq \Psi(-\mathbf{k}_1, \mathbf{k}_1) = \Psi(\mathbf{k}_2, \mathbf{k}_1). \tag{4.41}$$

The cross section therefore goes to zero. In general, this node can be observed for any state so that $S + \pi$ is odd. A rigorous derivation of the selection rules involved can be found in [121].

3.2 Experimental Challenges

The measurement of two photoelectrons in coincidence with the photoion presents a number of challenges. Figure 4.15 shows a HHG spectrum from neon (black) and the cross section for single ionization (solid red) and double ionization (dashed red) in helium. The difference in cross section between the single and double ionization is about of two orders of magnitude in this energy range [79, 126], which means that only one out of every hundred events are likely to be a double ionization event. While energies from a few eV up to >90 eV can be reached experimentally by generating HHG in neon, see Figure 4.15, the whole of the spectral range cannot be used. The cross section of the single ionization process close to threshold (24.5 eV) increases with an additional two orders of magnitude, and using all of the whole available spectral range would make the ratio of single to double ionization even worse. The XUV is therefore sent through a 200 nm zirconium filter which transmits only photon energies above 65 eV. This filter was coated with a thin layer of gold, to protect the zirconium from damage by the IR remaining after generation.

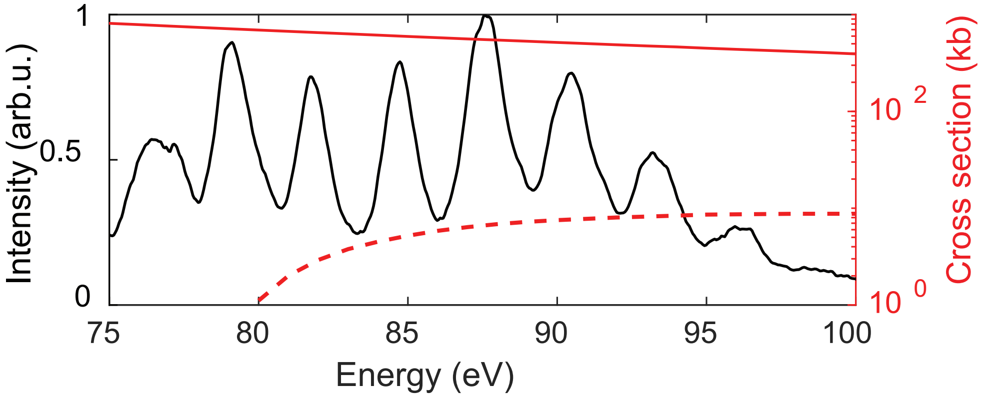

Figure 4.15: XUV spectrum and Cross Sections of Helium. XUV spectrum (solid black), single ionization cross section (solid red), and double ionization cross section (dashed red).

In order to sufficiently limit the likelihood of measuring false coincidence, i.e. in order to be able to safely say that the particles measured simultaneously are from only one event, the total event rate should be below a tenth of the repetition rate of the laser. With a repetition rate of 200 kHz, this means that the maximum rate of double ionization events in this experiment is 200 Hz. Additionally, the total detection efficiency of the two detectors can be expected to lie in the 15% range, and the maximum achievable event rate becomes 30 Hz. The photon flux of the source was optimized to reach a final event rate of 15 Hz. In addition, a large effort was devoted to increase the stability of the laser, so that acquisition over tens of hours was feasible.

3.3 Results

Figure 4.16 shows the measured TDCS for equal energy sharing of the two electrons (E_1=E_2=5±1 eV) with emission angles of the first electron of $\theta_1 = 90^\circ$, 60°, and 30° with respect to the polarization axis, and with a total kinetic energy $E_1 + E_2 = 10 \pm 1.5$ eV.

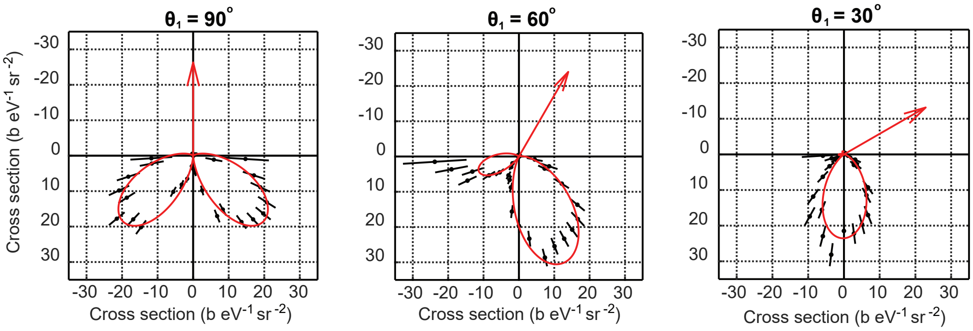

Figure 4.16: Measured TDCS. TDSC measured (black dots) and calculated according to Equation 4.37 (red) for three different emission directions of the first electron (red arrow); 90° (left), 60° (middle), and 30° (right).

The normalization is done according to the procedure from Bräuning et al. [127] using a value of the total cross section of 7.23 kb at 10 eV above threshold [126]. Through fitting Equation 4.37 for all emission angles θ_1 we find for this energy a value of $\gamma = 90^\circ \pm 3^\circ$. Previous reported values at this excess energy are approximately 85° [128]. However, theoretical calculations [99, 129] predict that the opening angle γ should be around 93° at this energy. Since the attosecond source is a broadband source, γ can be fitted at a range of different energies, and the results are shown in Figure 4.17. The red dots are the values extracted from this measurements, black is the theory from [129], and previous measurements are shown with black symbols [128, 130, 131]. Good agreement with theory is found, especially in the range from 5-9 eV.

The broad spectral width of the source also allows us to illustrate the wave-packet like nature of the second electron. By not filtering over the energy of the second electron the behavior

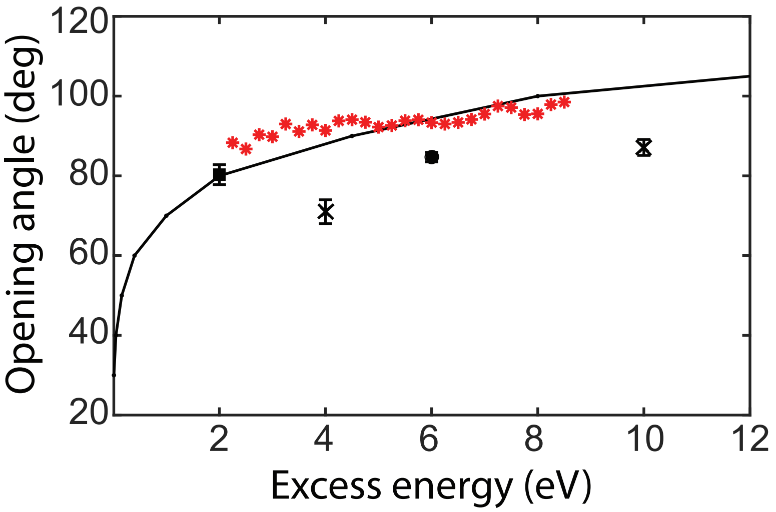

Figure 4.17: Variation of Opening Angle γ. Fitted values from measurement (red). Theoretical calculation from [129], solid black. Previously measured values: from [131] (black square), [128] (black circle), and [130] (crosses).

of the whole EWP can be shown, as in Figure 4.18, for the same emission angles of the first electron as in Figure 4.16.

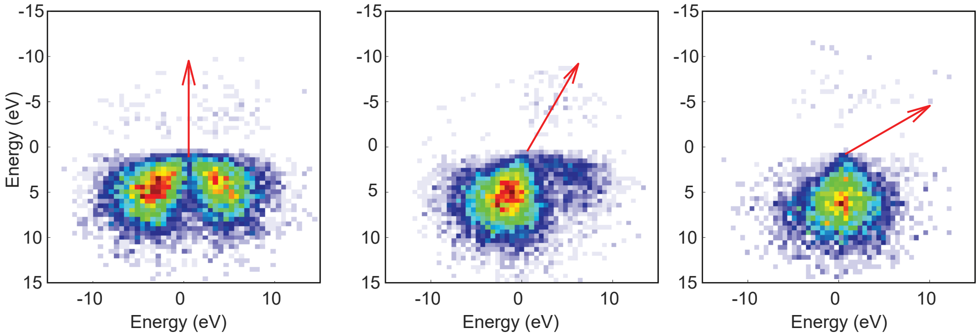

Figure 4.18: Distribution of Energies of Second Electron. Direction of first electron indicated by red arrows; 90° (left), 60° (middle), and 30° (right).

Chapter 5

Solid State Applications

The high repetition rate and short pulses makes the laser system used for this thesis attractive also for applications that do not necessarily involve the generation of XUV high-order harmonics. In this chapter, surface science applications performed directly with the near-IR laser output are presented. The first experiment from **Paper VII** concerns the control of electronic currents at high speeds, and the last two from **Paper VIII** and **IX** study the ultrafast dynamics of surface plasmons.

1 Light-Wave Currents

In modern electronics, transistors and similar components can switch electric currents at GHz rates, providing an upper limit to processing speeds. Optical light waves, however, oscillate at PHz rates—a million times faster—and if light fields could be used to control currents in semi-conductors, the possible computing speeds might increase dramatically. The PHz computer is far away, but the field of ultrafast optics has shown that light-wave driven currents are indeed possible to measure. The first observation of a macroscopic, measurable current driven by a laser impinging on a solid was reported in 2013 [132], and the phenomenon has since been observed in a variety of materials [133–135].

In **Paper VII**, the laser output after one NOPA stage was used to drive an electrical current in GaN between two contacts. Compared to previous studies, this work extends the scheme of light-wave driven currents to much higher repetition rates, i.e. 200 kHz instead of 1 kHz, and longer pulses. The increase in repetition rate is a small step closer towards the great computing speeds promised by light-wave electronics, and the longer pulse duration represents a relaxation of demands on the sophistication of the laser system.

In general, light-wave currents can be observed when a semiconductor or dielectric is exposed to a field strength close to the break-down threshold. There are a number of competing theories to explain the process [136–139]—in **Paper VII** the model presented by Khurgin in [138] was used to simulate currents observed with driving pulses carefully characterized by the d-scan technique.

The approach of Khurgin is based on the interference of different multi-photon transitions, which can be well described by the well-known nonlinear refractive index of a material. When the photon energy is not sufficient to cover the band gap, the laser field may still excite virtual electron-hole pairs below the band gap. The different multiphoton processes leading to the same energy will then interfere. The result of this interference between multiphoton processes that end up with different final parity states will differ for different directions of crystal momenta. The asymmetry leads to an observable current. This model of the physics behind the light-wave induced current is reminiscent of that behind the CEP dependent asymmetric photoelectron distributions, as described in Chapter 4.

The lowest order, where this multi-photon interference is possible, is with a one and two photon process, i.e. $\omega_1 = \omega_2 + \omega_3$, where ω_1 is the first photon process and $\omega_2 + \omega_3$ is the two photon process. The interference between the one- and two-photon absorption can be understood as a third-order nonlinear process and is thus connected to the third order susceptibility of the material, as shown in [138]. For very short pulses, this process will dominate, since there are plenty of different combinations of frequencies that fulfill the condition $\omega_1 = \omega_2 + \omega_3$ when the spectrum is octave-spanning. As the pulse duration increases, and the spectrum narrows, however, these combinations will decrease, while it is still possible to find many frequencies where the two-photon and three-photon transitions lead to the same energy. In general, higher-order processes decay slower when the pulse length increases. At the same time, optical breakdown becomes more likely.

The experiment was performed by focusing the laser onto devices with a geometry as shown in the upper left of Figure 5.1. Metal contacts of titanium and gold are deposited on top of epitaxially GaN on top of an Al_2O_3 wafer. A thin Al_2O_3 layer also protects the contacts. The laser is focused onto the gap and a current is driven through GaN, detected through the metal contacts. The GaN sample can easily be replaced with a BBO crystal for a d-scan measurement, to accurately measure the pulse duration at the experimental position. The same wedges used for the d-scan are then used to introduce dispersion to the pulse, and the current is measured as a function of glass insertion.

The two plots to the upper right of figure 5.1 show the calculated charge (blue) from a given waveform (red), for two different pulse durations. Both pulses result in a displacement of charge. However, the increase in pulse duration from 3.8 to 6.5 fs dramatically decreases its magnitude. For the shorter pulse it is readily observable, but for the 6.5 fs pulse a zoomed-in insert is required. At the bottom, measurement of resulting current as a function of pulse

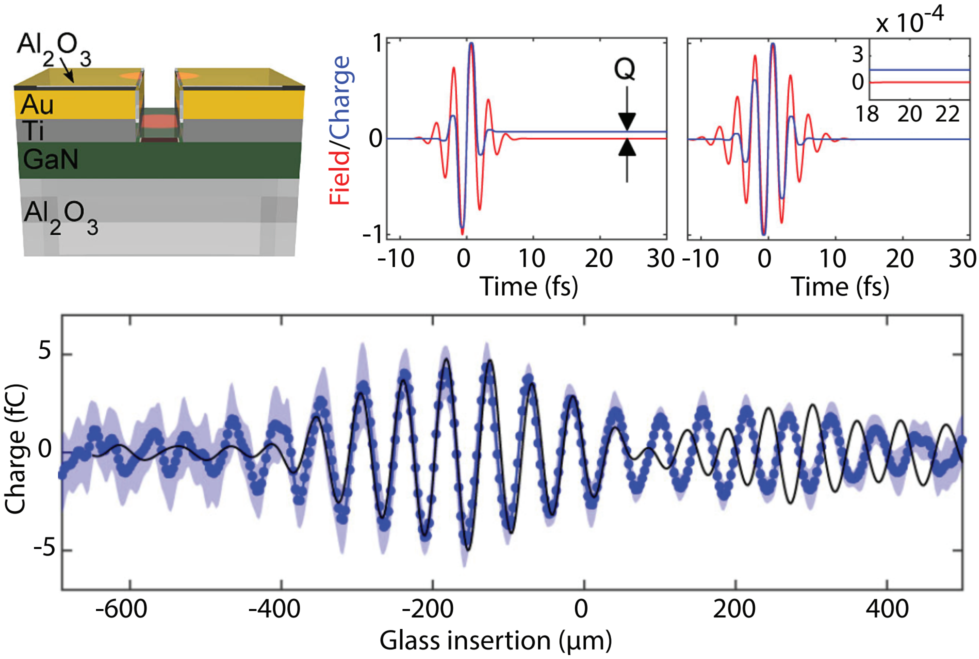

Figure 5.1: Ligh-Wave Currents Measurements. Top left: Schematic of devices. Middle and right: Simulations showing field (red) and generated charge (blue), for 3.8 fs (middle) and 6.5 fs (right). The residual charge is marked with arrows for the 3.8 fs pulse, and in an insert for the 6.5 fs pulse. Right: Measured residual charge as a function of glass wedge insertion (blue), and simulated charge from pulses measured by d-scan (black). Measurement uncertanity shown in light blue.

duration (i.e. glass wedge insertion) is shown in blue, compared to the model results in black. The model fits the results very well for the main part of the trace.

The resulting trace at the bottom could easily be mistaken for a representation of the waveform of the pulse, which is not the case. Instead the oscillations in the trace come from the fact that the nonlinear interference effects depend on the asymmetry of the waveform, i.e. the CEP. The oscillations follow the change of the CEP with dispersion, and the residual current is maximized when the vector potential of the field has a cosine-like waveform, and becomes zero for a sine-like waveform.

2 Photoelectron Spectroscopy from Surfaces

In this thesis work, a PhotoEmission Electron Microscope (PEEM) was used to image the photoemitted electrons from surfaces. A PEEM consists of a sequence of electron lenses which image the emitted electrons onto a detector. In such a lens system, there are a number of intermediate points where the photoelectrons will be focused, and if the density of electrons becomes too high, the electrons will repel each other, resulting in a distorted final image. In order to limit this space charge effect, which leads to a degraded spatial resolution, the number of electrons emitted at once must be kept low, ideally to just one per laser shot–i.e. the energy of the light pulse must be kept down. PEEM measurements therefore benefit greatly from higher repetition rates. During this thesis work, the 200 kHz laser was used in combination with a PEEM to investigate plasmon dynamics on the nanoscale.

2.1 Measuring Surface Plasmons

In solid state materials, the discrete energy levels of the constituent atoms broaden and form a complex band structure. In metals, the uppermost band is only partly filled. These electrons are shared between the atoms, and may move relatively easily, leading to the electrical conducting properties of metals—this top band is therefore called the conduction band. The relatively free behaviour of the electrons in the conduction bands means that they also share many properties with free electrons in a plasma, and interact with light in sometimes similar ways. When an electromagnetic field interacts with a free electron gas, it leads to a resonant oscillation within the plasma, called ”Langmuir waves”, or plasmons [140]. Such plasmons can also be observed in the conduction band of a metal.

At the interface between a dielectric and a metal, it is possible for electromagnetic fields to couple strongly to the electrons in the metal, leading to plasmons which propagate along the surface. If the size of the interface or object which leads to these surface plasmons is small enough, they will also be strongly localized. A strong localized electron distribution in turn leads to a high localized charge, which will couple back to the original field. This can induce very strong electromagnetic fields; a process which is called surface enhancement. Specially designed nanostructures may therefore be used to control and enhance light fields in novel ways, and this is today an active research area [141].

The surface plasmons that lead to these enhancement effects are not just localized in space, but also exhibit very short life times on the order of femtoseconds. To study their dynamics, ultrashort pulses are ideal. The understanding of the time evolution of these plasmons will be crucial for forming a complete picture of their origin and for achieving full coherent control. During this thesis work, the high repetition rate of the laser source has been used to investigate ultrafast dynamics of surface plasmons.

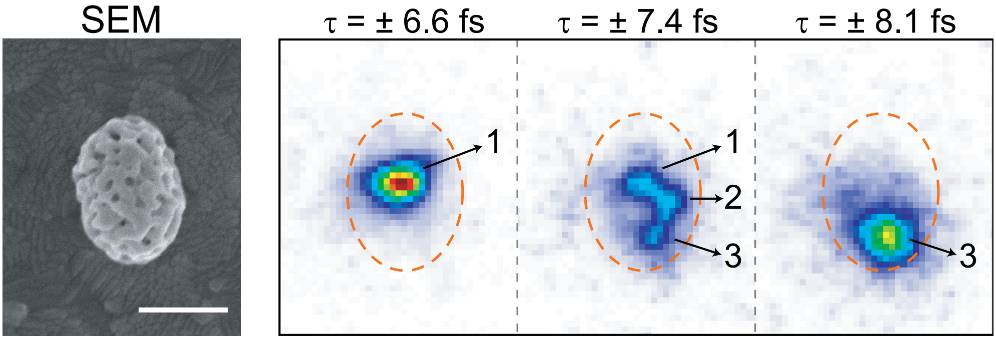

Figure 5.2: Nanosponge Hotspots. Left: SEM image of nanosponge, scale bar of 300 nm. Right: Hotspots measured by PEEM at different delays, marked above images. The different hotspots are numbered and indicated by arrows and numbers, showing activity at different times.

2.1.1 Gold Nanosponges

In **Paper VIII**, the non-linear emission from porous gold nanosponges was investigated. Plasmons from such metallic nanoantennas have been proposed as promising sources for e.g. subwavelength coherent light and ultrafast all optical control [142, 143]. The large flexibility in the design of such antennas provides the possibility of tuning them so that they are resonant with the frequency of the driving field, and many studies have been made to explore how these emissions may be enhanced by the use of different kinds of quantum emitters. Their ultrafast optical dynamics have not, however, been extensively studied, which is a necessity for achieving full coherent control.

In **Paper VIII**, it is found that the nonlinear emission from these sponges stems from a number of localized surface hot spots, and these were possible to image via time resolved PEEM measurements. Interferometric autocorrelation measurements were performed. In such a measurement, two replica IR pulses are created, and the signal is measured as a function of the delay between the two. It was shown that these hot spots act as independent long lived emitters with different resonance frequencies. Figure 5.2 shows, to the left, a scanning electron microscope (SEM) image of one nanosponge, and in the three images to the right, PEEM images at different delays between the optical pulses, indicated above the images, demonstrating three distinct hot spots.

2.1.2 TMD Interfaces

Paper IX explores spatio-temporal control of surface plasmons from 2D Transition Metal Dichalcogenides (TMDs)—a class of materials with many potential applications in optoelectronics due to their distinct layered structure which in many ways resembles graphene. Surface plasmons can be used to control the excitations of such materials, induced by introducing structures like borders or protrusions. **Paper IX** investigates the surface plasmon excitation at the edge between layers of the TMD WSe2 on a flat metal film, and demonstrates control over such plasmons on the attosecond timescale through the possibility of accurately depositing the 2D material with a lateral precision of a few tens of nanometers, and in singe atomic layers.

Chapter 6

Summary and Outlook

1 Summary

In this thesis, a 200 kHz attosecond light source was developed and used for applications in photoionization and surface science. Advanced techniques were employed for characterization of the OPA-based laser source, resulting in high-quality, 6 fs, few-cycle, near IR pulses with 15 μJ pulse energy and with good CEP stability.

Due to the low pulse energy compared to common, lower repetition rate, attosecond light sources, the efficient generation of high-order harmonics is challenging. Tight focusing is required to reach the intensities needed for HHG. In turn, phase matching necessitates a gas target with high gas density ($\sim$9 kg/m^3), corresponding to 5 bar pressure, and a short medium length ($\sim$40 μm). To achieve this, a nozzle-catcher configuration was implemented, and the performance of the gas target was found to match the required characteristics.

The generation of high-order harmonics with few-cycle pulses shows a strong dependence on the dispersion and CEP of the driving pulses. A multiple pulse interference model based on the three-step model of HHG was used to understand the effect of the CEP on the generated attosecond pulse train. The model suggests that in the present conditions, the number of attosecond pulses generated varies between two and three. This agrees with experimental results from HHG dispersion scans and photoionization. By varying the CEP, the structure of short attosecond pulse trains can be controlled.

The short attosecond pulse trains were used for XUV-IR pump-probe photoionization experiments. The use of a 3D momentum imaging spectrometer provided access to the full angular distribution of the photoelectrons. In the presence of an IR streaking field, a strong dependence on the number of pulses in the XUV attosecond train was observed, both concerning the angular symmetry and the number and position of the photoelectron peaks. In the case of ionization with two XUV pulses, the photoelectron peaks are shifted like in an attosecond streaking measurement. In the case of ionization with three attosecond pulses, new peaks are observed, similar to sidebands from a RABBIT measurement. This was explained with the help of a time-slit interference model.

The coincidence capabilities of the CIEL spectrometer were applied to study single-photon double-ionization of helium. In this process, a high-energy photon creates a strongly correlated photoelectron pair. By detecting the two photoelectrons in coincidence with the ion, the triple differential cross section was measured for the first time with an attosecond source, at a range of energies.

The laser source was also used for surface science applications that benefit from short pulse durations and high repetition rates. Light-wave driven currents were observed in GaN, for a higher repetition rate and longer pulses than previously reported. The current was measured as a function of dispersion, and the results were well replicated by a model based on multi-photon interference. Plasmon dynamics from nanostructures were investigated with a PEEM setup.

2 Outlook

The field of attosecond science moves forward in a number of different directions. One of those requires the development of high repetition rate attosecond light sources, which are needed for experiments that require spatial resolution, like in a PEEM, or coincidence information, such as with reaction microscopes. This thesis represents a step forward in that direction, and opens up for applying the techniques of attosecond science, with their extraordinary time-resolution, to new fields and phenomena.

2.1 Pulse-Pair Streaking

The traditional attosecond physics techniques for characterizing pulses from HHG rely on approximations that cannot be made when using trains generated by a few-cycle driver. In this thesis, the resulting photoelectron distributions created by different sequences of attosecond pulses together with the IR probe field were analyzed and explained by a time-slit interference model. While the SFA framework was used for this description, the approximations made and the understanding of the transition from streaking-like behavior to RABBIT-like behavior might be expanded to include a description of the influence of the atom.

While the three pulse case is interesting to analyze in order to understand the transition between the streaking and RABBIT regime, it is the two pulse case with its clear resemblance to the simple and intuitive streaking picture that may be more interesting to explore further. In order to accurately analyze an ordinary streaking trace, the modulations induced by the probe field must be significant compared to the bandwidth of the EWP spectrum. In the case where the spectrum is additionally modulated by the interference between two EWPs, the necessary strength of the probe field decreases significantly. The interference modulations, i.e. the harmonics, might in principle be analyzed as individual streaking traces, providing higher spectral resolution than in an ordinary streaking measurement. It would be interesting to investigate if the two-pulse streaking approach can give insight into new attosecond dynamics that conventional streaking and RABBIT cannot provide.

2.2 Highly-Correlated Electron Pairs

With the availability of a high repetition rate stable XUV source, a stable XUV-IR interferometer, and a powerful 3D momentum spectrometer, the work done during this thesis has set the stage for future investigation of the highly correlated electron pairs created by double ionization of atoms and molecules. In particular, the application of attosecond pump-probe techniques to follow the temporal evolution (and decoherence) of entangled electron pairs would be highly interesting.

After an upgrade to the pre-amplifier of the laser, the power stability of the HHG driver has been improved significantly, which also leads to better CEP stability. A better source stability means that experiments can be run for a longer time—and a long acquisition time is absolutely necessary for challenging experiments such as this. While pump-probe experiments were attempted on the single-photon double-ionization process, the temporal stability was not, at that time, sufficient for these experiments to yield any clear results. However, the upgrade and an improved active delay stabilization should make these experiments a reality in the near future.

2.3 ATTO-PEEM

While attosecond science has been successful in observing ultrafast phenomena and dynamics of atoms and molecules in gas phase, the study of more complex systems (e.g. on surfaces or in solids) requires the development of new approaches and tools. To observe plasmon dynamics, for example the properties of plasmonic nanostructures, high spatial and temporal resolution is simultaneously required. One proposed approach to achieve this is the ATTO-PEEM, which combines the spatial resolution of a PEEM setup with the temporal resolution of attosecond pump-probe techniques [20, 144]. The combination has shown immense potential [145, 146]. However, a crucial limiting factor in these experiments was space-charge related blurring.

The realization of the ATTO-PEEM has been a long standing goal of the attosecond research in Lund (in collaboration with the Division of Synchrotron Radiation Physics). First XUV imaging experiments were performed already in 2009 [147]. During this thesis work, pump-probe measurements on surfaces were realized with the high repetition rate attosecond light source. The beamline design, with the light being refocused after the CIEL and then sent to the spectrometer for surface measurements, even allows for calibrations using gas phase data. Both a hemispherical analyzer and a PEEM were used for measurements on a ZnO surface. Preliminary results are presently being analyzed. The realization of the ATTO-PEEM is finally within grasp.

Author Contributions

Paper I: Compact 200kHz HHG source driven by a few-cycle OPCPA

This paper presents the OPCPA laser and the HHG attosecond source at the time of publication. It includes a detailed description of the amplification process as well as characterization of the near-IR laser pulses with regards to CEP stability, spatio-temporal couplings, and spectrum and temporal structure. It also demonstrates efficient HHG in several different gas targets.

I participated in experiments characterizing the in and out-of-loop CEP. I was part of the discussions, and provided figures for the manuscript, along with comments and feedback.

Paper II: Characterizing ultrashort laser pulses with second harmonic dispersion scans

This paper presents a tutorial and overview of the dispersion scan characterization technique, as well as new developments in applying the technique to single-shot measurements and new spectral ranges.

I performed the measurements using the d-scan setup in the 1030 nm spectral range presented in the paper and participated in the measurements done on the few-cycle laser source. I provided comments and feedback for the manuscript.

Paper III: Phase control of attosecond pulses in a train

This paper presents measurements of the CEP and dispersion dependence of the HHG process for few-cycle pulses, as well as a model to reproduce and understand this behaviour based on a semi-classical approach.

I participated in the analysis and discussion of the results. For the manuscript I provided figures as well as comments and feedback.

Paper IV: A high-repetition rate attosecond light source for time-resolved coincidence spectroscopy

Compared to **Paper I**, this publication presents the upgraded 200 kHz pump-probe attosecond beamline at LLC. The XUV-IR pump-probe interferometer is presented in detail. It was used to perform proof-of-concept advanced 3D momentum spectroscopy measurements, demonstrating both capabilities for time resolved measurements and for demanding coincidence experiments.

I took a leading role in operating the light source for said experiments as well as participated in the installation and commissioning of the interferometer. I also took a leading role in performing the experiments using the 3D momentum spectrometer, and analysed the momentum results. I wrote the manuscript with help and feedback from the other authors.

Paper V: Accuracy and precision of the RABBIT technique

This paper investigates the performance of the RABBIT technique analytically and with simulations.

I performed simulations of RABBIT measurements based on the Strong Field Approximation and participated in the analysis of the results. I provided comments and feedback for the manuscript.

Paper VI: Controlling photoionization using attosecond time-slit interferences

This paper shows the results of two-color XUV-IR photoionization with few-cycle driving pulses, and shows the CEP dependence of the photoelectron distributions and explains how this can be understood with the help of electron wave-packet interference.

I took a leading role in performing the experiments. I did simulations of the photoionization process using the Strong Field Approximation and developed the model used to interpret the results. For the manuscript I provided figures, as well as participated in the discussion and writing process.

Paper VII: Few-cycle lightwave-driven currents in a semiconductor at high repetition rate

This paper presents results using the 200 kHz laser system to demonstrate light-wave driven currents in dielectrics with longer pulses at higher repetition rates than previously reported. A simple model based on interference of non-linear multi-photon processes was used to replicate the results.

I worked on operating and maintaining the light source and helped with optimizing it for the experiments. I provided comments and feedback for the manuscript.

Paper VIII: Nonlinear plasmon-exciton coupling enhances sum-frequency generation from a hybrid metal/semiconductor nanostructure

This paper presents measurements of the ultrafast dynamics of non-linear optical emission from plasmonic nanoantennas in the form of porous gold nanosponges infiltrated with zinc oxide emitters, using the 200 kHz laser system for time-resolved PEEM. The measurements were able to spatially and temporally resolve different plasmonic hotspots, and reveal how these couple to long-lived coherent exitonic emission.

I helped prepare the experimental setup. I worked on operating and maintaining the light source and helped with optimizing it for the experiments. I provided comments and feedback for the manuscript.

Paper IX: Coherent excitation and control of plasmons on gold using two-dimensional transition metal dichalcogenides

In this paper the 200 kHz laser system in combination with time-resolved PEEM was used to investigate surface plasmons excited by the interface between 2D TMDs and gold films, suggesting the possibility of controlling plasmon dynamics using such crystalline 2D materials.

I helped prepare the experimental setup. I worked on operating and maintaining the light source and helped with optimizing it for the experiments. I provided comments and feedback for the manuscript.

Acknowledgments

If you're reading this, that means I made it through this PhD in the end. I'm not entirely sure how that happened, but I do know for sure that I didn't do it alone. I don't know how I can adequately express how grateful I am to all the people I've been working with at the department of Atomic Physics—I could not have done a fraction of what I have managed in these years without you. Being a part of such a collaborative and supportive environment has meant the world to me.

Of course, there are many people at the department, and a few who have been more responsible for helping me finish this project than others. Let me start by thanking my supervisors. Cord—your support has been invaluable, especially through this last period of writing. Thank you for taking the time for me, always, and all your helpful advice. Anne—thank you for all the work you do in holding the attogroup together and for being an inspiration with your enthusiasm for physics. Miguel—thank you for showing me the ropes in the lab and teaching me the ins and outs of how to work with the laser. I also want to thank Mathieu, for all the discussions and your guidance with the challenging task of figuring out how to work with the spectrometer.

And then of course, my coworkers. Special thanks goes out to the (0.2)MHz group, whom I've worked closed with for the last four years. Anne Harth, for making me feel welcome and supported when I was just starting out. Chen, for all your help and for your endless competence. Yu-Chen, for your great work on the CIEL and company and conversation during the long measurements. Saikat, for showing me how to handle the vacuum. Ivan, for your great company and always checking in on me. Anne-Lise, for making sure I had a lovely time in Stockholm. Fabian, for your cheerful attitude and friendliness. Jan, for your constant positive outlook and helpfulness; I can't thank you enough. Dominik, for dealing with my confusion during my writing. And finally Anka, who arrived just in time to help me catch the last couple of typos!

To all the other lovely people who've been part of the attogroup during my time here, who are too many to list: Your presence and company in the hallways, coffee rooms, conferences and summer schools has been a huge part of making my time as a PhD a pleasure. Thank

you!

I also want to mention the people responsible for keeping the department afloat. Claes-Göran, your work as department head, together with the work work of Anne, Åke, Jakob, and Maria, is what makes it possible for the rest of us to do any research at all.

As nice as the department is, there are also people outside it who deserve to be mentioned. Valter and Gisela, thank you for your friendship and support. The last year of this thesis work, with the pandemic and all, would have been hell without you. My parents and my sister Elin, for asking me ”men förklara vad det är du gör nu igen” only a dozen times or so. You're the best: I love you. Willow—you know this would never have been possible without you. I can't tell you enough how grateful I am that you're in my life, and how much I love you.

And, finally, I would like to acknowledge Aiur the cat, who joined mine and Willow's little family during the last months of of my PhD. He's kept me company through more than one long evening of writing, and has never failed to make me smile or give me an encouraging headbutt when I needed it. We love him very much.

Figure 6.1: The Cutest Cat. Illustrated in a transient circular configuration.

References

[1] T. H. Maiman. Stimulated optical emission in Ruby. *J. Opt. Soc. Am.*, **50**:1134, 1960.

[2] P. A. Franken, A. E. Hill, C. W. Peters, and G. Weinreich. Generation of optical harmonics. *Phys. Rev. Lett.*, **7**:118, 1961.

[3] P. F. Moulton. Spectroscopic and laser characteristics of Ti:Al_2O_3. *J. Opt. Soc. Am. B*, 3(1):125–133, 1986.

[4] D. E. Spence, P. N. Kean, and W. Sibbett. 60-fsec pulse generation from a self-mode-locked Ti:sapphire laser. *Opt. Lett.*, **16**:42, 1991.

[5] D. S. G. Mourou. Compression of amplified chirped optical pulses. *Opt. Commun.*, **56**:219, 1985.

[6] A. Zewail. Femtochemistry: Atomic-Scale Dynamics of the Chemical Bond. *J. Phys. Chem. A*, 104:5660, 2000.

[7] A. McPherson, G. Gibson, H. Jara, U. Johann, T. S. Luk, I. A. McIntyre, K. Boyer, and C. K. Rhodes. Studies of multiphoton production of vacuum-ultraviolet radiation in the rare gases. *J. Opt. Soc. Am. B*, **4**:595, 1987.

[8] M. Ferray, A. L'Huillier, X. Li, L. Lompre, G. Mainfray, and C. Manus. Multiple-harmonic conversion of 1064 nm radiation in rare gases. *J. Phys. B*, **21**:L31, 1988.

[9] T. Popmintchev, M.-C. Chen, D. Popmintchev, P. Arpin, S. Brown, S. Alisauskas, G. Andriukaitis, T. Balciunas, O. Mücke, A. Pugzlys, A. Baltuska, B. Shim, S. Schrauth, A. Gaeta, C. Hernández-Garcia, L. Plaja, A. Becker, A. J.-B., M. Murnane, and H. Kapteyn. Bright coherent ultrahigh harmonics in the keV X-ray regime from mid-infrared femtosecond lasers. *Science*, 336(6086):1287–1291, 2012.

[10] P. Paul, E. Toma, P. Breger, G. Mullot, F. Augé, P. Balcou, H. Muller, and P. Agostini. Observation of a train of attosecond pulses from high harmonic generation. *Science*, 292(5522):1689–1692, 2001.

[11] M. Drescher, M. Hentschel, R. Kienberger, M. Uiberacker, V. Yakovlev, A. Scrinzi, T. Westerwalbesloh, U. Kleineberg, U. Heinzmann, and F. Krausz. Time-resolved atomic inner-shell spectroscopy. *Nature*, 419(6909):803–807, 2002.

[12] F. Calegari, D. Ayuso, A. Trabattoni, L. Belshaw, S. De Camillis, S. Anumula, F. Frassetto, L. Poletto, A. Palacios, P. Decleva, J. B. Greenwood, F. Martin, and M. Nisoli. Ultrafast electron dynamics in phenylalanine initiated by attosecond pulses. *Science*, 346(6207):336–339, 2014.

[13] P. M. Kraus, B. Mignolet, D. Baykusheva, A. Rupenyan, L. Horný, E. F. Penka, G. Grassi, O. I. Tolstikhin, J. Schneider, F. Jensen, L. B. Madsen, A. D. Bandrauk, F. Remacle, and H. J. Wörner. Measurement and laser control of attosecond charge migration in ionized iodoacetylene. *Science*, 350(6262):790–795, 2015.

[14] M. Schultze, M. Fieß, N. Karpowicz, J. Gagnon, M. Korbman, M. Hofstetter, S. Neppl, A. L. Cavalieri, Y. Komninos, T. Mercouris, C. A. Nicolaides, R. Pazourek, S. Nagele, J. Feist, J. Burgdörfer, A. M. Azzeer, R. Ernstorfer, R. Kienberger, U. Kleineberg, E. Goulielmakis, F. Krausz, and V. S. Yakovlev. Delay in photoemission. *Science*, 328:1658–1662, 2010.

[15] M. Isinger, R. J. Squibb, D. Busto, S. Zhong, A. Harth, D. Kroon, S. Nandi, C. L. Arnold, M. Miranda, J. M. Dahlström, E. Lindroth, R. Feifel, M. Gisselbrecht, and A. L'Huillier. Photoionization in the time and frequency domain. *Science*, 358(6365):893–896, 2017.

[16] A. L. Cavalieri, N. Müller, T. Uphues, V. S. Yakovlev, A. Baltuška, B. Horvath, B. Schmidt, L. Blümel, R. Holzwarth, S. Hendel, M. Drescher, U. Kleineberg, P. M. Echenique, R. Kienberger, F. Krausz, and U. Heinzmann. Attosecond spectroscopy in condensed matter. *Nature*, 449:1029, 2007.

[17] C. Heyl, H. Coudert-Alteirac, M. Miranda, M. Louisy, K. Kovacs, V. Tosa, E. Balogh, K. Varjú, A. L'Huillier, A. Couairon, et al. Scale-invariant nonlinear optics in gases. *Optica*, 3(1):75–81, 2016.

[18] A. Palacios, A. González-Castrillo, and F. Martín. Molecular interferometer to decode attosecond electron–nuclear dynamics. *Proc. Natl. Acad. Sci.*, 111(11):3973–3978, 2014.

[19] I. Makos, I. Orfanos, A. Nayak, J. Peschel, B. Major, I. Liontos, E. Skantzakis, N. Papadakis, C. Kalpouzos, M. Dumergue, S. Kühn, K. Varju, P. Johnsson, A. L'Huillier, P. Tzallas, and D. Charalambidis. ⊠ 10-gigawatt attosecond source for non-linear xuv optics and xuv-pump-xuv-probe studies. *Sci. Rep.*, 10(1), 2020.

[20] M. I. Stockman, M. F. Kling, U. Kleineberg, and F. Krausz. Attosecond nanoplasmonic-field microscope. *Nat. Photon.*, 1(9):539–544, 2007.

[21] J. Ullrich, R. Moshammer, A. Dorn, R. Dörner, L. P. H. Schmidt, and H. Schniidt-Böcking. Recoil-ion and electron momentum spectroscopy: reaction-microscopes. *Rep. Prog. Phys.*, 66(9):1463–1545, 2003.

[22] S. Hädrich, M. Krebs, J. Rothhardt, H. Carstens, S. Demmler, J. Limpert, and A. Tünnermann. Generation of μw level plateau harmonics at high repetition rate. *Opt. Express*, 19(20):19374–19383, 2011.

[23] M. Krebs, S. Hädrich, S. Demmler, J. Rothhardt, A. Zaïr, L. Chipperfield, J. Limpert, and A. Tünnermann. Towards isolated attosecond pulses at megahertz repetition rates. *Nat. Photon.*, 7(7):555–559, 2013.

[24] P. Rudawski, A. Harth, C. Guo, E. Lorek, M. Miranda, C. Heyl, E. Larsen, J. Ahrens, O. Prochnow, T. Binhammer, U. Morgner, J. Mauritsson, A. L'Huillier, and C. L. Arnold. Carrier-envelope phase dependent high-order harmonic generation with a high-repetition rate opcpa-system. *Eur. Phys. J. D*, 69(3):147–152, 2015.

[25] M. Osolodkov, F. J. Furch, F. Schell, P. Šušnjar, F. Cavalcante, C. S. Menoni, C. P. Schulz, T. Witting, and M. J. J. Vrakking. Generation and characterisation of few-pulse attosecond pulse trains at 100 kHz repetition rate. *J. Phys. B*, 53(19):194003, 2020.

[26] P. Ye, T. Csizmadia, L. G. Oldal, H. N. Gopalakrishna, M. Füle, Z. Filus, B. Nagyillés, Z. Divéki, T. Grósz, M. Dumergue, P. Jójárt, I. Seres, Z. Bengery, V. Zuba, Z. Várallyay, B. Major, F. Frassetto, M. Devetta, G. D. Lucarelli, M. Lucchini, B. Moio, S. Stagira, C. Vozzi, L. Poletto, M. Nisoli, D. Charalambidis, S. Kahaly, A. Zaïr, and K. Varjú. Attosecond pulse generation at ELI-ALPS 100 kHz repetition rate beamline. *J. Phys. B*, 53(15):154004, 2020.

[27] T. Young. I. the bakerian lecture. experiments and calculations relative to physical optics. *Philos. Trans. Royal Society*, 94:1–16, 1804.

[28] N. Picqué and T. W. Hänsch. Frequency comb spectroscopy. *Nat. Photon.*, 13(3):146–157, 2019.

[29] T. H. Maiman. Stimulated optical radiation in ruby. *Nature*, **187**:493, 1960.

[30] W. E. Lamb. Theory of an optical maser. *Phys. Rev.*, 134:A1429–A1450, 1964.

[31] L. E. Hargrove, R. L. Fork, and M. A. Pollack. Locking of HeNe laser modes induced by synchronous intracavity modulation. *Appl. Phys. Lett.*, 5(1):4–5, 1964.

[32] A. DeMaria, W. Glenn Jr., M. Brienza, and M. Mack. Picosecond laser pulses. *Proc. IEEE*, 57(1):2 – 25, 1969.

[33] A. D. E.P. Ippen, C.V. Shank. Passive mode locking of the cw dye laser. *Appl. Phys. Lett.*, 21(8):348–350, 1972.

[34] M. Nisoli, S. D. Silvestri, and O. Svelto. Generation of high energy 10 fs pulses by a new pulse compression technique. *Appl. Phys. Lett.*, 68:2793, 1996.

[35] M. Nisoli, S. D. Silvestri, O. Svelto, R. Szipöcs, K. Ferencz, C. Spielmann, S. Sartania, and F. Krausz. Compression of high-energy laser pulses below 5 fs. *Opt. Lett.*, 22:522, 1997.

[36] W. F. Krupke. Ytterbium solid-state lasers. the first decade. *IEEE J. Sel. Top. Quantum Electron.*, 6(6):1287–1296, 2000.

[37] S. A. Akhmanov, A. I. Kovrigin, A. S. Piskarskas, V. V. Fadeev, and R. V. Khokhlov. Observation of parametric amplification in the optical range. *JETP Letters*, 2:191, 1965.

[38] A. Dubietis, G. Jonusauskas, and A. Piskarskas. Powerful femtosecond pulse generation by chirped and stretched pulse parametric amplification in bbo crystal. *Opt. Commun.*, 88(4):437 – 440, 1992.

[39] L. J. Waxer, V. Bagnoud, I. A. Begishev, M. J. Guardalben, J. Puth, and J. D. Zuegel. High-conversion-efficiency optical parametric chirped-pulse amplification system using spatiotemporally shaped pump pulses. *Opt. Lett.*, 28(14):1245–1247, 2003.

[40] G. Cerullo and S. D. Silvestri. Ultrafast optical parametric amplifiers. *Rev. Sci. Instrum.*, 74(1):1–18, 2003.

[41] D. N. Schimpf, J. Rothhardt, J. Limpert, A. Tünnermann, and D. C. Hanna. Theoretical analysis of the gain bandwidth for noncollinear parametric amplification of ultrafast pulses. *J. Opt. Soc. Am. B*, 24(11):2837, 2007.

[42] T. Lang, A. Harth, J. Matyschok, T. Binhammer, M. Schultze, and U. Morgner. Impact of temporal, spatial and cascaded effects on the pulse formation in ultrabroadband parametric amplifiers. *Opt. Express*, 21(1):949–959, 2013.

[43] D. Eimerl, L. Davis, S. Velsko, E. K. Graham, and A. Zalkin. Optical, mechanical, and thermal properties of barium borate. *J. Appl. Phys.*, 62(5):1968–1983, 1987.

[44] I. Ross, P. Matousek, G. New, and K. Osvay. Analysis and optimization of optical parametric chirped pulse amplification. *J. Opt. Soc. Am. B*, 19(12):2945 – 2956, 2002.

[45] A. M. Weiner. Femtosecond pulse shaping using spatial light modulators. *Rev. Sci. Instrum.*, 71(5):1929–1960, 2000.

[46] I. A. Walmsley and C. Dorrer. Characterization of ultrashort electromagnetic pulses. *Adv. Opt. Photon.*, 1(2):308–437, 2009.

[47] C. Iaconis and I. A. Walmsley. Spectral phase interferometry for direct electric-field reconstruction of ultrashort optical pulses. *Opt. Lett.*, 23(10):792–794, 1998.

[48] S. Akturk, C. D'Amico, and A. Mysyrowicz. Measuring ultrashort pulses in the single-cycle regime using frequency-resolved optical gating. *J. Opt. Soc. Am. B*, 25(6):A63–A69, 2008.

[49] R. Trebino, K. W. DeLong, D. N. Fittinghoff, J. Sweetser, M. A. Krumbügel, and B. Richman. Measuring ultrashort laser pulses in the time-frequency domain using frequency-resolved optical gating. *Rev. Sci. Instrum.*, **68**:1, 1997.

[50] V. V. Lozovoy, I. Pastirk, and M. Dantus. Multiphoton intrapulse interference. IV. ultrashort laserpulse spectral phase characterization and compensation. *Opt. Lett.*, 29(7):775–777, 2004.

[51] M. Miranda, T. Fordell, C. Arnold, A. L'Huillier, and H. Crespo. Simultaneous compression and characterization of ultrashort laser pulses using chirped mirrors and glass wedges. *Opt. Express*, 20(1):688–697, 2012.

[52] M. Miranda, C. L. Arnold, T. Fordell, F. Silva, B. Alonso, R. Weigand, A. L'Huillier, and H. Crespo. Characterization of broadband few-cycle laser pulses with the d-scan technique. *Opt. Express*, 20(17):18732–18743, 2012.

[53] M. Miranda, J. Penedones, C. Guo, A. Harth, M. Louisy, L. Neoričić, A. L'Huillier, and C. L. Arnold. Fast iterative retrieval algorithm for ultrashort pulse characterization using dispersion scans. *J. Opt. Soc. Am. B*, 34(1):190–197, 2017.

[54] R. W. Gerchberg and W. O. Saxton. A practical algorithm for the determination of phase from image and diffraction plane pictures. *Optik*, 35(2):237–246, 1972.

[55] D. J. Kane. Real-Time Measurement of Ultrashort Laser Pulses Using Principal Component Generalized Projections. *IEEE J. Sel. Top. Quantum Electron.*, 4:278–284, 1998.

[56] D. J. Kane. Principal components generalized projections: a review [invited]. *J. Opt. Soc. Am. B*, 25(6):A120, 2008.

[57] H. R. Telle, G. Steinmeyer, A. E. Dunlop, J. Stenger, D. H. Sutter, and U. Keller. Carrier-envelope offset phase control: A novel concept for absolute optical frequency measurement and ultrashort pulse generation. *Appl. Phys. B*, 69:327, 1999.

[58] M. Kakehata, H. Takada, Y. Kobayash, K. Torizuka, Y. Fujihira, T. Homma, and H. Takahashi. Single-shot measurement of carrier-envelope phase changes by spectral interferometry. *Opt. Lett.*, 26(18):1436, 2001.

[59] S. Akturk, X. Gu, P. Bowlan, and R. Trebino. Spatio-temporal couplings in ultrashort laser pulses. *J. Opt.*, 12(9):093001, 2010.

[60] M. Miranda, M. Kotur, P. Rudawski, C. Guo, A. Harth, A. L'Huillier, and C. L. Arnold. Spatiotemporal characterization of ultrashort laser pulses using spatially resolved Fourier transform spectrometry. *Opt. Lett.*, 39(17):5142–5145, 2014.

[61] G. Pariente, V. Gallet, A. Borot, O. Gobert, and F. Quéré. Space–time characterization of ultra-intense femtosecond laser beams. *Nat. Photon.*, 10(8):547–553, 2016.

[62] G. Farkas and C. Tóth. Proposal for attosecond light pulse generation using laser induced multiple-harmonic conversion processes in rare gases. *Phys. Lett. A*, **168**:447, 1992.

[63] P. Antoine, A. L'Huillier, and M. Lewenstein. Attosecond Pulse Trains Using High-Order Harmonics. *Phys. Rev. Lett.*, **77**:1234, 1996.

[64] P. B. Corkum, N. H. Burnett, and M. Y. Ivanov. Subfemtosecond pulses. *Opt. Lett.*, 19:1870, 1994.

[65] M. Hentschel, R. Kienberger, C. Spielmann, G. A. Reider, N. Milosevic, T. Brabec, P. Corkum, U. Heinzmann, M. Drescher, and F. Krausz. Attosecond metrology. *Nature*, 414(6863):509–513, 2001.

[66] T. Gaumnitz, A. Jain, Y. Pertot, M. Huppert, I. Jordan, F. Ardana-Lamas, and H. J. Wörner. Streaking of 43-attosecond soft-X-ray pulses generated by a passively CEP-stable mid-infrared driver. *Opt. Express*, 25(22):27506, 2017.

[67] E. Goulielmakis, M. Schultze, M. Hofstetter, V. S. Yakovlev, J. Gagnon, M. Uiberacker, A. L. Aquila, E. Gullikson, D. T. Attwood, R. Kienberger, et al. Single-cycle nonlinear optics. *Science*, 320(5883):1614–1617, 2008.

[68] R. Kienberger, M. Hentschel, M. Uiberacker, C. Spielmann, M. Kitzler, A. Scrinzi, M. Wieland, T. Westerwalbesloh, U. Kleineberg, U. Heinzmann, M. Drescher, and F. Krausz. Steering Attosecond Electron Wave Packets with Light. *Science*, **297**:1144, 2002.

[69] F. Quéré, J. Itatani, G. L. Yudin, and P. B. Corkum. Attosecond Spectral Shearing Interferometry. *Phys. Rev. Lett.*, **90**:073902, 2003.

[70] Y. Mairesse, A. de Bohan, L. J. Frasinski, H. Merdji, L. C. Dinu, P. Monchicourt, P. Breger, M. Kovačev, R. Taïeb, B. Carré, H. G. Muller, P. Agostini, and P. Salières. Attosecond synchronization of high-harmonic soft X-rays. *Science*, 302:1540, 2003.

[71] M. Nisoli, G. Sansone, S. Stagira, S. De Silvestri, C. Vozzi, M. Pascolini, L. Poletto, P. Villoresi, and G. Tondello. Effects of carrier-envelope phase differences of few-optical-cycle light pulses in single-shot high-order-harmonic spectra. *Phys. Rev. Lett.*, 91(21):213905, 2003.

[72] I. Sola, E. Mével, L. Elouga, E. Constant, V. Strelkov, L. Poletto, P. Villoresi, E. Benedetti, J.-P. Caumes, S. Stagira, C. Vozzi, G. Sansone, and M. Nisoli. Controlling attosecond electron dynamics by phase-stabilized polarization gating. *Nat. Phys.*, 2:319, 2006.

[73] C. A. Haworth, L. E. Chipperfield, J. S. Robinson, P. L. Knight, J. P. Marangos, and J. W. Tisch. Half-cycle cutoffs in harmonic spectra and robust carrier-envelope phase retrieval. *Nat. Phys.*, 3(1):52–57, 2007.

[74] K. C. Kulander, K. J. Schafer, and J. L. Krause. Dynamics of short-pulse excitation, ionization and harmonic conversion. In *Super-Intense Laser-Atom Physics*. Plenum Press, New York, 1993.

[75] P. Corkum. Plasma perspective on strong-field multiphoton ionization. *Phys. Rev. Lett.*, **71**:1994, 1993.

[76] M. Lewenstein, P. Balcou, M. Ivanov, A. L'Huillier, and P. Corkum. Theory of high-order harmonic generation by low-frequency laser fields. *Phys. Rev. A*, 49:2117, 1994.

[77] K. Varjú, Y. Mairesse, B. Carré, M. Gaarde, P. Johnsson, S. Kazamias, R. López-Martens, J. Mauritsson, K. Schafer, P. Balcou, et al. Frequency chirp of harmonic and attosecond pulses. *J. Mod. Opt.*, 52(2-3):379–394, 2005.

[78] N. Dudovich, O. Smirnova, J. Levesque, Y. Mairesse, M. Y. Ivanov, D. Villeneuve, and P. B. Corkum. Measuring and controlling the birth of attosecond xuv pulses. *Nat. Phys.*, 2(11):781–786, 2006.

[79] J. Samson and W. Stolte. Precision measurements of the total photoionization cross sections of he, ne, ar, kr, and xe. *J. Electron Spectros. Relat. Phenomena*, pages 265–276, 2002.

[80] M. Ammosov, N. Delone, and V. Krainov. Tunnelling ionization of complex atoms and of atomic ions in an alternating electromagnetic field. *Sov. Phys. JETP*, 64(6):1191–1194, 1986.

[81] H. Wikmark, C. Guo, J. Vogelsang, P. W. Smorenburg, H. Coudert-Alteirac, J. Lahl, J. Peschel, P. Rudawski, H. Dacasa, S. Carlström, S. Maclot, M. B. Gaarde, P. Johnsson, C. L. Arnold, and A. L'Huillier. Spatiotemporal coupling of attosecond pulses. *Proc. Natl. Acad. Sci.*, 116(11):4779–4787, 2019.

[82] R. Kienberger, E. Goulielmakis, M. Uiberacker, A. Baltuška, V. Yakovlev, F. Bammer, A. Scrinzi, T. Westerwalbesloh, U. Kleineberg, U. Heinzmann, M. Drescher, and F. Krausz. Atomic transient recorder. *Nature*, 427:817, 2004.

[83] G. Sansone, E. Benedetti, F. Calegari, C. Vozzi, L. Avaldi, R. Flammini, L. Poletto, P. Villoresi, C. Altucci, R. Velotta, et al. Isolated single-cycle attosecond pulses. *Science*, 314(5798):443–446, 2006.

[84] S. Kazamias, D. Douillet, F.Weihe, C. Valentin, A. Rousse, S. Sebban, G. Grillon, F. Augé, D. Hulin, and P. Balcou. Global Optimization of High Harmonic Generation. *Phys. Rev. Lett.*, 90:193901, 2003.

[85] M. B. Gaarde, J. L. Tate, and K. J. Schafer. Macroscopic aspects of attosecond pulse generation. *J. Phys. B*, 41:132001, 2008.

[86] C. M. Heyl, C. L. Arnold, A. Couairon, and A. L'Huillier. Introduction to macroscopic power scaling principles for high-order harmonic generation. *J. Phys. B*, 50(1):013001, 2017.

[87] R. Weissenbilder. Private communication. 2020.

[88] A. Börzsönyi, Z. Heiner, M. P. Kalashnikov, A. P. Kovács, and K. Osvay. Dispersion measurement of inert gases and gas mixtures at 800 nm. *Appl. Opt.*, 47(27):4856–4863, 2008.

[89] H. Hertz. Ueber einen Einfluss des ultravioletten Lichtes auf die electrische Entladung. *Ann. Physik*, 267:983, 1887.

[90] A. Einstein. Über einen die erzeugung und verwandlung des lichtes betreffenden heuristischen gesichtspunkt. *Ann. Phys.*, 322(6):132–148, 1905.

[91] C. J. Davisson. The diffraction of electrons by a crystal of nickel. *Bell System Technical Journal*, 7(1):90–105, 1928.

[92] P. Kruit and F. H. Read. Magnetic field paralleliser for 2π electron-spectrometer and electron-image magnifier. *J. Phys. E*, 16:313, 1983.

[93] C. Cha, G. Ganteför, and W. Eberhardt. New experimental setup for photoelectron spectroscopy on cluster anions. *Rev. Sci. Instrum.*, 63(12):5661–5666, 1992.

[94] A. T. J. B. Eppink and D. H. Parker. Velocity map imaging of ions and electrons using electrostatic lenses: Application in photoelectron and photofragment ion imaging of molecular oxygen. *Rev. Sci. Instr.*, 68:3477, 1997.

[95] L. Rading, J. Lahl, S. Maclot, F. Campi, H. Coudert-Alteirac, B. Oostenrijk, J. Peschel, H. Wikmark, P. Rudawski, M. Gisselbrecht, and P. Johnsson. A versatile velocity map ion-electron covariance imaging spectrometer for high-intensity XUV experiments. *Appl. Sci.*, 8(6):998, 2018.

[96] J. Ullrich, R. Moshammer, R. Dörner, O. Jagutzki, V. Mergel, H. Schmidt-Böcking, and L. Spielberger. Recoil-ion momentum spectroscopy. *J. Phys. B*, 30(13):2917–2974, 1997.

[97] R. Dörner, J. Ullrich, H. Schmidt-Böcking, and R. E. Olson. Three-body interactions in proton-helium angular scattering. *Phys. Rev. Lett.*, 63:147–150, 1989.

[98] M. Lavollée. A new detector for measuring three-dimensional momenta of charged particles in coincidence. *Rev. Sci. Instrum.*, 70(7):2968–2974, 1999.

[99] A. Huetz and J. Mazeau. Double photoionization of helium down to 100 mev above threshold. *Phys. Rev. Lett.*, 85:530–533, 2000.

[100] M. Gisselbrecht, A. Huetz, M. LavollÃ©e, T. J. Reddish, and D. P. Seccombe. Optimization of momentum imaging systems using electric and magnetic fields. *Rev. Sci. Instrum.*, 76(1):013105, 2005.

[101] Y.-C. Cheng. *Ultrafast Photoionization Dynamics Studied with Coincidence Momentum Imaging Spectrometers. [Elektronisk resurs].* Department of Physics, Lund University, 2019.

[102] I. H. M. W. C. Wiley. Time-of-flight mass spectrometer with improved resolution. *Rev. Sci. Instrum*, 1955.

[103] W. Steckelmacher, R. Strong, and M. W. Lucas. A simple atomic or molecular beam as target for ion-atom collision studies. *J. Phys. D*, 11(11):1553–1566, 1978.

[104] O. Jagutzki, V. Mergel, K. Ullmann-Pfleger, L. Spielberger, U. Spillmann, R. Dörner, and H. Schmidt-Böcking. A broad-application microchannel-plate detector system for advanced particle or photon detection tasks: large area imaging, precise multi-hit timing information and high detection rate. *Nucl. Instrum. Methods Phys. Res. A*, 477(1):244 – 249, 2002. 5th Int. Conf. on Position-Sensitive Detectors.

[105] O. Jagutzki, A. Cerezo, A. Czasch, R. Dorner, M. Hattas, Min Huang, V. Mergel, U. Spillmann, K. Ullmann-Pfleger, T. Weber, H. Schmidt-Bocking, and G. D. W. Smith. Multiple hit readout of a microchannel plate detector with a three-layer delay-line anode. *IEEE Trans. Nucl. Sci.*, 49(5):2477–2483, 2002.

[106] V. Véniard, R. Taïeb, and A. Maquet. Phase dependence of (N+1) - color (N>1) ir-uv photoionization of atoms with higher harmonics. *Phys. Rev. A*, **54**:721, 1996.

[107] E. Constant, V. D. Taranukhin, A. Stolow, and P. B. Corkum. Methods for the measurement of the duration of high-harmonic pulses. *Phys. Rev. A*, 56:3870, 1997.

[108] K. Klünder, J. M. Dahlström, M. Gisselbrecht, T. Fordell, M. Swoboda, D. Guénot, P. Johnsson, J. Caillat, J. Mauritsson, A. Maquet, R. Taïeb, and A. L'Huillier. Probing single-photon ionization on the attosecond time scale. *Phys. Rev. Lett.*, 106:143002, 2011.

[109] F. Quéré, Y. Mairesse, and J. Itatani. Temporal characterization of attosecond XUV fields. *J. Mod. Opt.*, 52:339, 2005.

[110] Y. Mairesse and F. Quéré. Frequency-resolved optical gating for complete reconstruction of attosecond bursts. *Phys. Rev. A*, 71:011401(R), 2005.

[111] K. C. Kulander. Time-dependent Hartree-Fock theory of multiphoton ionization: Helium. *Phys. Rev A*, 36:2726, 1987.

[112] H. A. Bethe and E. E. Salpeter. *Quantum mechanics of one- and two-electron atoms*. Plenum Publishing Corp, United States, 1977.

[113] A. L'Huillier, M. Lewenstein, P. Salières, P. Balcou, M. Y. Ivanov, J. Larsson, and C. G. Wahlström. High-order harmonic generation cutoff. *Phys. Rev. A*, 48:R3433, 1993.

[114] R. Pazourek, S. Nagele, and J. Burgdörfer. Attosecond chronoscopy of photoemission. *Rev. Mod. Phys.*, 87:765–802, 2015.

[115] N. Chandra and M. Chakraborty. Entanglement in double photoionization of atoms. *J. Phys. B*, 35(10):2219–2238, 2002.

[116] N. Chandra and R. Ghosh. Generation of tunable entangled states of two electrons and their characterization without entanglement witness. *Phys. Rev. A*, 70:060306, 2004.

[117] D. Akoury, K. Kreidi, T. Jahnke, T. Weber, A. Staudte, M. Schoffler, N. Neumann, J. Titze, L. P. H. Schmidt, A. Czasch, O. Jagutzki, R. A. C. Fraga, R. E. Grisenti, R. D. Muino, N. A. Cherepkov, S. K. Semenov, P. Ranitovic, C. L. Cocke, T. Osipov, H. Adaniya, J. C. Thompson, M. H. Prior, A. Belkacem, A. L. Landers, H. Schmidt-Bocking, and R. Dorner. The simplest double slit: Interference and entanglement in double photoionization of h2. *Science*, 318(5852):949–952, 2007.

[118] R. Peterkop. WKB approximation and threshold law for electron-atom ionization. *J. Phys. B*, 4(4):513–521, 1971.

[119] A. R. P. Rau. Two electrons in a coulomb potential. double-continuum wave functions and threshold law for electron-atom ionization. *Phys. Rev. A*, 4(1):207–220, 1971.

[120] A. Huetz, P. Selles, D. Waymel, and J. Mazeau. Wannier theory for double photoionization of noble gases. *J. Phys. B*, 24(8):1917–1933, 1991.

[121] F. Maulbetsch and J. S. Briggs. Selection rules for transitions to two-electron continuum states. *J. Phys. B*, 28(4):551–564, 1995.

[122] L. Avaldi and A. Huetz. Photodouble ionization and the dynamics of electron pairs in the continuum. *J. Phys. B*, 38(9):S861–S891, 2005.

[123] J. S. Briggs and V. Schmidt. Differential cross sections for photo-double-ionization of the helium atom. *J. Phys. B*, 33(1):R1–R48, 1999.

[124] E. P. Månsson, D. Guénot, C. L. Arnold, D. Kroon, S. Kasper, J. M. Dahlström, E. Lindroth, A. S. Kheifets, A. L'Huillier, S. L. Sorensen, et al. Double ionization probed on the attosecond timescale. *Nat. Phys.*, 10:207–211, 2014.

[125] G. H. Wannier. The threshold law for single ionization of atoms or ions by electrons. *Phys. Rev.*, 90:817–825, 1953.

[126] J. A. R. Samson, W. C. Stolte, Z.-X. He, J. N. Cutler, Y. Lu, and R. J. Bartlett. Double photoionization of helium. *Phys. Rev. A*, 57:1906–1911, 1998.

[127] H. Bräuning, R. Dörner, C. L. Cocke, M. H. Prior, B. Krässig, A. S. Kheifets, I. Bray, A. Bräuning-Demian, K. Carnes, S. Dreuil, V. Mergel, P. Richard, J. Ullrich, and H. Schmidt-Böcking. Absolute triple differential cross sections for photo-double ionization of helium - experiment and theory. *J. Phys. B*, 31(23):5149–5160, 1998.

[128] R. Dörner, H. Bräuning, J. M. Feagin, V. Mergel, O. Jagutzki, L. Spielberger, T. Vogt, H. Khemliche, M. H. Prior, J. Ullrich, C. L. Cocke, and H. Schmidt-Böcking. Photo-double-ionization of he: Fully differential and absolute electronic and ionic momentum distributions. *Phys. Rev. A*, 57:1074–1090, 1998.

[129] L. Malegat, P. Selles, and A. Kazansky. Double photoionization of helium: The hyperspherical $\mathcal{R}$-matrix method with semiclassical outgoing waves. *Phys. Rev. A*, 60:3667–3676, 1999.

[130] L. Malegat, P. Selles, P. Lablanquie, J. Mazeau, and A. Huetz. Double photoionization: II. analysis of experimental triple differential cross sections in helium and neon. *J. Phys. B*, 30(2):263–276, 1997.

[131] G. Dawber, L. Avaldi, A. G. McConkey, H. Rojas, M. A. MacDonald, and G. C. King. Near threshold TDCS for photo-double ionization of helium. *J. Phys. B*, 28(8):L271–L277, 1995.

[132] A. Schiffrin, T. Paasch-Colberg, N. Karpowicz, V. Apalkov, D. Gerster, S. Mühlbrandt, M. Korbman, J. Reichert, M. Schultze, S. Holzner, J. V. Barth, R. Kienberger, R. Ernstorfer, V. S. Yakovlev, M. I. Stockman, and F. Krausz. Optical-field-induced current in dielectrics. *Nature*, 493(7430):70–74, 2013.

[133] O. Kwon and D. Kim. Phz current switching in calcium fluoride single crystal. *Appl. Phys. Lett.*, 108(19):191112, 2020.

[134] O. Kwon, T. Paasch-Colberg, V. Apalkov, B.-K. Kim, J.-J. Kim, M. I. Stockman, and D. Kim. Semimetallization of dielectrics in strong optical fields. *Sci. Rep.*, 6(1):21272, 2016.

[135] T. Paasch-Colberg, S. Y. Kruchinin, Özge Sağlam, S. Kapser, S. Cabrini, S. Muehlbrandt, J. Reichert, J. V. Barth, R. Ernstorfer, R. Kienberger, V. S. Yakovlev, N. Karpowicz, and A. Schiffrin. Sub-cycle optical control of current in a semiconductor: from the multiphoton to the tunneling regime. *Optica*, 3(12):1358–1361, 2016.

[136] V. Apalkov and M. I. Stockman. Theory of dielectric nanofilms in strong ultrafast optical fields. *Phys. Rev. B*, 86:165118, 2012.

[137] S. Y. Kruchinin, M. Korbman, and V. S. Yakovlev. Theory of strong-field injection and control of photocurrent in dielectrics and wide band gap semiconductors. *Phys. Rev. B*, 87:115201, 2013.

[138] J. B. Khurgin. Optically induced currents in dielectrics and semiconductors as a nonlinear optical effect. *J. Opt. Soc. Am. B*, 33(7):C1–C9, 2016.

[139] L. Chen, Y. Zhang, G. Chen, and I. Franco. Stark control of electrons along nanojunctions. *Nat. Commun.*, 9(1):2070, 2018.

[140] L. Tonks and I. Langmuir. Oscillations in ionized gases. *Phys. Rev.*, 33:195–210, 1929.

[141] L. Novotny and N. van Hulst. Antennas for light. *Nat. Photon.*, 5(2):83–90, 2011.

[142] M. Kauranen and A. Zayats. Nonlinear plasmonics. *Nat. Photon.*, 6(11):737–748, 2012.

[143] P. Vasa, W. Wang, R. Pomraenke, M. Lammers, M. Maiuri, C. Manzoni, G. Cerullo, and C. Lienau. Real-time observation of ultrafast rabi oscillations between excitons and plasmons in metal nanostructures with j-aggregates. *Nat. Photon.*, 7(2):128–132, 2013.

[144] S. H. Chew, K. Pearce, C. Späth, A. Guggenmos, J. Schmidt, F. Süßmann, M. F. Kling, U. Kleineberg, E. Mårsell, C. L. Arnold, E. Lorek, P. Rudawski, C. Guo, M. Miranda, F. Ardana, J. Mauritsson, A. L'Huillier, and A. Mikkelsen. Imaging Localized Surface Plasmons by Femtosecond to Attosecond Time-Resolved Photoelectron Emission Microscopy- "ATTO-PEEM". In P. Hommelhoff and M. F. Kling, editors, *Attosecond Nanophysics*, pages 325–364. Wiley-VCH Verlag GmbH and Co. KGaA, 2014.

[145] S. H. Chew, F. Süssmann, C. Späth, A. Wirth, J. Schmidt, S. Zherebtsov, A. Guggenmos, A. Oelsner, N. Weber, J. Kapaldo, A. Gliserin, M. I. Stockman, M. F. Kling, and U. Kleineberg. Time-of-flight-photoelectron emission microscopy on plasmonic structures using attosecond extreme ultraviolet pulses. *Appl. Phys. Lett.*, 100(5):–, 2012.

[146] E. Mårsell, C. L. Arnold, E. Lorek, D. Guenot, T. Fordell, M. Miranda, J. Mauritsson, H. Xu, A. L'Huillier, and A. Mikkelsen. Secondary electron imaging of nanostructures using extreme ultra-violet attosecond pulse trains and infra-red femtosecond pulses. *Ann. Phys.*, 525(1-2):162–170, 2013.

[147] A. Mikkelsen, J. Schwenke, T. Fordell, G. Luo, K. Klünder, E. Hilner, N. Anttu, A. Zakharov, E. Lundgren, J. Mauritsson, J. Andersen, H. Xu, and A. L'Huillier. Photoemission electron microscopy using extreme ultraviolet attosecond pulse trains. *Rev. Sci. Instrum.*, 80:123703, 2009.

Paper I

Paper II

Paper III

Paper IV

Paper V

Paper VI

Paper VII

Paper VIII

Paper IX

Printed by Media-Tryck, Lund 2021 NORDIC SWAN ECOLABEL 3041 0903

LUND UNIVERSITY
Faculty of Engineering, LTH
Department of Physics
Division of Atomic Physics

ISBN: 978-91-7895-713-2 (print)
ISBN: 978-91-7895-714-9 (pdf)
ISSN: 0281-2762
Lund Reports on Atomic Physics, LRAP 570 (2020)